High-Performance RF-MEMS Tunable Filters

by

Sang-June Park

A dissertation submitted in partial fulfillment
of the requirements for the degree of
Doctor of Philosophy
(Electrical Engineering)
in The University of Michigan
2008

Doctoral Committee:

Professor Amir Mortazawi, Co-Chair
Professor Gabriel M. Rebeiz, Co-Chair, University of California, San Diego
Professor Mahta Moghaddam
Professor Kim A. Winick

To my family

Acknowledgements

Among all who have contributed to my education at the University of Michigan, my greatest appreciation surely belongs to my advisor, Professor Gabriel M. Rebeiz who guided me through the Ph.D. program. Without his help and support I could not have this great opportunity. During the years of working with him, I learned a great deal both about technical issues and how to analyze and solve the problem. His devotion to how-to-think is a precious lesson that I would never forget. I also would like to thank my dissertation committee members, Prof. Amir Mortazawi, Prof. Mahta Moghaddam and Prof. Kim A. Winick for their participation, support and feedback.

I have also enjoyed the friendship, advice and help from many people in the TICS group including Carson, who discussed many interesting issues with me, Prof. Abbas A.Tamijani, Prof. Kamran Entesari, Chris Galbraith, Byung Wook Min, Michael Chang, Alex Girchner, Mohammed El-Tanani, Isak Reines, Tiku Yu, Jason May and also many other friends from Radiation Laboratory. I also have good memories with my Korean friends. Especially, I would like to thank to Dong-Joon, who shared many things with me in Ann Arbor, and Kwang-Jin, Jung-Guen, and Sang-Young for their good friendship in San Diego.

My acknowledgement will not be complete without mentioning the staff members of the Radiation Lab and EECS department for their dedication and for their assistance through the past years.

Finally, I would like to thank my family. Their unconditional love and emotional support has been the greatest motivation for me to keep progressing during these years. Specially, I thank my wife, Kang-Yoon, my parents, my sister, and my lovely daughter, Su-Young. It is to commemorate their love that I dedicate this thesis to them.

Table of Contents

List of Tables

List of Figures

Chapter 1

Introduction

1.1 Tunable filter technology overview

In modern wireless communication systems, multi-band and multi-mode devices are taking more and more of the spotlight, becoming a major trend due to their ability to cover different communication standards with a single device. A new wireless paradigm called "cognitive radio" recently emerged as a hot research topic. This radio scans the available spectrum and change its network parameters (frequency, bandwidth, modulation) for maximum data transfer. Some essential components for the cognitive radio are tunable filters, tunable antennas, and tunable high-efficiency power amplifiers. The importance of tunable filters in such devices is substantial since they could replace the use of a switched-filter bank with a single component (Fig. 1.1).

Tunable filters have been reported since the development of radar systems and are a very active research area now. The mechanical tunable filters are the oldest of their kind and their design principles are well explained in the literature [7]. Even though they have excellent insertion loss and power handling capabilities, their large size and very slow tuning speed limit their use in wireless communication systems. Thus, the tunable filter technology which is feasible to wireless systems can be categorized in four different ones; YIG (Yttrium-Iron-Garnet) filters [7–10], BST (Barium Strontium Titanate) filters [11], varactor filters [12], and RF-MEMS (Micro-Electro-Mechanical-Systems) filters.

The YIG filters contain single-crystal Yttrium-Iron-Garnet spheres in their resonator and are controlled by the ferromagnetic resonance frequency change with an externally applied DC magnetic field. These filters have multi-octave tuning ranges and a Q up to 10,000 at 0.1-6 GHz. However, their power consumption, tuning speed, size, and weight are

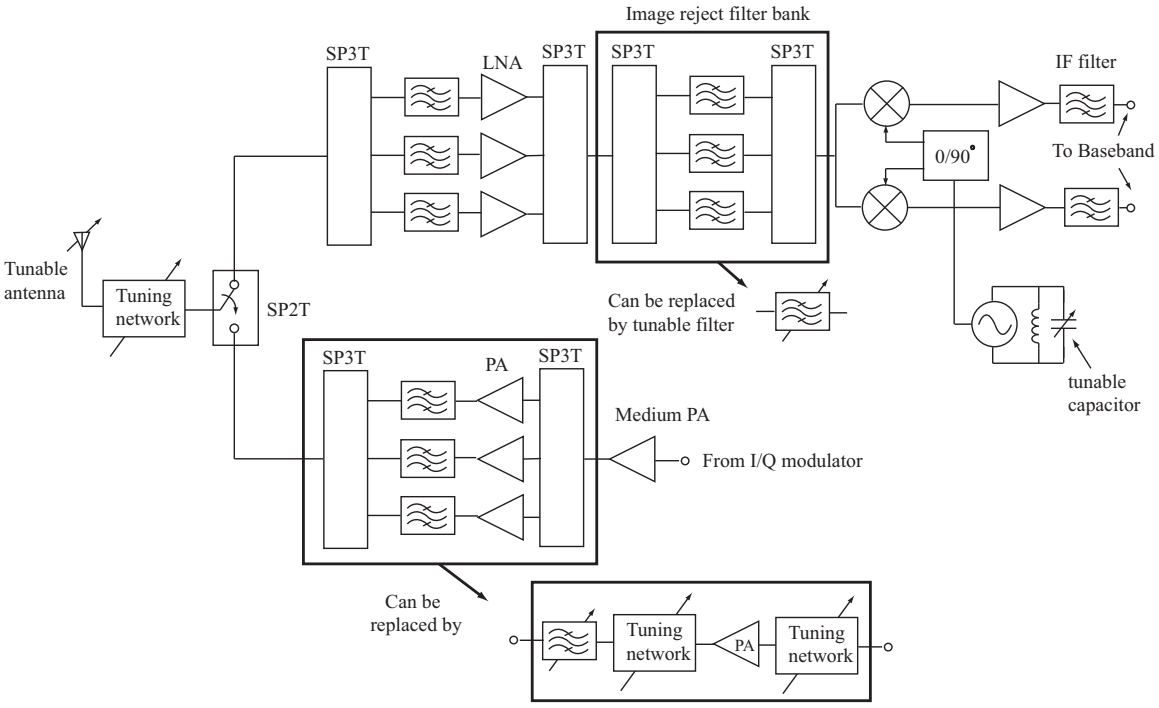

Figure 1.1: The block diagram of a multi-band wireless systems [1].

limiting factors for their use in modern wireless systems. They have been in use as front-end filters for microwave instrumentation systems, and for electric warfare and electric counter measure transceivers. The design principles for multi-state YIG filters from 0.5 to 40 GHz are given in [7–9].

The BST filters employ Barium Strontium Titanate thin film capacitors as tuning elements. These ferro-electric materials have two phases of operation: ferro-electric phase and para-electric phase. The device maintains high relative dielectric constant ($\epsilon_r \backsim 300$) in para-electric phase and the tunability of the dielectric constant with applied electric field enables electrically tunable capacitors for a DC-bias of 2-5 V [13]. Recently, a tunable filter utilizing improved-Q BST capacitor was reported with frequency range and insertion loss of 176 to 276 MHz and 3 dB, respectively [11].

The Schottky-diode filters utilize reverse bias diodes as tuning elements. The main advantages of these devices are their small size and fast tuning speed. The tuning speed of this technology is limited by the biasing network and can be on the order of nanoseconds. Their limiting factors are power handling and non-linearities. At large input signal, the turn

on of reversed biased diodes results in clipping and creates harmonics and sub-harmonics, and limits the filter dynamic range. The Q of the typical varactor diodes is only 30-100, and this limits their use in narrow-band filter design at microwave frequency. Varactor diode filters with frequency range of 0.5 to 5.0 GHz have been reported and they show a considerable amount of loss [12, 14, 15].

An RF-MEMS (Micro-Electro-Mechanical-Systems) switch is a electro-mechanical device which is able to change its capacitance value with an applied DC voltage. The capacitance change can be either digital or analog or can be both. The RF-MEMS switch itself has a high Q (150-300) at RF and millimeter wave frequencies, and a very low distortion level [16], and this is a huge advantage over its varactor diode counterparts. The switching time of this device is 0.5-50 μs depending on the size of the MEMS capacitive switch. The filters utilizing these MEMS devices have advantages of low loss and low distortion levels, however the tunable filter reported so far have a $Q < 100$ [17–26], and this is due to the resonator Q and the bias-line loss in the multi-bit capacitance network.

The main part of this thesis is devoted to the realization of high-Q (> 100) tunable filters utilizing RF-MEMS capacitance networks. A distributed filter topology is used for the filter design with a new admittance matrix design method. The dominant electric-field to bias-line coupling loss in the multi-bit RF-MEMS capacitance network is first addressed and a novel multi-bit orthogonal high-Q RF-MEMS capacitance network is introduced. A significant improvement ($Q_u \sim$ 85-170) in the tunable filter performance is achieved by reducing the coupling between the resonant electric field and bias-lines with an orthogonal bias network configuration.

A further enhancement of the tunable filter performance ($Q_u > 500$) is achieved using an evanescent-mode cavity resonator and a high-Q RF-MEMS cantilever-switch network. In this design, an RF-MEMS tunable is installed in the modular evanescent-mode cavity resonator assembly, and a dramatic increase in the resonator Q to 400-800 is obtained at 4-6 GHz. Details will be given in chapter 7. Table 1.1 summarizes the performance of the 5 different technologies for the tunable filters. It is seen that RF-MEMS achieves the best compromise between power handling, tuning speed, achievable Q and power consumption.

Fig. 1.2 shows the block diagram of the Sirific 7-band radio chip. This chip requires 19

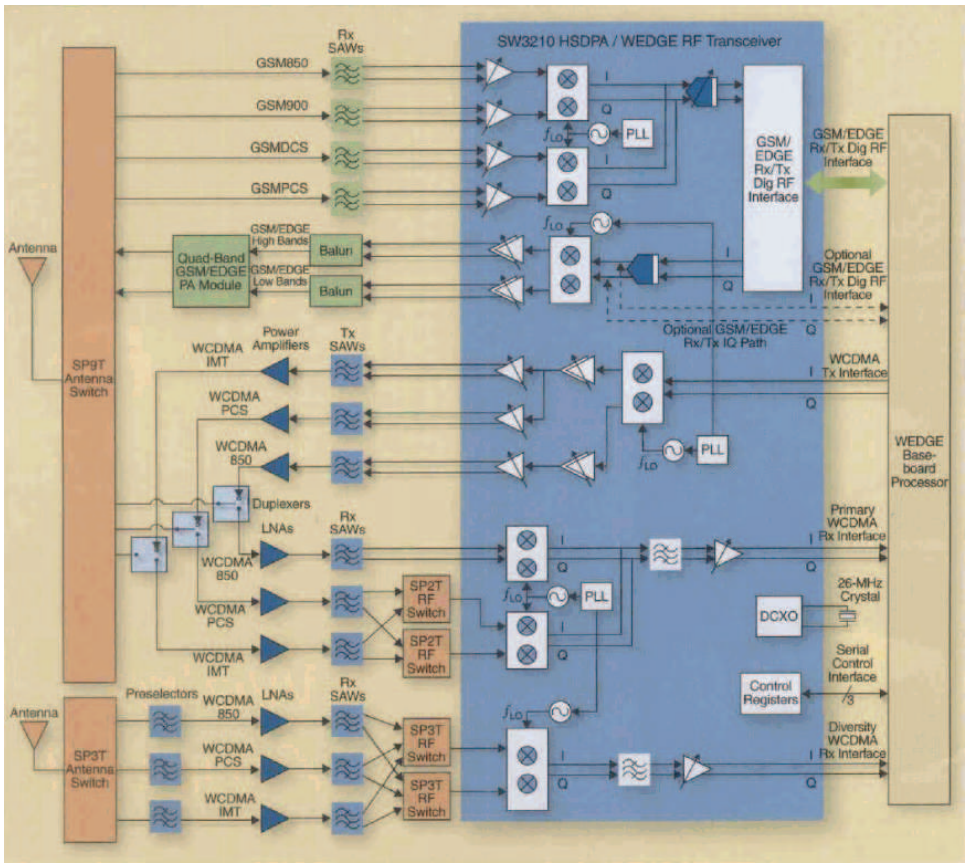

Figure 1.2: The Sirific 7-band radio chip [2].

Table 1.1: Typical performance parameters of microwave tunable bandpass filters.

Parameter	Mech.	YIG	PIN/Schottky	BST	RF − MEMS
I.L. (dB)	$0.5-2.5$	$3-8$	$3-10$	$3-5$	$3-8$
Q_u	>1000	>500	<50	<100	<100
power handling (W)	500	2	0.2	–	2
bandwidth (%)	$0.3-3$	$0.2-3$	>4	>4	$1-10$
IIP_3 (dBm)	very high	<30	<30	<30	>50
tuning speed (GHz/ms)	very low	$0.5-2$	10^3	–	10^2
powerconsumtion	high	high	medium	0	0
miniaztrization	No	No	Yes	Yes	Yes

external filters, 3 external power amplifiers, and 6 external low noise amplifiers. With RF-MEMS technology, the filters can be replaced by 6 tunable filters, a single power amplifier (with a reconfigurable matching network), and 2 low noise amplifiers. This is a dramatic reduction in front-end complexity for multi-standard cell phones, and can only be possible using RF-MEMS technology.

1.2 RF-MEMS technology

Micro-Electro-Mechanical Systems (MEMS) is the integration of mechanical elements, sensors, actuators, and electronics on a common silicon substrate using micro-fabrication technology. While the electronics are fabricated using integrated circuit (IC) process sequences (e.g., CMOS, Bipolar, or BICMOS processes), the micro-mechanical components are fabricated using compatible "micro-machining" processes that selectively etch away parts of the silicon wafer or add new structural layers to form the mechanical and electromechanical devices.

The possible applications of the MEMS technology are numerous such as biotechnology, communications, accelerometers, and etc... and the devices working at microwave frequency are called RF (Radio Frequency) MEMS. High frequency circuits benefit considerably from the advent of the RF-MEMS technology. Due to its outstanding performance, it has immense potential for commercial and defense applications. One of the most important example in RF/Microwave applications is an RF-MEMS switch. It is essentially a miniature device which use mechanical movement to achieve an open or short circuit in a transmis-

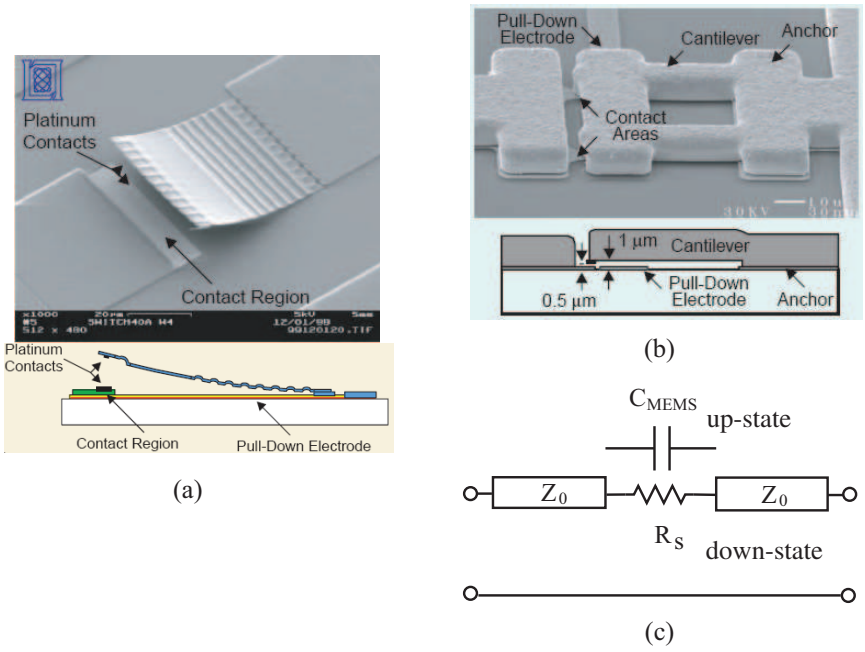

Figure 1.3: Series metal-contact switches developed by (a) Lincoln Laboratory [3], (b) Northwestern/Radant MEMS/Analog Device [4], and (c) their equivalent circuit models.

sion line. RF-MEMS switches can be categorized by two configurations: metal-contact and capacitive-contact. Fig. 1.3 shows two metal-contact series switches developed by Lincoln Laboratory [3], and Northwestern/Radent MEMS/Analog Devices [4], and Fig. 1.4 shows a capacitive shunt switch developed by Raytheon [27].

In the up-state positions, the input impedance of series switches is very high and becomes an open circuit ($C_{up} < 10$ fF) whereas the down-state position results in a near short circuit ($R_s < 2\ \Omega$) through the metal-to-metal contact.

The capacitive switches use a metal-to-dielectric contact with C_d=0.5-2 pF, and as a result, the down-state input impedance of the switch becomes very low, and the up-state to down-state capacitance ratio ($C_r = C_{down}/C_{up}$) is 20-100. For applications such as loaded-line phase shifters, reconfigurable matching networks, and tunable filters, the capacitance ratio of the MEMS switch is scaled down to 3-5 by connecting a fixed capacitor in series with the MEMS switch. For an application which requires continuous capacitance variation, analog MEMS switch varactors are developed[28].

There are several ways to actuate RF-MEMS devices such as electrostatic, thermal,

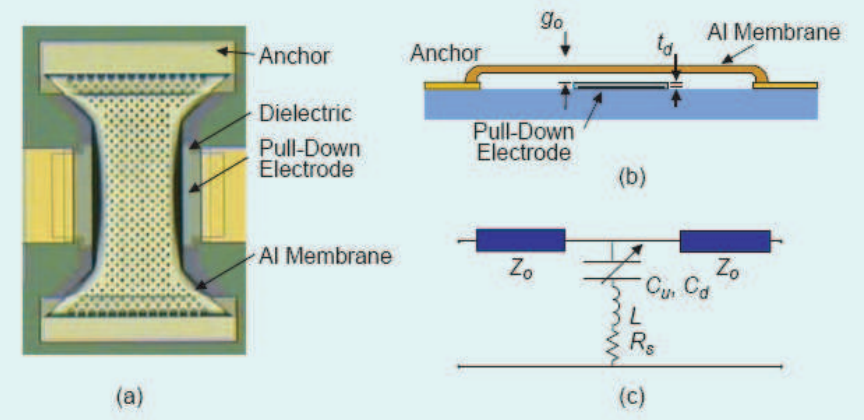

Figure 1.4: Shunt capacitive switch developed by Raytheon: (a) top view, (b) side view, and (c) the equivalent circuit model [1].

magnetostatic or piezoelectric. The electrostatic force actuation is the most widely used due to its simplicity, compactness and low power consumption. The switching speed (1-100 μs) and low power handling capability (< 1-2 W) can be disadvantages in these devices, however they show excellent performance such as:

1. *Very Low Insertion Loss:* MEMS switches are simple micro-scale suspended metal structures with only the conductor losses, and therefore, they have very low loss (0.05-0.2 dB from 1-100 GHz).

2. *Very High Linearity:* MEMS switches cannot respond to a fast varying electronic signal (f>1 MHz) due to the mechanical nature of the device, and therefore they are very linear and produce very low intermodulation products. (30-50 dB better than FET switches, PIN diodes or BST varactors counterparts).

3. *Very Low Power Consumption:* Despite the high actuation voltage (20-100 V) requirement, there is virtually no DC current flowing in the device, and therefore MEMS switches have very low DC power dissipation.

4. *Very High Isolation:* MEMS metal-contact switches have air as a dielectric in the up-state, and therefore have very small off-state capacitance (C_{up}=1-6 fF) resulting in an excellent isolation up to 40 GHz.

Table 1.2 summarizes the performance comparison of MEMS switches with the current standard technology such as FET switches and PIN diodes. [1]. The cutoff frequency

Table 1.2: Performance comparison of FET switches, PIN diodes and RF-MEMS electrostatic switches [1].

Parameter	RFMEMS	PIN	FET
Voltage (V)	$20-100$	$\pm 3-5$	$3-5$
Current (A)	0	$3-20$	0
Power Consumption (mW)	$0.05-0.1$	$5-100$	$0.05-0.1$
Switching Time	$1-300\ \mu s$	$1-100\ ns$	$1-100\ ns$
C_{up}(Series) (ff)	$2-12$	$40-80$	$70-140$
R_s(Series) (Ω)	$0.5-2$	$2-4$	$4-6$
Capacitance Ratio	$20-300$	10	N/A
Cutoff Freq. (THz)	$20-80$	$1-4$	$0.5-2$
Isolation($1-10$ GHz)	V.High	High	Medium
Isolation($10-40$ GHz)	V.High	Medium	Low
Isolation($60-100$ GHz)	High	Medium	None
Loss($1-100$ GHz) (dB)	$0.05-0.2$	$0.3-1.2$	$0.4-2.5$
Power Handling (W)	<5	<10	<10
IIP_3 (dBm)	$60-80$	$27-45$	$27-45$

mentioned in the table is the figure of merit for a series switch and $f_c = 1/(2\pi R_s C_{up})$.

Most of the current research activities in RF-MEMS switch are concentrated on improving the power-handling capability, reliability, packaging and switching time of the MEMS-based structures. The most recent RF-MEMS research results show a power handling of 1-7 W, the reliability of >100 billion cycles at 100 mW RF power (even >1000 billion), a switching speed of <10 μsecond, and an inexpensive in-situ packaging []. The RF-MEMS can also be built on glass or low-cost silicon substrates, and does not require MBE (Molecular Beam Epitaxy) or MOCVD (Metal Organic Chemical Vapor Deposition). These advantages along with IC-processing compatibility make RF-MEMS an enabling technology for low cost and high performance systems in both military and commercial applications, which include wide-band tunable/switchable filters, antenna beam-steering systems, reconfigurable matching networks, reconfigurable array antennas, and satellite communications.

1.3 Thesis overview

Chapter 2 presents a 2.1 GHz miniature planar two-pole microstrip filter with independent electric and magnetic coupling. The independent coupling allows separate control

of two transmission zeroes and result in a sharp filter skirt. The two-pole filter occupies an area of 6.6×4.6 mm^2 (30 mm^2) on an ϵ_r = 10.2 substrate, and shows a 5% bandwidth (100 MHz) and an insertion loss of 1.4 dB. The filter unloaded Q is 150 at 2.1 GHz which is much better than compatible filters done in LTCC technology.

In Chapter 3, low-loss tunable filters on ϵ_r=2.2, 0.787 mm Duroid with three different fractional-bandwidth variations are presented. A detailed analysis for realizing predefined bandwidth characteristics is presented, and a design technique to take into account the source and load impedance loading is discussed. It is found that *independent* electric and magnetic coupling makes it possible to realize three different coupling coefficient variations with the same filter structure. The proposed topology is different from the comb-line design in that all three filters have identical electrical lengths, the same varactors and the same filter Q values. Three different filters are built using Schottky varactor diodes with a tuning range of ∼850 MHz to ∼1400 MHz. The constant fraction-bandwidth filter has a 1-dB bandwidth of 5.4 ± 0.3 % and an insertion loss of 2.88-1.04 dB. The decreasing fractional-bandwidth filter shows a 1-dB bandwidth decrease from 5.2 % to 2.9 % with an insertion loss of 2.89-1.93 dB (this is effectively an 40-45 MHz constant absolute-bandwidth filter). The increasing fractional-bandwidth filter shows a 1-dB bandwidth increase from 4.3 % to 6.5 % with an insertion loss of 3.47-1.18 dB. The measured Q of the filters are between 53 and 152 from ∼850 MHz to ∼ 1400 MHz. The measured IIP3 ranges from 11.3 dBm to 20.1 dBm depending on the bias voltage. To our knowledge, these planar tunable filters represent state-of-the-art insertion loss performance at this frequency range.

Chapter 4 presents low loss 3.6 GHz fixed and 5.15-5.70 GHz RF-MEMS switchable filters on quartz substrates. Detailed design equations for the capacitively-loaded coupled open-loop $\lambda/2$ resonators are given and the realization of the tunable filter using these equations is discussed. The use of capacitively-loaded coupled open-loop $\lambda/2$ resonators made it possible to realize the fixed and switchable filters with unloaded Q of around 150 resulting in a 1.4 dB insertion loss. The measured 1-dB bandwidth for the 3.6 GHz fixed and 5.15-5.70 GHz switchable filters were 4% and 5%, respectively. To our knowledge, this represents the lowest loss planar tunable filter to-date in the 4-6 GHz frequency range.

Chapter 5 presents a low-loss 4-6 GHz 3-bit tunable filter on a quartz substrate using

a high-Q 3-bit orthogonal RF-MEMS capacitance network. Detailed design equations for the capacitively-loaded coupled $\lambda/2$ resonators and with capacitive external coupling and source-load impedance loading are discussed. Measurements show an unloaded-Q of 85-170, an insertion loss of 1.5-2.8 dB, and a 1-dB bandwidth of 4.35 $\pm$ 0.35% at 4-6 GHz. The measured IIP3 and 1-dB power compression point at 5.91 GHz are $>$ 40 dBm and 27.5 dBm, respectively. The unloaded Q can be improved to 125-210 with the use of a thicker bottom electrode. To our knowledge, this is the highest Q tunable planar filter to-date at this frequency range.

In Chapter 6, a 5.10-5.80 GHz CPW RF-MEMS switchable on a Si-Substrate is presented. The filter response which corresponds to either the up or down-state position of the RF-MEMS switch has one transmission zero, and these transmission zeroes switch their locations from the higher to the lower side of the pass-band as the filter state switches. Detailed design equations for this CPW filter are given and the coupling sign change (magnetic to electric) for this mirrored transmission zero is discussed. The measured up and down-state frequencies are 5.95 GHz and 5.21 GHz, respectively, and the corresponding losses are 9.3 dB for both states. The measured results have about 7 dB more loss than the simulated ones (2.3 dB), and this is due to the use of 5 Ω-cm resistivity wafer instead of the originally intended 3-10 kΩ-cm high resistivity wafer. The up and down-state responses show a transmission zero at 5.40 GHz and 5.63 GHz, respectively, and with these mirrored transmission zeroes, the isolation between the two frequency bands are enhanced by more than 10 dB.

In chapter 7, a very high-Q evanescent-mode tunable filter with a novel high-Q RF-MEMS cantilever-switch capacitance network is presented. The evanescent-mode cavity resonator design methodology is discussed and its full-wave implementation is shown. The loss mechanisms of the RF-MEMS capacitance network in the high-Q evanescent-mode resonator are investigated and a bias-line metal-bridge cover and an RC network in the bias-path are introduced. The evanescent-mode filter is constructed as a modular assembly, and this eases the installation of the RF-MEMS chip in the cavity. The measured filter frequencies with the fixed interdigital capacitance chips are 4.19-6.59 GHz, and their insertion losses and Q_u are 2.46-1.28 dB, and 538-845, respectively.

Chapter 8, is the conclusion and future work chapter. It is seen that we have nearly achieved the limit of achievable Q's using planar circuits, but the tunable filter area is still wide open for 3-dimensional implementations.

Chapter 2

A Miniature 2.1 GHz Low Loss Microstrip Filter with Independent Electric and Magnetic Coupling

2.1 introduction

Miniature filters at wireless communication frequency band (800 MHz - 2.5 GHz) are a very active area of research due to the relatively large size of the components, and typical implementations on microstrip substrates utilize parallel coupled lines. Usually, these filters make use of $\lambda/2$ or $\lambda/4$ resonators and have an insertion loss of 1-2 dB for a 5% bandwidth [29]. Because of the large size of the filter (over 20×20 mm^2), they are rarely used in commercial wireless communication frequency bands. The LTCC (low-Temperature-Cofired-Ceramic) designs are more successful than microstrip designs in size but they have poor insertion loss characteristic. Their typical size is 5×4 mm^2 with 2-3 dB of loss for 2-pole 5% filter [30].

The most successful filters in wireless communications are Saw filters and BAW/FBAR (Bulk-Acoustic-Wave/Film-Bulk-Acoustic-Resonator) filters. They have a very small size (3×2 mm^2) and low insertion loss (1-2 dB), but require a specialized technology and have power handling problem at $>$ 2W [31][32].

This paper presents a miniature filter which is compatible with low-cost printed substrates. It is based on a folded structure with two loading capacitors and shorted resonators. It has independent electric and magnetic coupling sections which enables the control of two transmission zeroes. This new coupling structure gives the freedom to choose the resonator admittance, and therefore the width of the microstrip resonator can be optimized for low-loss performance.

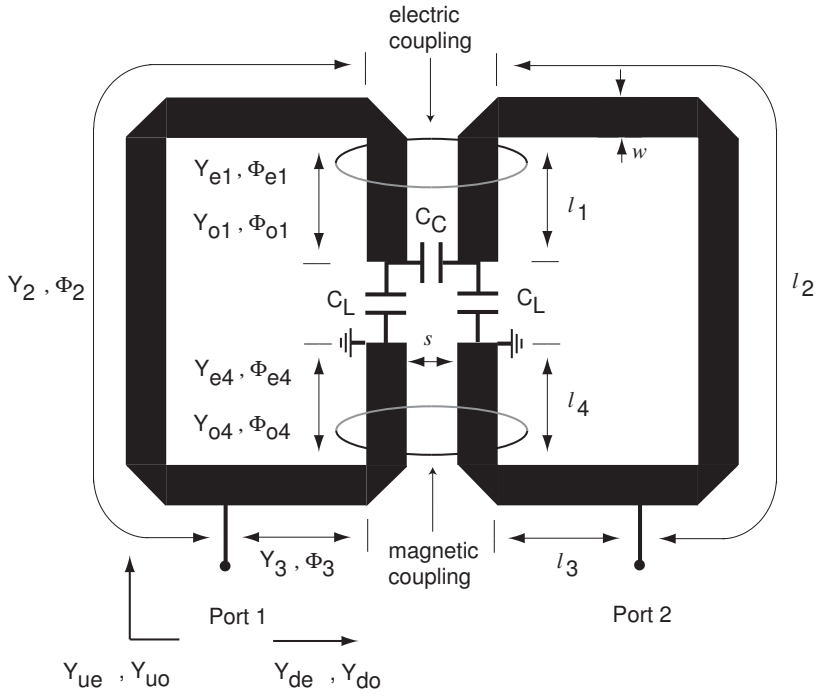

Figure 2.1: Electrical circuit model of the miniature filter.

2.2 Design

Fig. 2.1 shows the layout of the proposed miniature filter, and a circuit model was built to extract the design parameter of this filter. As can be seen in Fig. 2.1, the two different coupling regions are characterized by even and odd-mode admittances.

The even-mode admittance seen from port 1 to the upper-half section of the filter is defined by:

$$Y_{ue} = Y_2 \frac{Y_{e1} \dfrac{j\omega C_L + jY_{e1} \tan \phi_{e1}}{Y_{e1} - \omega C_L \tan \phi_{e1}} + jY_2 \tan \phi_2}{Y_2 + jY_{e1} \dfrac{j\omega C_L + jY_{e1} \tan \phi_{e1}}{Y_{e1} - \omega C_L \tan \phi_{e1}} \tan \phi_2} \tag{2.1}$$

When the odd-mode is excited, there exists a virtual ground at the plane of symmetry between the resonators. Therefore the overall capacitance value at the open end terminal is the sum of loading capacitance, C_L, and two times the coupling capacitance, C_C. The

resulting odd-mode admittance from port 1 to the upper-half section, Y_{uo}, is:

$$Y_{uo} = Y_2 \frac{\frac{Y_{o1}\, j\omega\,(C_L + 2C_C) + jY_{o1}\tan\phi_{o1}}{Y_{o1} - \omega\,(C_L + 2C_C)\tan\phi_{o1}} + jY_2\tan\phi_2}{Y_2 + jY_{o1}\frac{j\omega\,(C_L + 2C_C) + jY_{o1}\tan\phi_{o1}}{Y_{o1} - \omega\,(C_L + 2C_C)\tan\phi_{o1}}\tan\phi_2} \tag{2.2}$$

Similarly the even and odd-mode admittances for the lower-half of the resonator are Y_{de} and Y_{do}, respectively; with:

$$Y_{de} = Y_3 \frac{-jY_{e4}\cot\phi_{e4} + jY_3\tan\phi_3}{Y_3 + Y_{e4}\cot\phi_{e4}\tan\phi_3} \tag{2.3}$$

$$Y_{do} = Y_3 \frac{-jY_{o4}\cot\phi_{o4} + jY_3\tan\phi_3}{Y_3 + Y_{o4}\cot\phi_{o4}\tan\phi_3} \tag{2.4}$$

The admittance matrices of the upper-half section and lower-half section can be defined as Y_u and Y_d, respectively:

$$Y_u = \begin{pmatrix} \frac{Y_{ue} + Y_{uo}}{2} & \frac{Y_{ue} - Y_{uo}}{2} \\ \frac{Y_{ue} - Y_{uo}}{2} & \frac{Y_{ue} + Y_{uo}}{2} \end{pmatrix} \tag{2.5}$$

$$Y_d = \begin{pmatrix} \frac{Y_{de} + Y_{do}}{2} & \frac{Y_{de} - Y_{do}}{2} \\ \frac{Y_{de} - Y_{do}}{2} & \frac{Y_{de} + Y_{do}}{2} \end{pmatrix} \tag{2.6}$$

The two sections are connected in parallel and therefore the resulting admittance matrix of this filter can be found by:

$$Y = \begin{pmatrix} \frac{Y_{ue} + Y_{de} + Y_{uo} + Y_{do}}{2} & \frac{Y_{ue} + Y_{de} - Y_{uo} - Y_{do}}{2} \\ \frac{Y_{ue} + Y_{de} - Y_{uo} - Y_{do}}{2} & \frac{Y_{ue} + Y_{de} + Y_{uo} + Y_{do}}{2} \end{pmatrix} \tag{2.7}$$

The equivalent circuit model of the filter can be found from the calculated admittance matrix, and the circuit model in Fig. 2.2 shows the Π-network equivalence of the miniature filter. The Y_{11} represents the two resonators and the Y_{12} Π-network represents the coupling between them.

The network also needs to satisfy several conditions: At resonance, the admittance of the resonator should be zero and the Y_{12} Π-network should have the coupling value of the

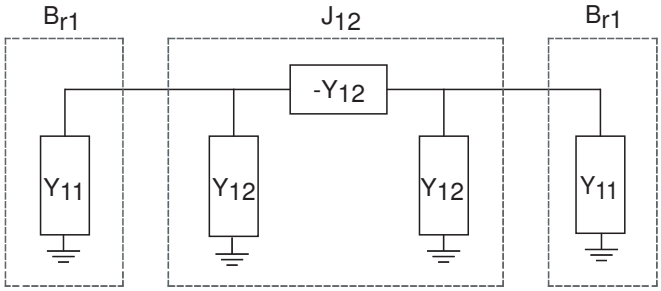

Figure 2.2: Equivalent Π-network of the miniature filter.

Table 2.1: Design parameters of the 2-pole 6% filter on a 1.27 mm, $\epsilon_r = 10.2$ substrate (dimensions are in mm, impedances are in Ω).

w	s	$l1$	$l2$	$l3$	$l4$
0.8	0.4	1	5.2	0.8	1
Z_{e1}	Z_{o1}	Z_2	Z_3	Z_{e4}	Z_{o4}
76.0	37.9	62.4	62.4	76.0	37.9
$\epsilon_{eff_{e1}}$	$\epsilon_{eff_{o1}}$	ϵ_{eff_2}	ϵ_{eff_3}	$\epsilon_{eff_{e4}}$	$\epsilon_{eff_{o4}}$
7.25	5.55	7.27	7.27	7.25	5.55

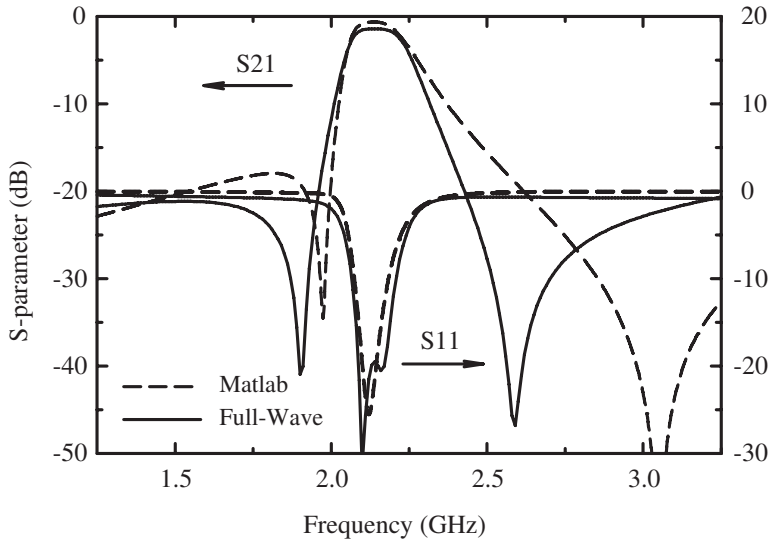

Figure 2.3: MATLAB and full-wave simulation of the 2-pole 6% filter.

prototype filter, $\pm J_{12}$. These relations can be expressed as:

$$Y_{11}(\omega_0) = 0, \quad Y_{12}(\omega_0) = J_{12} \tag{2.8}$$

where

$$J_{12} = \Delta\sqrt{\frac{b_1 b_2}{g_1 g_2}}, \quad b = \frac{\omega_0}{2}\frac{\partial B}{\partial \omega}, \quad B = Im(Y_{11}) \tag{2.9}$$

Solving the above equations is not easy because both Y_{12} and J_{12} are complicated functions of C_C and C_L. Fortunately, the coupling capacitance, C_C, and the loading capacitance, C_L, can be decoupled from the slope parameter b if the input terminal is redefined at the open end. This will not change the filter characteristics because it is still not externally coupled yet. The external coupling is realized by tapping input and the tapping position which gives right amount of external coupling can be found by:

$$\frac{b}{Y_0} = Q_e = \frac{g_0 g_1}{\Delta} \tag{2.10}$$

The control of upper and lower transmission zeroes is possible by choosing circuit parameters which satisfy (8), $Y_{12}(\omega_{p1}) = 0$, and $Y_{12}(\omega_{p2}) = 0$ simultaneously. These circuit parameters include the even and odd-mode admittances and electrical lengths of the coupled sections, and the admittance and electrical length of the uncoupled resonator section. This independent electric and magnetic coupling configuration gives five more degrees of freedom than the conventional comb-line coupling structure and leads to a different solution set of circuit parameters, which enable the separate control of the two transmission zeroes.

A 6% bandwidth 0.2 dB equal ripple two-pole filter centered at 2.1 GHz was designed using the described topology. The detailed design parameters are listed in Table 6.1. The calculated coupling and loading capacitances are $C_C = 0.17$ pF and $C_L = 0.85$ pF, respectively. Electric coupling is selected in order to get transmission zeroes below and above the pass band. Also, full-wave (HFSS) simulations were performed to validate the analytical (MATLAB) simulations [33, 34]. In the full-wave simulations, the calculated capacitance values of 0.17 pF and 0.85 pF did not give the desired center frequency. The readjusted

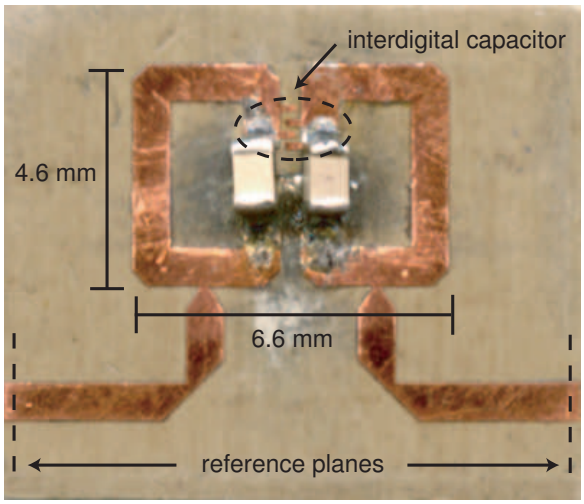

Figure 2.4: Fabricated miniature filter on a Duroid substrate ($\epsilon_r = 10.2$).

capacitance values for the desired full-wave response are $C_C = 0.08$ pF and $C_L = 0.75$ pF. Both values of capacitances are lower than calculated because the analytical circuit model does not take into account the fringing field at the open end of the resonators, the mitered corners of the folded microstrip structure, and the parasitic effect of the grounding via.

Fig. 2.3 is a comparison between the Matlab simulation with calculated parameters and the full-wave simulation of the physical structure. As can be seen, the location of the higher transmission zero is different. The transmission zero in the upper stop-band occurs when the voltage distribution is a maximum at the open end of the resonator and a minimum at the tapping location. This length is longer in the full-wave simulation because of the mitered corners. In addition, because of the microstrip implementation, the even and odd-mode phase velocities are not constant over frequency as assumed in the circuit model (these effects cause only a small shift in the transmission zero in the lower stop band).

2.3 Fabrication and Measurement

The filter was fabricated on a 1.27 mm Duroid substrate ($\epsilon_r = 10.2$, Roger RT/Duroid 6010LM) using a copper etching process (Fig. 2.4) [35]. The loading capacitances were implemented with lumped chip capacitors (1.6×0.8 mm^2) and the small coupling capacitance was realized by an interdigital structure added between the open ends of the resonators.

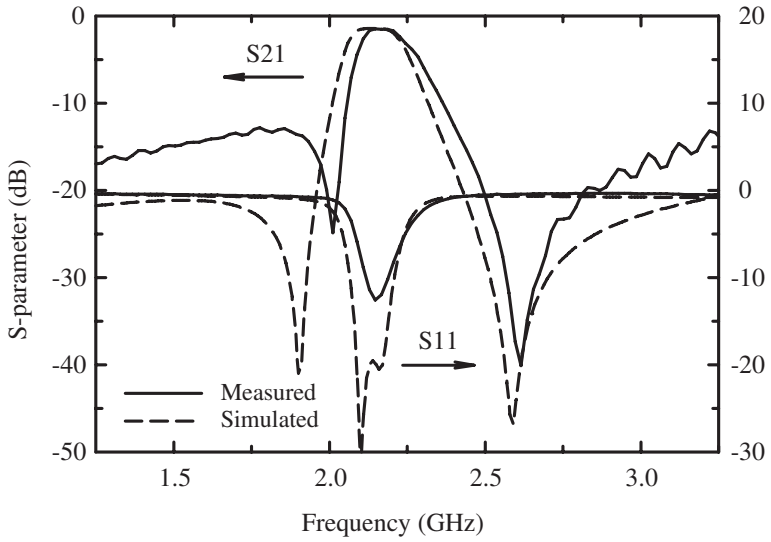

Figure 2.5: Measurement vs. simulation of the 2-pole 6% filter.

The chip capacitors are ATC 600S and have a Q of 200 at 2 GHz [36].

The measured insertion loss is 1.4 dB with a 5% 1-dB bandwidth. The center frequency is 2.17 GHz. A slight deviation of the center frequency can be accounted for by the tolerance ($\pm$ 0.1 pF) of the chip capacitors that are used as loading capacitances. The measured bandwidth is slightly smaller than the simulated design because of the over-etched interdigital coupling capacitor.

The simulated and measured results are shown in Fig. 2.5. The discrepancy in the lower stop band attenuation level is about 10 dB. This is because the length (1.6 mm) of chip capacitor is longer than the gap (1.0 mm) between the open and shorted end of the resonator. The filter was re-simulated with the mounting position of the capacitors adjusted by increasing the distance between the internal ports from 1.0 mm to 1.4 mm. With this adjustment, the measured and simulated results show excellent agreement (Fig. 2.6).

A circuit simulation done with ADS on the filter with the full-wave design parameters shows an *rms* RF voltage and current across the chip capacitor of 28-56 V and 310-620 mA respectively, for an input power of 1-4 W [37]. The chip capacitors can handle this voltage and current [36] and therefore this filter topology is suitable for a wide range of wireless standards.

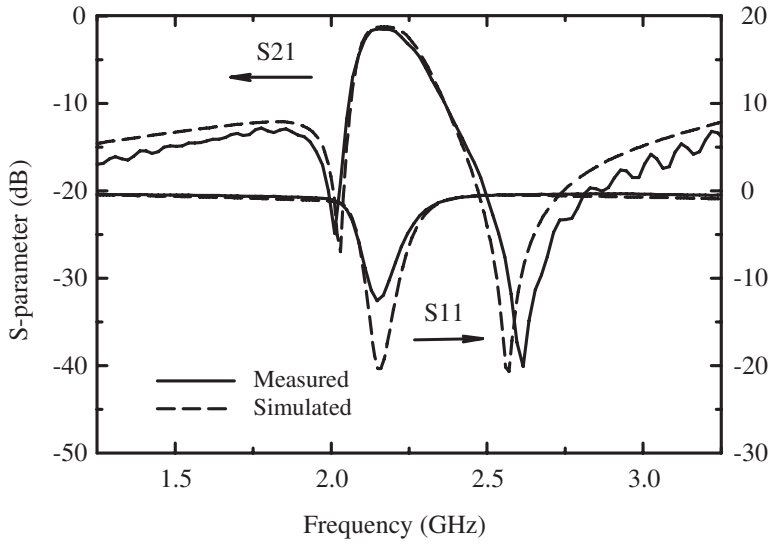

Figure 2.6: Simulation vs. measurement after adjusting the chip capacitor mounting location.

2.4 Conclusion

A miniature microstrip filter was designed and fabricated with 1.4 dB insertion loss and an unloaded Q of 150 (fitted to the measurements). Two transmission zeroes can be positioned above and below the pass band which give good attenuation characteristics. The location of the transmission zeroes are easy to adjust because of the independent electric and magnetic coupling scheme. A significant size reduction (6.6×4.6 mm^2) was accomplished using a novel folded resonator on a Duroid ($\epsilon_r = 10.2$) substrate. A similar filter on an $\epsilon_r = 38$ substrate with planar metal-air-metal capacitor would result in an area of 2.9×2.1 mm^2.

Chapter 3

Low-Loss Tunable Filters with Three Different Pre-defined Bandwidth Characteristics

3.1 introduction

Low-loss tunable filters are essential for modern wide-band communication systems. Tunable filters have been studied for almost three decades and most of them can be classified in three categories; YIG filters [10], varactor diode filters [12, 14, 15, 38], and RF-MEMS filters [17, 19, 23, 26]. YIG (Yttrium-Iron-Garnet) filters utilize the ferromagnetic resonance frequency change of YIG spheres with an externally applied DC magnetic field. These filters have multi-octave tuning ranges and a Q up to 10,000, however, their power consumption, tuning speed, size, and weight are limiting factors for their use in modern communication systems. Varactor diode filters utilize reverse-biased diodes with moderate Q (30-150). The tuning speed of this technology is limited by the varactor biasing network and can be on the order of nano-seconds. RF-MEMS (RF Micro Electro Mechanical Systems) filters utilize RF-MEMS capacitors and have high-Q at RF and millimeter frequencies (50-200), as well as very low distortion levels [16]. The limiting factor for these filters is currently the maturity of RF-MEMS technology. A tunable filter Q of 150 has been recently reported at 5.15-5.7 GHz [39].

Research in tunable filters has been mainly focused on the realization of frequency tuning. Hunter *et al.* [12] reported a varactor tuned filter at 3500-4500 MHz utilizing a comb-line filter topology with a 3-5 dB insertion loss and a 5.7-4.4% fractional-bandwidth. Brown *et al.* [14] realized a varactor tuned filter at 700-1330 MHz using an interdigital filter topology with an insertion loss and fractional-bandwidth of 5-2 dB and 10-16%, respectively. Recently, filters with both frequency and bandwidth tuning capabilities have

been reported [19], [15]. Young *et al.* developed an RF-MEMS tunable filter in the 860-1750 MHz frequency range using a lumped filter topology with a 7-3 dB insertion loss and a 7-42% fractional-bandwidth. Sanchez *et al.* [15] introduced a variable coupling reducer between comb-line resonators and realized bandwidth tuning with varactor diodes. In his work, mechanical capacitors are used as frequency tuners in the resonators. The filter shows a tuning range, insertion loss, and fractional-bandwidth of 450-850 MHz, 14-3 dB, and 2-18%, respectively.

In previous work, neither the change in bandwidth as the center frequency is tuned, nor how to manipulate this change have been studied intensively using distributed circuits. Hunter *et al.* [12] reported that a constant absolute-bandwidth tunable filter over an octave bandwidth is possible using a comb-line filter topology with a resonator's electrical length of 53°. The constant fractional-bandwidth filter is also possible using a comb-line filter topology, but the electrical length of the resonator becomes 23°, and this leads to significantly different loading capacitance and filter Q.

Park *et al.* [40] introduced a filter with independent electric and magnetic coupling using the admittance matrix method. The independent electric and magnetic coupling scheme makes it possible to manipulate the frequency-dependent coupling coefficient variation, and this leads to different pre-defined bandwidth variations versus frequency. Based on the independent electric and magnetic coupling filter topology, this paper presents three filters with three different bandwidth variations; constant fractional-bandwidth, decreasing fractional-bandwidth (constant absolute-bandwidth), and increasing fractional-bandwidth. The proposed topology is different from the comb-line design in that all three filters have identical electrical lengths, the same varactors and the same filter Q values. Due to the narrow-band nature of a lumped LC circuit model, a comprehensive distributed circuit design methodology using admittance matrices for the coupled resonators and the wide-band transformer is presented. Specific design considerations for the biasing and capacitive loading schemes are done in order to achieve excellent insertion loss and tuning range.

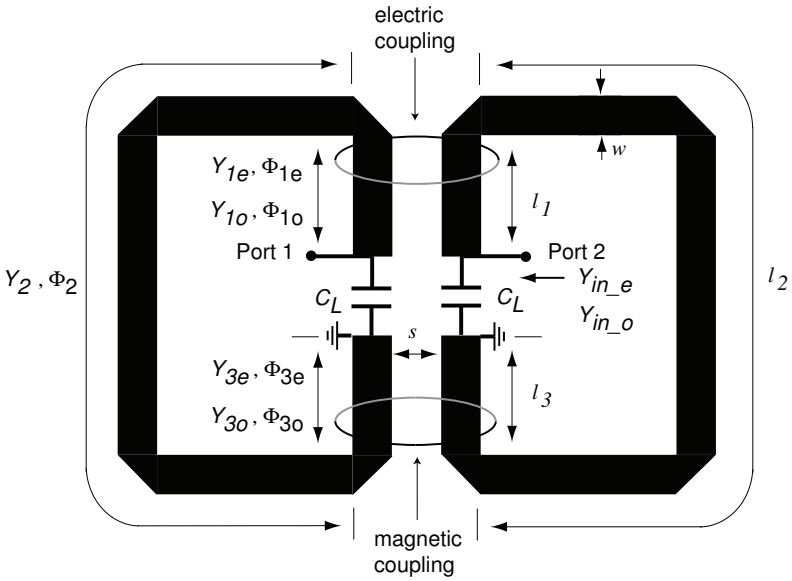

Figure 3.1: Electrical circuit model of the filter.

3.2 Design

3.2.1 Admittance Matrix of the Filter

Fig. 3.1 shows the schematic of the filter with an electric coupling section (Y_{1e}, Y_{1o}) and a magnetic coupling section (Y_{3e}, Y_{3o}). The input even and odd-mode admittances, Y_{in_e}, Y_{in_o}, are

$$Y_{in\_e} = j\omega C_L + Y_{re} \tag{3.1}$$

$$Y_{in\_o} = j\omega C_L + Y_{ro} \tag{3.2}$$

where

$$Y_{re} = Y_{1e}\frac{Y_2\frac{-jY_{3e}\cot\phi_{3e} + jY_2\tan\phi_2}{Y_2 + Y_{3e}\cot\phi_{3e}\tan\phi_2} + jY_{1e}\tan\phi_{1e}}{Y_{1e} + jY_2\frac{-jY_{3e}\cot\phi_{3e} + jY_2\tan\phi_2}{Y_2 + Y_{3e}\cot\phi_{3e}\tan\phi_2}\tan\phi_{1e}} \tag{3.3}$$

$$Y_{ro} = Y_{1o}\frac{Y_2\frac{-jY_{3o}\cot\phi_{3o} + jY_2\tan\phi_2}{Y_2 + Y_{3o}\cot\phi_{3o}\tan\phi_2} + jY_{1o}\tan\phi_{1o}}{Y_{1o} + jY_2\frac{-jY_{3o}\cot\phi_{3o} + jY_2\tan\phi_2}{Y_2 + Y_{3o}\cot\phi_{3o}\tan\phi_2}\tan\phi_{1o}}. \tag{3.4}$$

The overall admittance matrix of the capacitively-loaded coupled resonators is

$$Y = \begin{bmatrix} \frac{Y_{in\_e} + Y_{in\_o}}{2} & \frac{Y_{in\_e} - Y_{in\_o}}{2} \\ \\ \frac{Y_{in\_e} - Y_{in\_o}}{2} & \frac{Y_{in\_e} + Y_{in\_o}}{2} \end{bmatrix} \tag{3.5}$$

$$= \begin{bmatrix} j\omega C_L + Y_{r11} & Y_{r12} \\ \\ Y_{r12} & j\omega C_L + Y_{r11} \end{bmatrix} \tag{3.6}$$

where

$$Y_{r11} = \frac{Y_{re} + Y_{ro}}{2}, \quad Y_{r12} = \frac{Y_{re} - Y_{ro}}{2}. \tag{3.7}$$

3.2.2 Design of the Filter

Calculating the loading capacitor, C_L, and the even-odd mode admittances

For the above network (Fig. 3.1), two conditions must be satisfied. One is the resonance condition and the other is the coupling condition. The conditions are

$$Im[Y_{11}(\omega_0)] = 0, \quad \frac{Im[Y_{12}(\omega_0)]}{b} = k_{12} \tag{3.8}$$

where

$$b = \frac{\omega_0}{2} \frac{\partial Im[Y_{11}(\omega_0)]}{\partial \omega}, \quad k_{12} = \frac{\Delta}{\sqrt{g_1 g_2}}. \tag{3.9}$$

To complete the filter network, the design parameters, $Y_{1e,o}$, Y_2, $Y_{3e,o}$, $\phi_{1e,o}$, ϕ_2, and $\phi_{3e,o}$ need to be determined and must satisfy (4.10). The design parameters above cannot be found uniquely by only the resonance and loading conditions because the design parameters have eight degrees of freedom. Therefore, it is necessary to independently choose parameters such as the resonator impedance. For simplicity, the loading capacitor, C_L, needs to be decoupled from (4.10), and that can be chosen after all of the other filter parameters are found.

From the resonance condition $Im[Y_{11}] = 0$: it follows that

$$C_L = -Im\left[\frac{Y_{r11}(\omega_0)}{\omega_0}\right]. \tag{3.10}$$

With the above result, b can be defined by

$$b = Im\left[\frac{\omega_0}{2}\frac{\partial Y_{r11}(\omega_0)}{\partial\omega} - \frac{Y_{r11}(\omega_0)}{2}\right]. \tag{3.11}$$

The coupling condition in (4.10) can now be rewritten as

$$\frac{Im[Y_{r12}(\omega_0)]}{Im\left[\frac{\omega_0}{2}\frac{\partial Y_{r11}(\omega_0)}{\partial\omega} - \frac{Y_{r11}(\omega_0)}{2}\right]} = \frac{\Delta}{\sqrt{g_1 g_2}}. \tag{3.12}$$

With a given filter specification, the design parameters can be determined from the above equations and C_L can be found using (4.15). It is possible to design a filter with several different sets of design parameters because the design parameters are not uniquely determined by (3.12). If the design parameters Y_2 and l_2 are chosen first, satisfying (3.12) becomes a problem of selecting the electric and magnetic coupling sections of the filter. These electric and magnetic coupling sections also have six degrees of freedom. Although all design parameter sets give exactly the same frequency response at ω_0, these coupling structures have different frequency variations as the resonance frequency is tuned. This plays an important role in realizing predefined bandwidth characteristics in tunable filters and will be discussed in detail in section D.

External Coupling of the Filter

The frequency change due to the variable loading capacitors affects the slope parameter, b, and the coupling coefficient, k, of the filter, and therefore, external coupling elements which compensate for the frequency variation of b are required to maintain a good match over the entire tuning range. In this work, the impedance transformer network in Fig. 3.2 is suggested as an external coupling circuit. The resonator input admittance, Y_r^s, seen from

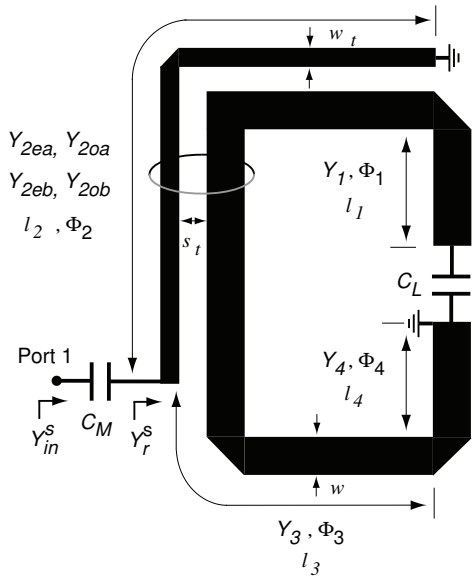

Figure 3.2: Electrical circuit model of the resonator with the external coupling circuit.

the input port before the matching capacitor, C_M, is

$$Y_r^s = y_{22}^s + y_{23}^s \frac{y_{34}^s y_{42}^s - y_{44}^s y_{32}^s}{y_{33}^s y_{44}^s - y_{34}^s y_{43}^s} + y_{24}^s \frac{y_{43}^s y_{32}^s - y_{33}^s y_{42}^s}{y_{33}^s y_{44}^s - y_{34}^s y_{43}^s} \tag{3.13}$$

where

$$y_{22}^s = -j \frac{Y_{2ea} + Y_{2oa}}{2} \cot \phi_2 \tag{3.14}$$

$$y_{23}^s = y_{32}^s = j \frac{Y_{2ea} - Y_{2oa}}{2} \csc \phi_2 \tag{3.15}$$

$$y_{34}^s = y_{43}^s = j \frac{Y_{2eb} + Y_{2ob}}{2} \csc \phi_2 \tag{3.16}$$

$$y_{42}^s = -j \frac{Y_{2ea} - Y_{2oa}}{2} \cot \phi_2 \tag{3.17}$$

$$y_{33}^s = -j \frac{Y_{2eb} + Y_{2ob}}{2} \cot \phi_2 + j Y_1 \frac{\omega C_L + Y_1 \tan \phi_1}{Y_1 - \omega C_L \tan \phi_1} \tag{3.18}$$

$$y_{44}^s = -j \frac{Y_{2eb} + Y_{2ob}}{2} \cot \phi_2 + j Y_3 \frac{-Y_4 \cot \phi_4 + Y_3 \tan \phi_3}{Y_3 + Y_4 \cot \phi_4 \tan \phi_3}. \tag{3.19}$$

The overall input admittance, Y_{in}^s, is then,

$$Y_{in}^s = \frac{j\omega C_M Y_r^s}{j\omega C_M + Y_r^s}. \tag{3.20}$$

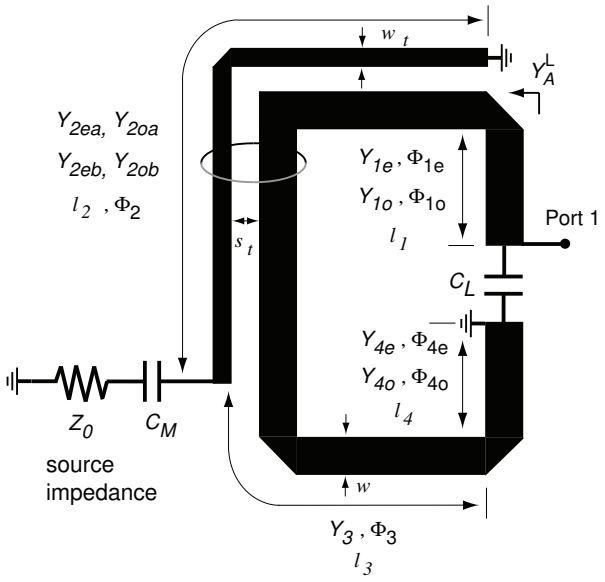

Figure 3.3: Electrical circuit model of the resonator with source and load impedance loading.

The transformer coupled section, l_2, was assumed to be homogeneous to make the analysis simpler. The detailed analysis of inhomogeneous asymmetric coupled lines is available in the literature, e.g., [41]. Once Y_{in}^s is found, Q_{ext} is

$$Q_{ext}^s = \frac{b^s}{Y_0} \tag{3.21}$$

where

$$b^s = \frac{\omega_0}{2} \frac{\partial Im[Y_{in}^s(\omega_0)]}{\partial \omega}. \tag{3.22}$$

By properly choosing the transformer section parameters, Y_{2ea}, Y_{2oa}, l_2, and C_M, one can achieve a relatively small variation in Q_{ext} over the whole tuning range.

3.2.3 Design with the Source and Load Impedance Loading

The introduction of the wide bandwidth transformer coupling section requires a small modification to the filter design. The parallel resonance frequency, f_0^s, given by $Im[Y_{in}^s] = 0$ is slightly lower than the design frequency, f_0. The distributed loading effect of the coupled transformer section, l_2, as well as C_M, adds to the susceptance of the original filter circuit

and this additional susceptance value reduces the resonance frequency. One should note that neither f_0 nor f_0^s is the actual resonance frequency of the filter when the filter circuit is completed with the source and load impedances. The load and source impedances are coupled through external coupling circuits and give a complex admittance. This complex loading results in a frequency shift in the filter. To accounts for this complex admittance loading in the filter design, a new model is developed as shown in Fig. 3.3.

The new model includes an input port at the open end of the resonator and the even and odd-mode coupling sections that determine the coupling coefficient (k_{12}) value of the filter. The even and odd-mode input admittances of the resonator seen from the l_1 section to the l_2 section, Y_{Ae}^L, Y_{Ao}^L, are

$$Y_{Ae}^L = y_{33}^L + y_{32}^L \frac{y_{24}^L y_{43}^L - y_{44e}^L y_{23}^L}{y_{22}^L y_{44e}^L - y_{24}^L y_{42}^L} + y_{34}^L \frac{y_{42}^L y_{23}^L - y_{22}^L y_{43}^L}{y_{22}^L y_{44e}^L - y_{24}^L y_{42}^L} \tag{3.23}$$

$$Y_{Ao}^L = y_{33}^L + y_{32}^L \frac{y_{24}^L y_{43}^L - y_{44o}^L y_{23}^L}{y_{22}^L y_{44o}^L - y_{24}^L y_{42}^L} + y_{34}^L \frac{y_{42}^L y_{23}^L - y_{22}^L y_{43}^L}{y_{22}^L y_{44o}^L - y_{24}^L y_{42}^L}. \tag{3.24}$$

where

$$y_{22}^L = -j \frac{Y_{2ea} + Y_{2oa}}{2} \cot \phi_2 + \frac{j\omega C_M Y_0}{j\omega C_M + Y_0} \tag{3.25}$$

$$y_{23}^L = y_{32}^L = j \frac{Y_{2ea} - Y_{2oa}}{2} \csc \phi_2 \tag{3.26}$$

$$y_{33}^L = -j \frac{Y_{2eb} + Y_{2ob}}{2} \cot \phi_2 \tag{3.27}$$

$$y_{34}^L = y_{43}^L = j \frac{Y_{2eb} + Y_{2ob}}{2} \csc \phi_2 \tag{3.28}$$

$$y_{42}^L = y_{24}^L = -j \frac{Y_{2ea} - Y_{2oa}}{2} \cot \phi_2 \tag{3.29}$$

$$y_{44e}^L = -j \frac{Y_{2eb} + Y_{2ob}}{2} \cot \phi_2 + jY_3 \frac{-Y_{4e} \cot \phi_{4e} + Y_3 \tan \phi_3}{Y_3 + Y_{4e} \cot \phi_{4e} \tan \phi_3} \tag{3.30}$$

$$y_{44o}^L = -j \frac{Y_{2eb} + Y_{2ob}}{2} \cot \phi_2 + jY_3 \frac{-Y_{4o} \cot \phi_{4o} + Y_3 \tan \phi_3}{Y_3 + Y_{4o} \cot \phi_{4o} \tan \phi_3}. \tag{3.31}$$

The even and odd-mode admittances of the resonators, Y_{re}^L, Y_{ro}^L, seen from port 1 without C_L, are

$$Y_{re}^L = Y_{1e} \frac{Y_{Ae}^L + jY_{1e} \tan \phi_{1e}}{Y_{1e} + jY_{Ae}^L \tan \phi_{1e}} \tag{3.32}$$

$$Y_{ro}^{L} = Y_{1o}\frac{Y_{Ao}^{L} + jY_{1o}\tan\phi_{1o}}{Y_{1o} + jY_{Ao}^{L}\tan\phi_{1o}}. \tag{3.33}$$

Then, the overall admittance matrix of the filter becomes

$$Y^{L} = \begin{bmatrix} j\omega C_L + Y_{r11}^{L} & Y_{r12}^{L} \\ \\ Y_{r12}^{L} & j\omega C_L + Y_{r11}^{L} \end{bmatrix} \tag{3.34}$$

where

$$Y_{r11}^{L} = \frac{Y_{re}^{L} + Y_{ro}^{L}}{2}, \quad Y_{r12}^{L} = \frac{Y_{re}^{L} - Y_{ro}^{L}}{2}. \tag{3.35}$$

This filter is already coupled to the source and load impedances, and therefore Q_{ext} is

$$Q_{ext}^{L} = \frac{b^{L}}{Re[Y_{r11}^{L}(\omega_0)]} \tag{3.36}$$

where

$$b^{L} = Im\left[\frac{\omega_0}{2}\frac{\partial Y_{r11}^{L}(\omega_0)}{\partial\omega} - \frac{Y_{r11}^{L}(\omega_0)}{2}\right]. \tag{3.37}$$

The design of the filter with the external coupling circuit can be completed with the following two equations as well as the resonance condition ($Im[Y_{11}^{L}]$=0): the coupling equation and the matching equation. The coupling and matching equations are

$$\frac{Im[Y_{r12}^{L}(\omega_0)]}{b^{L}} = \frac{\Delta}{\sqrt{g_1 g_2}} \tag{3.38}$$

$$\frac{b^{L}}{Re[Y_{r11}^{L}(\omega_0)]} = \frac{g_0 g_1}{\Delta}. \tag{3.39}$$

When the l_1 and l_4 sections are uncoupled, the resonator becomes a single uncoupled one and it no longer has even and odd-mode resonance frequencies, ω_{0e}, and ω_{0o}. Because the uncoupled resonator slope parameter, b_u^{L}, and coupled resonator slope parameter, b^{L}, are almost identical, (3.39) can be simplified using the uncoupled resonator admittance, Y_r^{L}. Y_r^{L} is identical to Y_{re}^{L} or Y_{ro}^{L} when the coupled sections are replaced by uncoupled sections

Table 3.1: Filter Parameters for Three Different Frequency Dependence of k_{12} (Impedances are in Ω, dimensions are in mm, $\varepsilon_r = 2.2$, 0.787 mm Substrate is Assumed, FBW is fractional-bandwidth)

	electric $Z_{1e}/Z_{1o}/l_1$	magnetic $Z_{3e}/Z_{3o}/l_3$	Z_2/l_2
constant FBW	64.7/45.7/2.70	84.2/39.5/3.40	56.3/28.0
decreasing FBW	68.7/35.3/2.70	84.2/39.5/3.60	56.3/27.8
increasing FBW	59.5/53.5/2.70	84.2/39.5/3.45	56.3/27.9

as is in Fig. 3.2. Once the design parameters with the uncoupled resonator are found, the coupled section parameters, $Y_{1e,o}$, $Y_{4e,o}$, l_1, and l_4 can be determined using (3.38).

3.2.4 Realizing Predefined Frequency Dependence of the Coupling Coefficient

The amount of coupling can be realized by choosing the even and odd-mode coupled sections, l_1 and l_4. The net coupling of this filter is given by the difference between the magnetic and electric coupling. Because the electrical length of this filter is smaller than 90°, the net coupling is magnetic. The rate of increase of the electric coupling in the l_1 section is larger than the increase in the magnetic coupling in the l_4 section. Therefore, when the electric coupling amount is adjusted, the variation of the net coupling is controlled in a more deterministic way.

Fig. 3.4 shows three different frequency dependence characteristics of k_{12}. Each plot is created using (3.12) with different sets of $Y_{1e,o}$, Y_2, $Y_{3e,o}$, l_1, l_2, and l_3. These parameters are summarized in Table 3.1.

Fig. 3.4 reveals how this filter can achieve three different k_{12} variations with frequency: constant fractional-bandwidth, decreasing fractional-bandwidth, and increasing fractional-bandwidth. All of these designs have the same values of k_{12} at $f \simeq$850 MHz, and at this frequency, all three filters have exactly the same characteristics. As can be seen in Table 3.1 and Fig. 3.4, the slope of k_{12} can be controlled by changing the electric coupling section, and an increase in the electric coupling results in a decrease in the slope of k_{12}. The level of

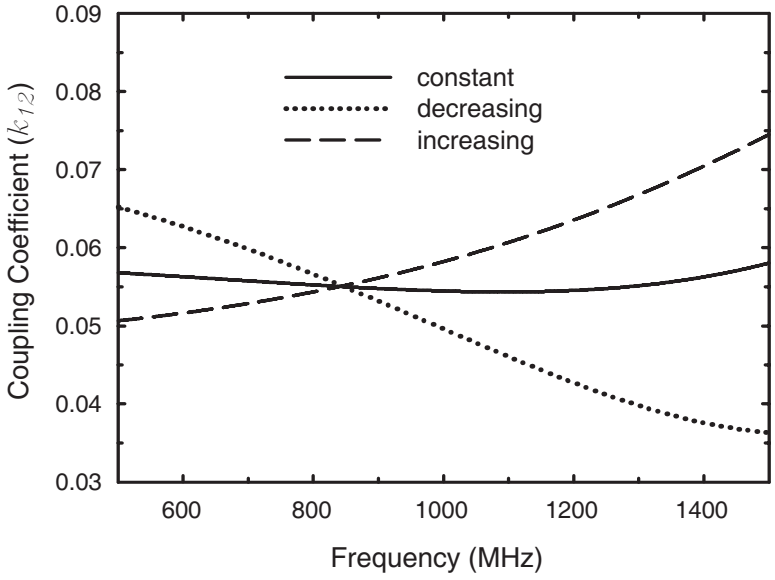

Figure 3.4: Three different k_{12} variations with frequency.

k_{12} can be also controlled by adjusting the magnetic coupling section length, l_3. These two mechanisms allow us to design a cross-over frequency of 850 MHz and different k_{12} slopes.

3.2.5 Implementation of the Tunable Filter

For this filter structure, it is not possible to implement the design values into an exact physical layout because of right angle bends. When realized physically, parasitic effects such as open-end fringing, right angle bend parasitics, coupled section fringing, via-hole inductance, and even coupling between non-adjacent transmission line sections all add up and deviate the filter responses from that of the ideal electrical model. A full-wave matrix method is used to include all of these effects in the filter design. A full-wave simulation of the resonator structure in Fig. 3.5 (without C_L, C_M, and Z_0) is performed using Sonnet[42]

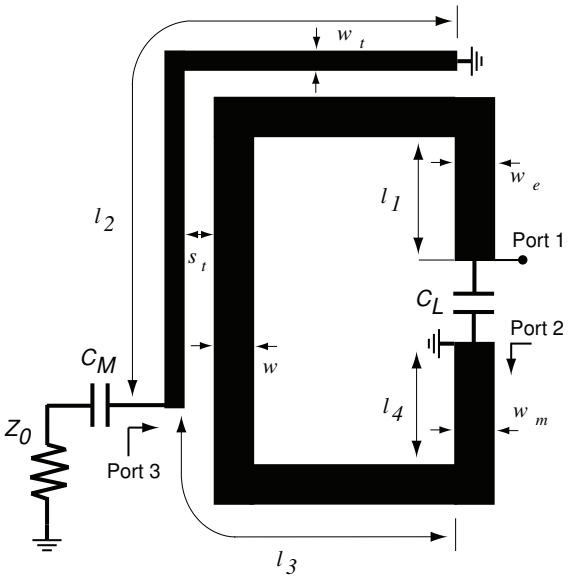

Figure 3.5: Full-wave simulation model of the tunable resonator.

and the 3-port Y-parameters are extracted. The 3-port full-wave Y-matrix is

$$Y^{3p} = \begin{bmatrix} Y_{11}^{3p} & Y_{12}^{3p} & Y_{13}^{3p} \\ Y_{21}^{3p} & Y_{22}^{3p} & Y_{23}^{3p} \\ Y_{31}^{3p} & Y_{32}^{3p} & Y_{33}^{3p} \end{bmatrix}. \tag{3.40}$$

The 1-port Y-parameter of the single resonator structure (with C_L, C_M, and Z_0) in Fig. 3.5 can be found by short-circuiting port 2 and open-circuiting port 3. The 1-port input Y-matrix, Y_{in}^{1p} is

$$Y_{in}^{1p} = Y_r^{1p} + j\omega C_L \tag{3.41}$$

where

$$Y_r^{1p} = y_{11}^{3p} - y_{13}^{3p} \frac{y_{31}^{3p}}{y_{b33}^{3p}} \tag{3.42}$$

$$y_{b33}^{3p} = y_{33}^{3p} + \frac{j\omega C_M Y_0}{j\omega C_M + Y_0}. \tag{3.43}$$

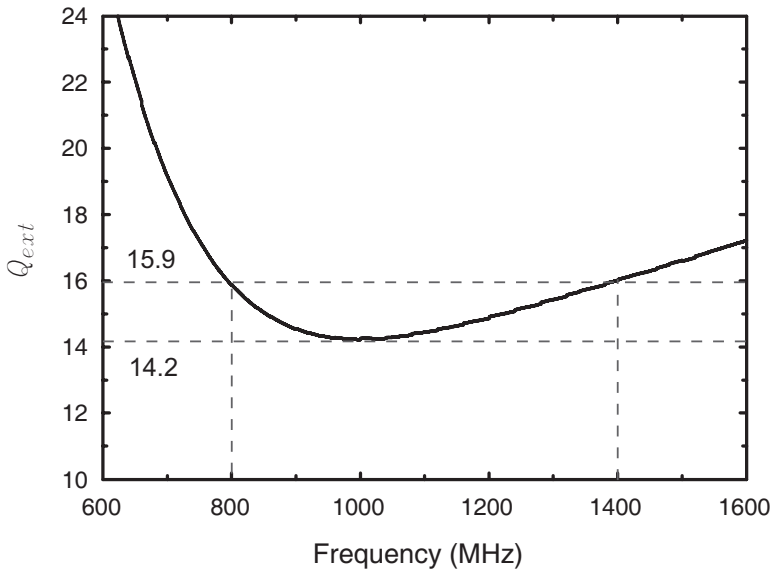

Figure 3.6: External Q (Q_{ext}) as a function of the resonance frequency for the constant fractional-bandwidth filter.

The external coupling is given by (3.36) with Y_{r11}^{L} replaced by Y_{r}^{1p}. Fig. 3.6 shows the resonator Q_{ext} values as a function of the resonance frequency for the constant fractional-bandwidth case. The Q_{ext} value is 15±1 over the frequency range of 800 to 1400 MHz.

The complete filter circuit with external coupling is shown in Fig. 3.7. Full-wave simulations are done for this structure (without C_L, C_M, and Z_0) to calculate the parasitic-included filter parameters. The simulated full-wave 6-port matrix is

$$Y^{6p} = [Y_{ij}^{6p}] \quad where \quad i,j = 1,2,...,6. \tag{3.44}$$

To calculate the filter parameters, the 6-port matrix needs to be converted to a 2-port matrix. By adding C_L, C_M, and Z_0 to the circuit, short-circuiting ports 2 and 4, and open-circuiting ports 3 and 6, matrix transformations are performed. The 2-port matrix is

$$Y^{2p} = \begin{bmatrix} j\omega C_L + Y_{r11}^{2p} & Y_{r12}^{2p} \\ \\ Y_{r12}^{2p} & j\omega C_L + Y_{r11}^{2p} \end{bmatrix} \tag{3.45}$$

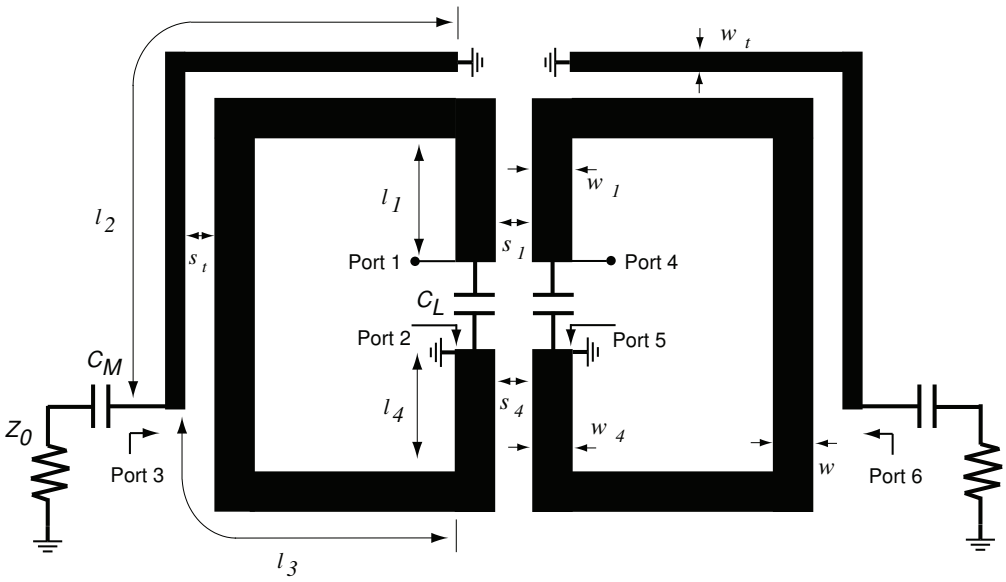

Figure 3.7: Full-wave simulation model of the tunable filter.

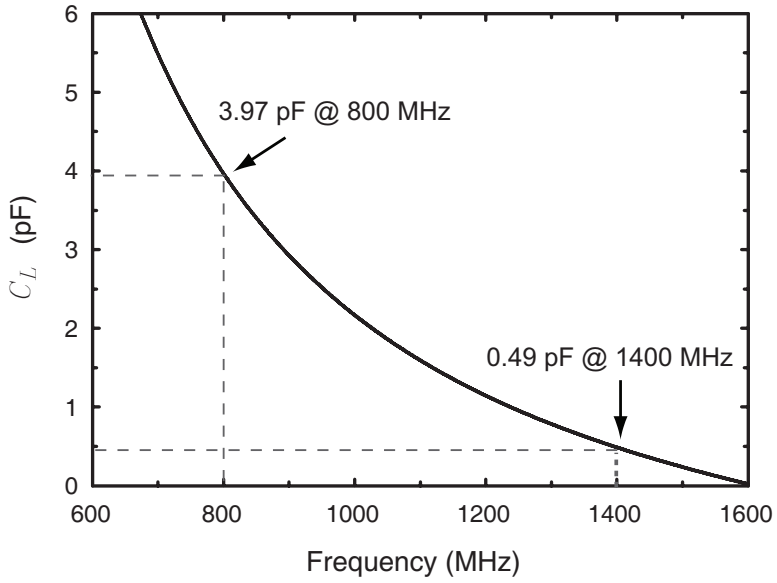

Figure 3.8: Loading capacitor, C_L, as a function of the resonance frequency for the constant fractional-bandwidth filter.

Table 3.2: Dimensions for the constant FBW, decreasing FBW, and increasing FBW Filters (Dimensions are in mm, and Capacitances are in Picofarad, $\varepsilon_r = 2.2$, 31 mil Microstrip Substrate is Assumed, FBW is fractional-bandwidth

	electric $l_1/s_1/w_1$	magnetic $1_4/s_4/w_4$	$l_2/l_3/w$	s_t/w_t	C_M
constant FBW	1.3/0.5/2.0	4.0/0.1/1.5	19.1/6.2/2.0	0.1/0.5	5.0
decreasing FBW	1.3/0.1/2.0	4.0/0.1/1.5	19.1/6.2/2.0	0.1/0.5	10.0
increasing FBW	0.3/2.1/2.0	5.0/0.1/2.0	19.1/5.7/2.0	0.1/0.5	5.0

where

$$Y_{r11}^{2p} = y_{11}^{6p} - y_{13}^{6p}\frac{(y_{b33}^{6p}y_{31}^{6p} + y_{36}^{6p}y_{34}^{6p})}{[(y_{b33}^{6p})^2 - (y_{36}^{6p})^2]} - y_{16}^{6p}\frac{(y_{b33}^{6p}y_{34}^{6p} + y_{36}^{6p}y_{31}^{6p})}{[(y_{b33}^{6p})^2 - (y_{36}^{6p})^2]} \tag{3.46}$$

$$Y_{r12}^{2p} = y_{14}^{6p} - y_{13}^{6p}\frac{(y_{b33}^{6p}y_{34}^{6p} + y_{36}^{6p}y_{31}^{6p})}{[(y_{b33}^{6p})^2 - (y_{36}^{6p})^2]} - y_{16}^{6p}\frac{(y_{b33}^{6p}y_{31}^{6p} + y_{36}^{6p}y_{34}^{6p})}{[(y_{b33}^{6p})^2 - (y_{36}^{6p})^2]} \tag{3.47}$$

$$y_{b33}^{6p} = y_{33}^{6p} + \frac{j\omega C_M Y_0}{j\omega C_M + Y_0}. \tag{3.48}$$

Using the resonance condition, C_L is calculated as

$$C_L = -Im\left[\frac{Y_{r11}^{2p}(\omega_0)}{\omega_0}\right]. \tag{3.49}$$

The variation of C_L with the resonance frequency is plotted in Fig. 3.8 for the constant fractional-bandwidth filter. This filter resonates at 1400 MHz with C_L of 0.49 pF and can be tuned down to 800 MHz by increasing C_L to 3.97 pF. The coupling coefficient, k_{12}, is calculated using (4.10) and is

$$k_{12} = \frac{Im[Y_{r12}^{2p}(\omega_0)]}{Im\left[\frac{\omega_0}{2}\frac{\partial Y_{r11}^{2p}(\omega_0)}{\partial\omega} - \frac{Y_{r11}^{2p}(\omega_0)}{2}\right]}. \tag{3.50}$$

The calculated k_{12} is 0.061±0.002 over the 800 MHz to 1400 MHz frequency range. The dimensions of the constant fractional-bandwidth filter are given in Table 3.2.

For the decreasing fractional-bandwidth and increasing fractional-bandwidth filters, the

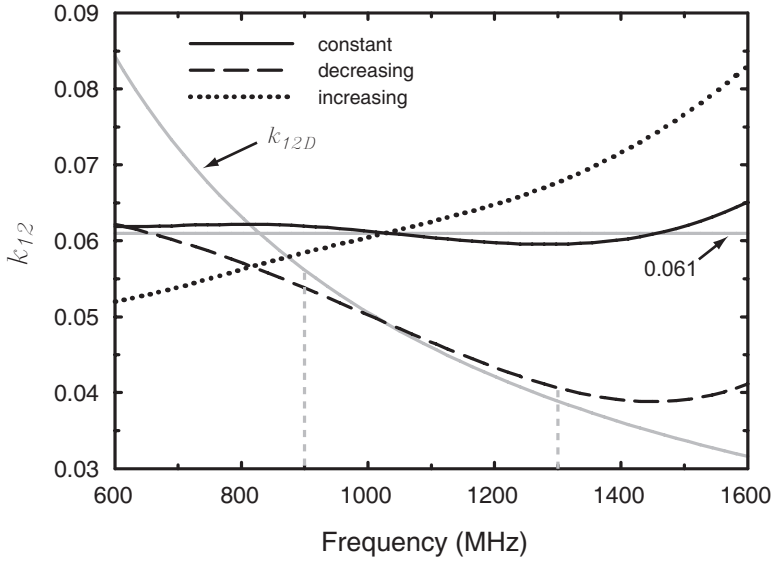

Figure 3.9: Realized k_{12} obtained using full-wave simulations and the Y-matrix method for the 3 different tunable filters.

external coupling and loading capacitance values are calculated using the same method as the constant fractional-bandwidth filter. To increase the electrical coupling in the decreasing fractional-bandwidth filter, the spacing between the coupled lines in the electric coupling section is reduced from 0.5 mm to 0.1 mm. The spacing of 0.1 mm is the minimum achievable in the copper etching process. The increasing fractional-bandwidth filter design is realized by decreasing the electric coupling. The electric coupling line spacing is increased and the line length is reduced to 2.1 mm and 0.3 mm, respectively. In the decreasing fractional-bandwidth filter, the coupled-line spacing change has an insignificant effect on the electrical length of the resonator. However, the change in both the coupled-line length and spacing in the increasing fractional-bandwidth filter has a significant effect on the electrical length of the resonator and changes the values of C_L from the values used in the constant fractional-bandwidth filter. The magnetic coupling section length of the increasing fractional-bandwidth filter is therefore increased by 1 mm to compensate for this electrical length change. The increase in magnetic coupling length also increases the overall coupling of the increasing fractional-bandwidth filter. To reduce this overall coupling increase, the coupling line width in the magnetic coupling section is increased from 1.5 mm to 2.0 mm.

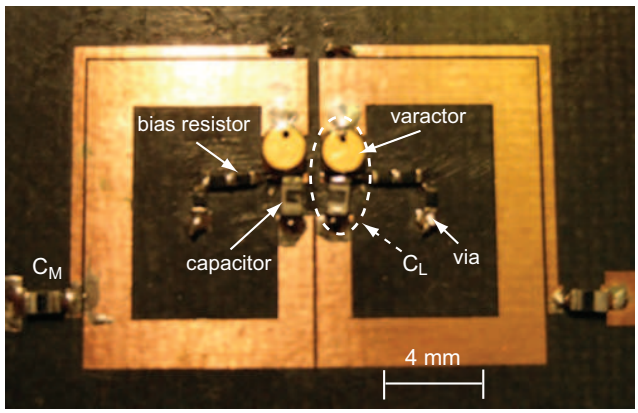

Figure 3.10: Photograph of the C_L, C_M, and bias resistors.

The coupling coefficient variations for the three filters are plotted in Fig. 3.9 and the corresponding filter dimensions are given in Table 3.2. To realize a 45 MHz 1-dB constant absolute-bandwidth, k_{12} of the decreasing fractional-bandwidth filter is adjusted to approximate the ideal coupling coefficient for a 45 MHz 1-dB bandwidth (k_{12D}). The coupling coefficient of the decreasing fractional-bandwidth filter is 0.057 at 800 MHz and decreases to 0.039 at 1400 MHz. The decreasing fractional-bandwidth filter shows a constant absolute-bandwidth behavior over the 900 MHz to 1300 MHz frequency range. k_{12} of the increasing fractional-bandwidth filter is 0.056 at 800 MHz increases to 0.071 at 1400 MHz.

3.3 Fabrication and Measurements

Three filters were fabricated on an ε_r=2.2, 0.787 mm Duroid substrate using a standard copper etching process [35]. The intrinsic Q of the microstrip resonator with w=2 mm is 210 at 1100 MHz. A detailed photograph of the filter with the biasing scheme is shown in Fig. 3.10. C_L was realized by connecting a schottky varactor diode (M\A COM MA46H202), with a specified capacitance of 3.0 $\pm$ 0.3 pF at 4 V, and a capacitance ratio of 5.6 from 2 V to 20 V bias [43], together with an AVX chip capacitor ([44]) to realize a DC biasing scheme between the short and open ends of the resonator (Fig. 3.11). The capacitor-varactor series connection reduces the overall capacitance ratio due to the fixed value of the chip capacitor.

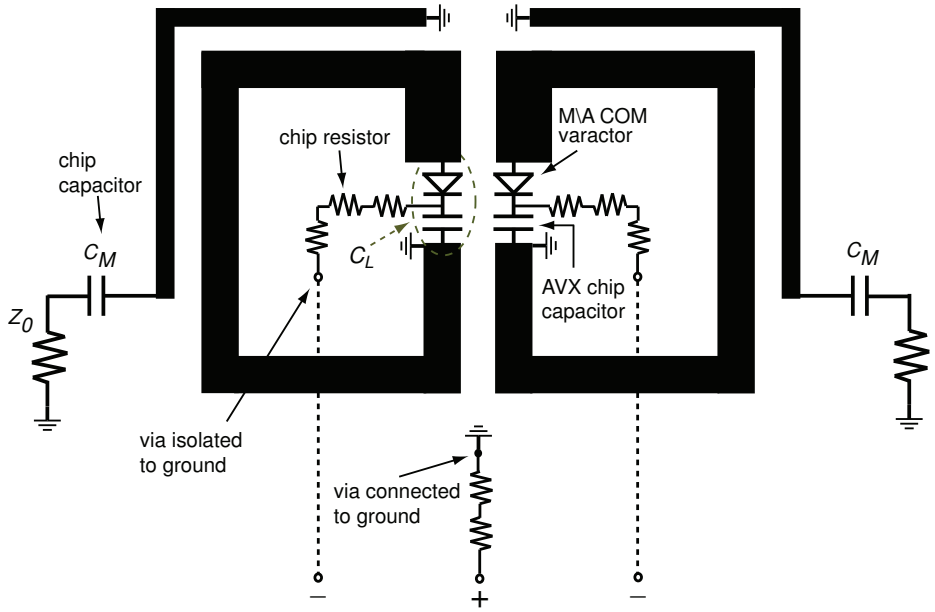

Figure 3.11: Tunable filter implementation with varactors, chip capacitors, and bias resistors.

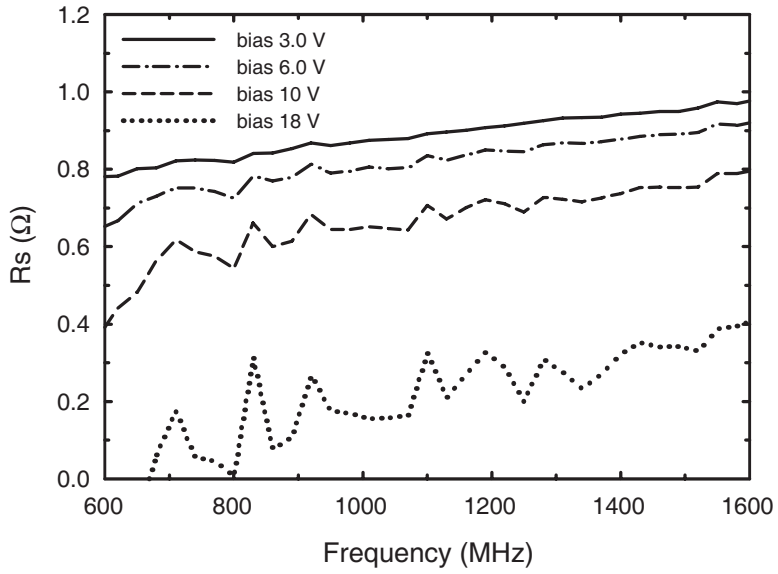

Figure 3.12: Measured series resistance (R_s) of the M\A COM varactor (MA46H202).

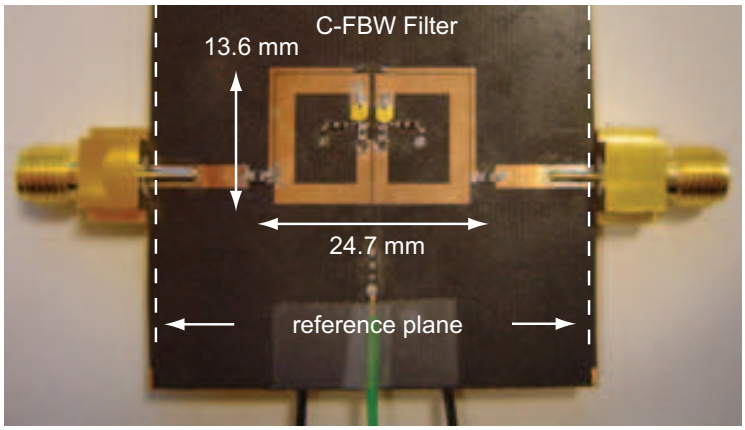

Figure 3.13: Fabricated constant fractional-bandwidth filter.

Therefore, a fixed capacitance value of 15.4 pF was chosen as a compromise between the tunability and loss of C_L. To minimize any RF signal leaking on the bias pads, the bias circuit was realized using three 5 $k\Omega$ resistors instead of one 15 $k\Omega$ resistor.

The series resistance (R_s) of the varactor was measured using an Agilent E4491A Impedance Analyzer to precisely simulate the filter loss. The varactor series resistance decreases with increasing bias voltage, and is between 0.2-0.9 Ω at 18-3 V bias, respectively (Fig. 3.12).

The S-parameters of the three filters were measured with an Agilent E5071B PNA. The SOLT calibration was performed using an Agilent E-cal kit. The filter S-parameters were measured with bias voltages ranging from 22.0 V (varactor break-down voltage) to 2-3 V. However, the filter response is plotted for the bias voltages which result in a 3-dB S_{21} cross-over at adjacent frequency states.

3.3.1 Constant Fractional-Bandwidth Filter

The fabricated constant fractional-bandwidth filter is shown in Fig. 3.13 with an overall size of 24.7 x 13.6 mm^2 and its measured frequency response is shown in Fig. 3.14. The center frequency starts at 803 MHz at 2.4 V bias, with an insertion loss of 2.88 dB and a 1-dB bandwidth of 5.7%. At 22.0 V bias, the center frequency is 1355 MHz and the insertion loss and 1-dB bandwidth are 1.04 dB and 5.1%, respectively. The measured results are

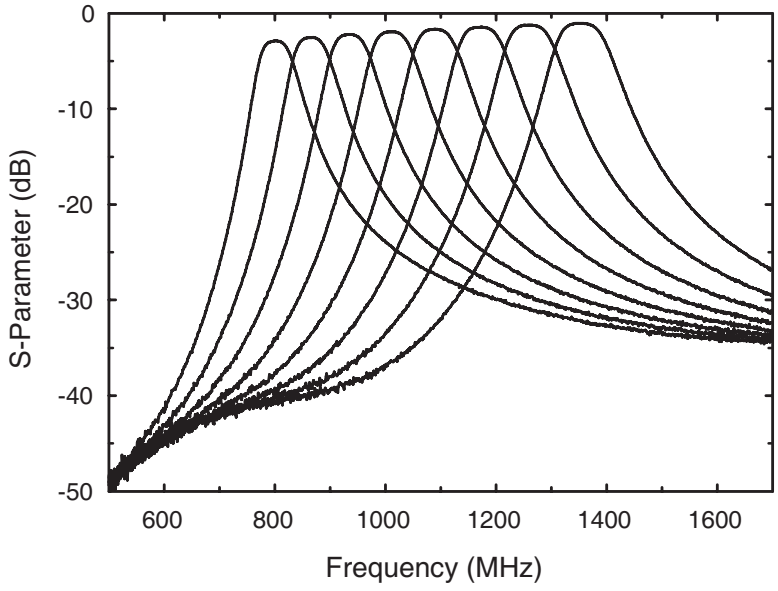

(a)

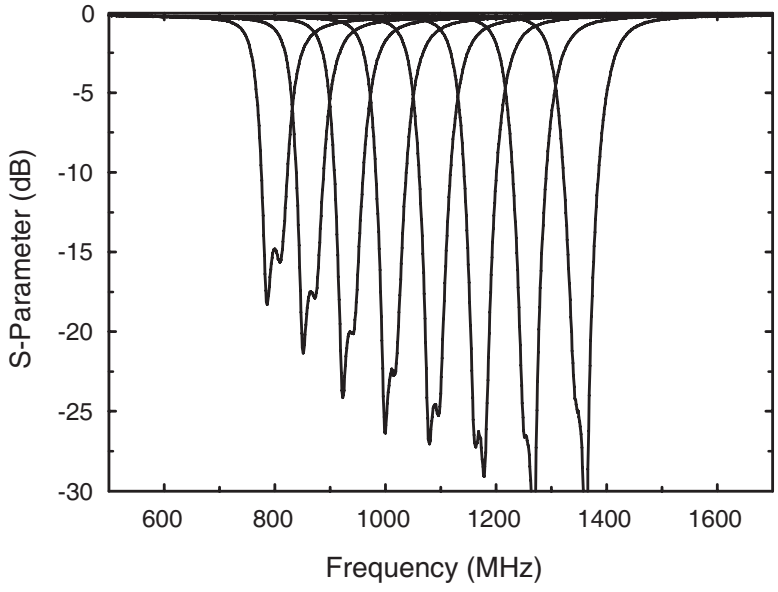

(b)

Figure 3.14: Measured S-parameters of the constant fractional-bandwidth filter, (a) S_{21} (b), S_{11}. The bias voltage is between 2.4 V and 22 V.

Table 3.3: Measured frequency, insertion loss, 1-dB bandwidth (BW), and fractional-bandwidth (FBW) of the constant fractional-bandwidth filter. (frequencies are in MHz, biases are in V, insertion losses are in dB, and BWs are in MHz, and FBWs are in %.)

Freq.	804	867	937	1013	1092	1174	1261	1357
Bias	2.4	3.2	4.2	5.5	7.2	9.6	13.6	22
I.L.	2.88	2.52	2.20	1.92	1.66	1.43	1.22	1.04
BW	46	49	52	56	58	62	65	69
FBW	5.7	5.6	5.6	5.5	5.3	5.3	5.1	5.1

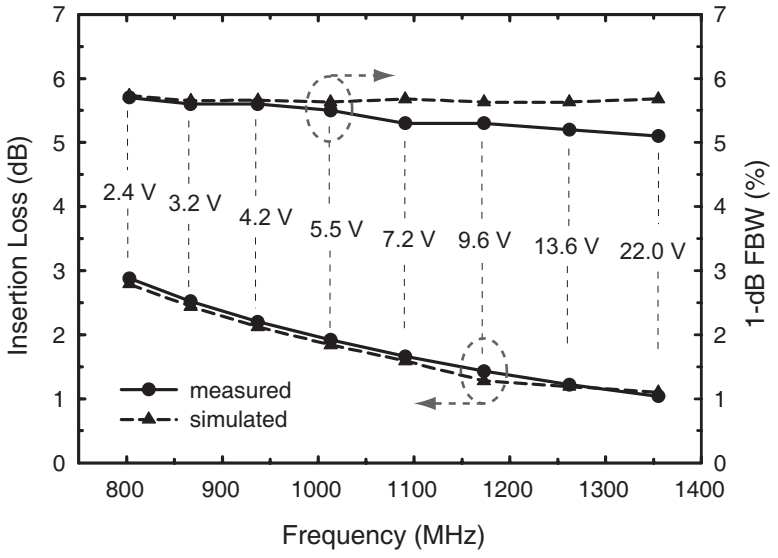

Figure 3.15: Measured and simulated insertion loss and 1-dB bandwidth of the constant fractional-bandwidth filter

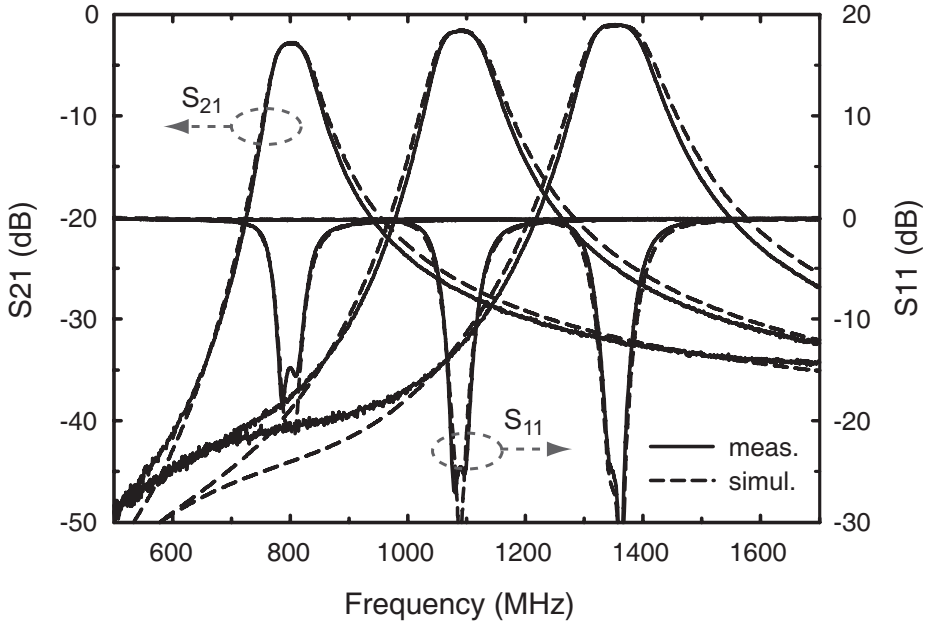

Figure 3.16: Measured and simulated S-parameters of the constant fractional-bandwidth filter (V_b=2.4 V, 7.2 V, and 22 V).

summarized in Table 3.3. The measurement shows almost constant fractional-bandwidth with a slight decrease (0.6% max) at the higher frequency states (Fig. 3.15). This is due to the increase in the filter Q and a slight change in the k_{12} slope due to the copper etching tolerance (s_1=0.5 mm, s_4=0.1 mm). The increased filter Q is due to the decrease in the varactor R_s with increased reverse bias voltage. The measured S_{11} responses of this filter show good matching over the entire tuning range. Although the change is small, the measured S_{11} of this filter becomes closer to the critically coupled states as the filter tunes to higher frequency states. This can be explained by the almost constant Q_{ext} values (15±1, Fig. 3.6) and the small decrease in the filter fractional bandwidth.

The measured and simulated filter responses are given in Fig. 3.16. The simulated filter Q is 50 at 803 MHz (V_b=2.4 V). It increases as the bias voltage increases and reaches 135 at 1355 MHz (V_b=22.0 V). The measured Q of this filter is around 53 at 803 MHz and 152 at 1355 MHz. The measurement and simulation are in excellent agreement. The harmonic responses are suppressed by more than 10 dB for all tuning states (Fig. 3.17).

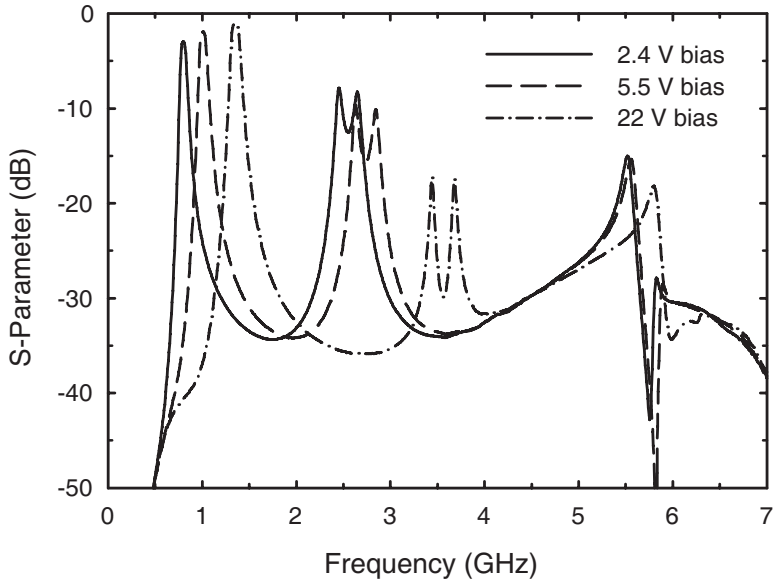

Figure 3.17: Measured harmonic responses of the constant fractional-bandwidth filter.

3.3.2 Constant Absolute-Bandwidth Filter

The fabricated constant absolute-bandwidth (decreasing fractional-bandwidth) filter is shown in Fig. 3.18. The filter dimensions are almost the same as the constant fractional-bandwidth filter except for the electric coupling section. For the constant absolute-bandwidth filter, the gap between the coupled lines in the electric coupling section is 100 μm and this stronger electric coupling results in a decreased net coupling as the filter tunes to higher frequency states. At 3.9 V bias, the center frequency is 911 MHz and the insertion loss

Table 3.4: Measured frequency, insertion loss, 1-dB bandwidth (BW), and fractional-bandwidth (FBW) of the constant absolute-bandwidth filter. (frequencies are in MHz, biases are in V, insertion losses are in dB, and BWs are in MHz, and FBWs are in %.)

$Freq.$	911	971	1023	1095	1160	1221	1284	1335
$Bias$	3.9	4.9	5.9	7.6	9.6	12.3	13.6	16.5
$I.L.$	2.89	2.58	2.35	2.09	1.91	1.82	1.84	1.93
BW	47	47	47	46	44	42	40	38
FBW	5.2	4.9	4.6	4.2	3.8	3.4	3.1	2.9

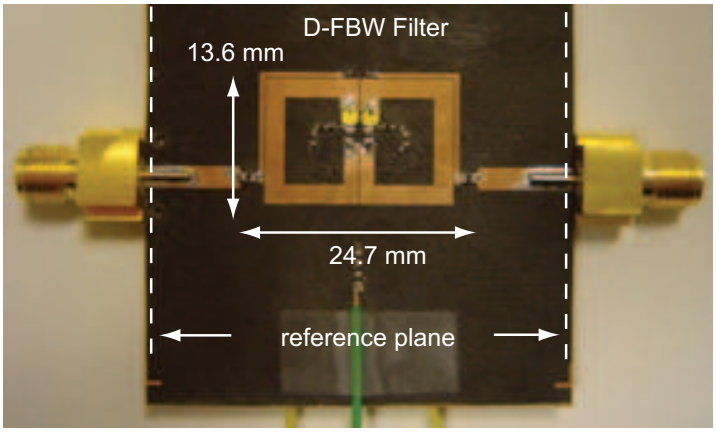

Figure 3.18: Fabricated constant absolute-bandwidth filter

and 1-dB fractional-bandwidth are 2.89 dB and 5.2% respectively. The center frequency increases to 1335 MHz at 22 V bias, and the insertion loss and 1-dB fractional bandwidth are 1.93 dB and 2.9%, respectively. The measured results are summarized in Table 3.5.

The measured S_{21} and S_{11} are plotted in Fig. 3.19(a) and Fig. 3.19(b), respectively. The measured and simulated 1-dB fractional-bandwidth and insertion loss are shown in Fig. 3.20. The measured 1-dB bandwidth is approximately 43±3 MHz (constant absolute-bandwidth) up to 1250 MHz center frequency. The measured S_{11} in Fig. 3.19(b) changes from under-coupled to over-coupled states. The almost constant Q_{ext} values and the decreasing fractional-bandwidth of this filter are responsible for these S_{11} changes.

The measured and simulated responses of this filter are plotted in Fig. 3.21, and again are in excellent agreement. The measured and simulated Q of the filter at 915 MHz (V_b=3.9 V) and 1335 MHz (V_b=22 V) are 66 and 64, and 150 and 141, respectively. The harmonic responses are also suppressed by more than 10 dB (Fig. 3.22). The filter with a constant absolute-bandwidth of 43±3 MHz and an insertion loss of 1.9-2.9 dB may be very useful for many emerging wireless systems, and is a state-of-the-art result in this frequency range.

3.3.3 Increasing Fractional-Bandwidth Filter

The fabricated increasing fractional-bandwidth filter is shown in Fig. 3.23. The electric coupling section length and gap of this filter are modified significantly (l_1=0.3 mm,

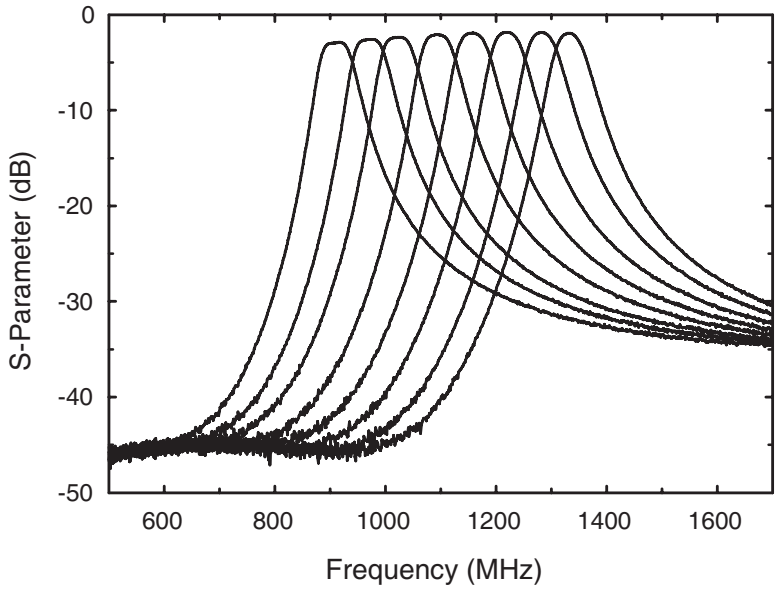

(a)

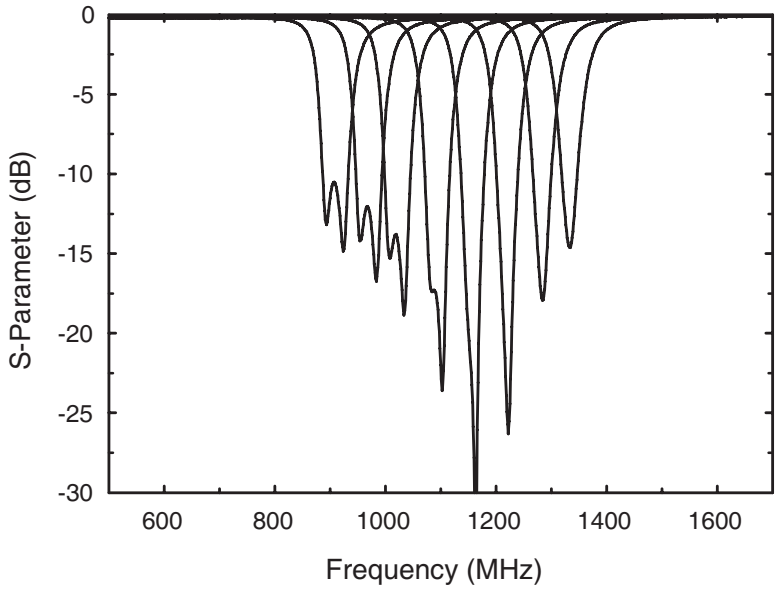

(b)

Figure 3.19: Measured S-parameters of the constant absolute-bandwidth filter, (a) S_{21} (b), S_{11}. The bias voltage is between 3.9 V and 22 V. The absolute bandwidth is 43±3MHz from 915 to 1250 MHz.

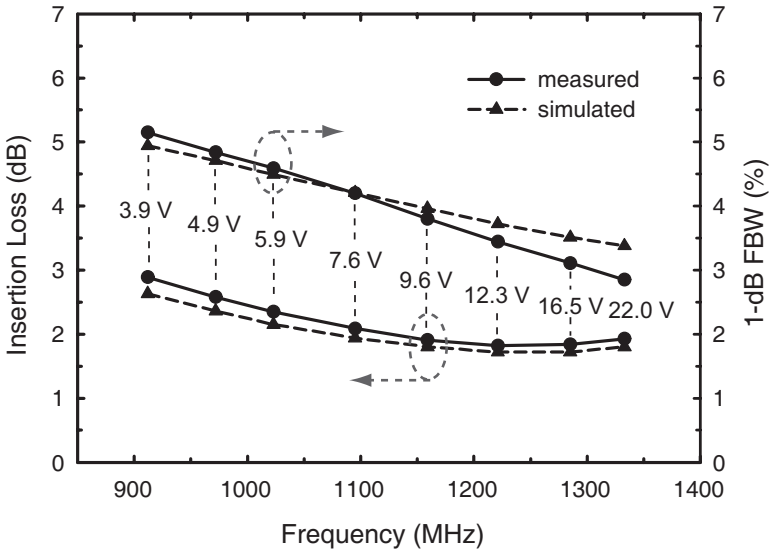

Figure 3.20: Measured and simulated insertion loss and 1-dB bandwidth of the constant absolute-bandwidth filter.

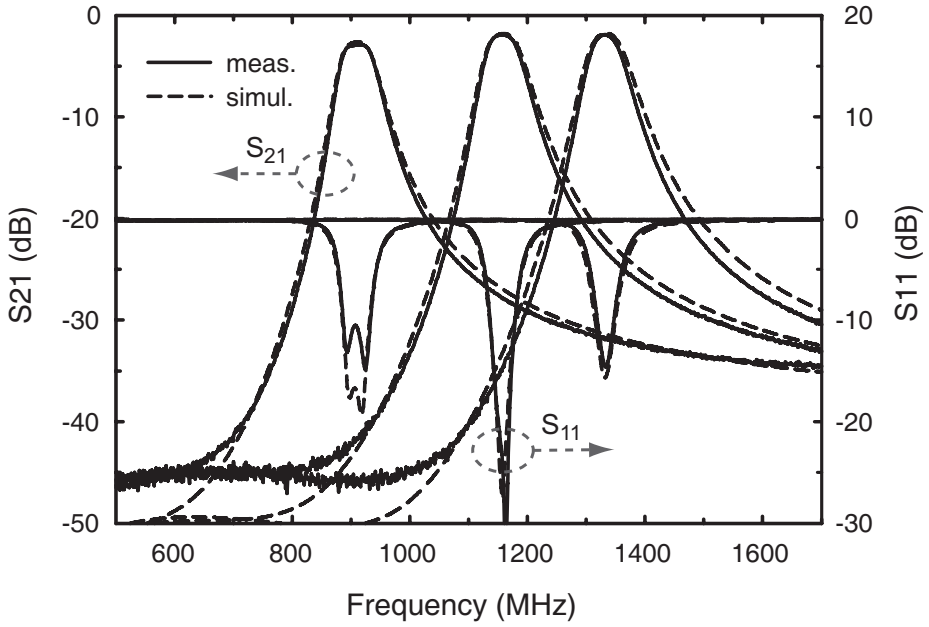

Figure 3.21: Measured and simulated S-parameters of the constant absolute-bandwidth filter (V_b=3.9 V, 9.6 V, and 22 V).

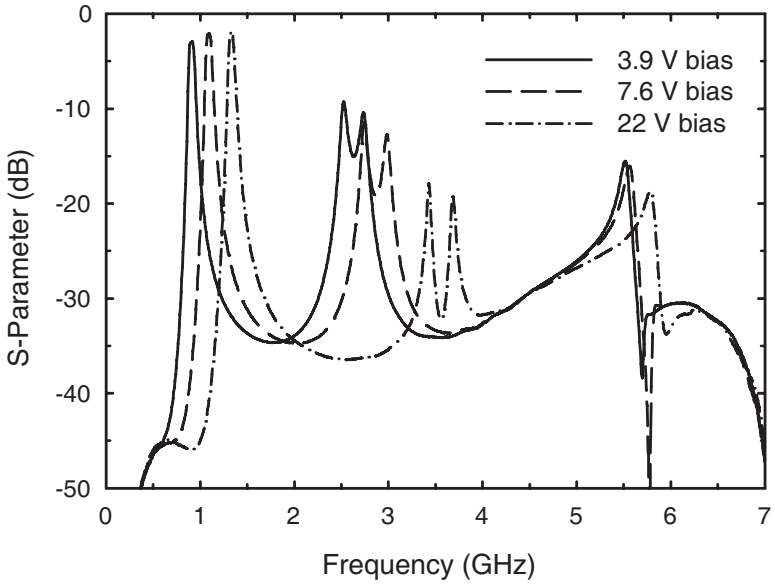

Figure 3.22: Measured harmonic responses of the constant absolute-bandwidth filter.

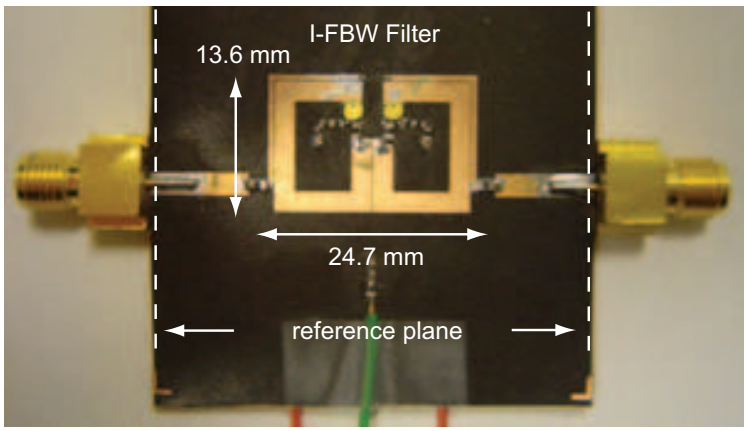

Figure 3.23: Fabricated increasing fractional-bandwidth filter.

Table 3.5: Measured frequency, insertion loss, 1-dB bandwidth (BW), and fractional bandwidth (FBW) of the increasing fractional-bandwidth filter. (Frequencies are in MHz, biases are in V, insertion losses are in dB, and BWs are in MHz, and FBWs are in %.)

$Freq.$	856	912	976	1042	1117	1203	1297	1414
$Bias$	2.8	3.5	4.4	5.5	7.0	9.2	12.2	22
$I.L.$	3.16	2.79	2.40	2.05	1.74	1.42	1.20	1.08
BW	41	44	49	54	60	69	80	96
FBW	4.3	4.4	4.6	4.7	5.0	5.4	5.9	6.5

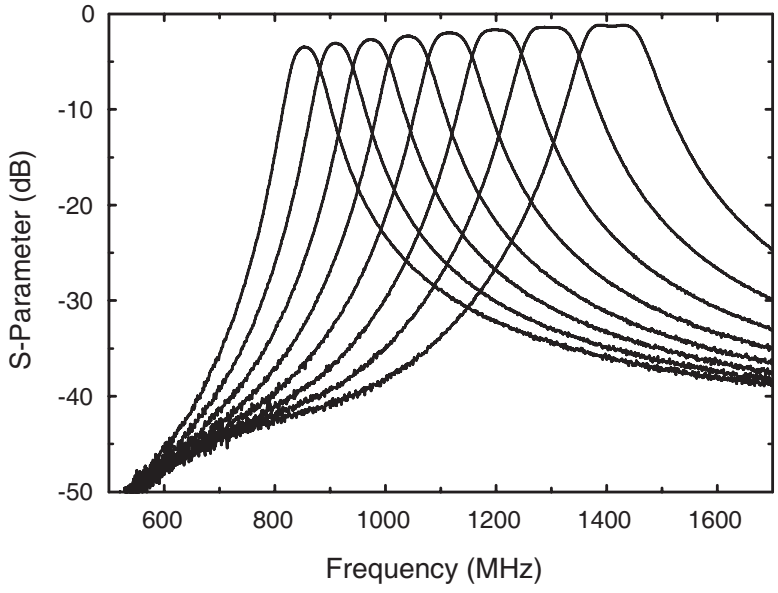

(a)

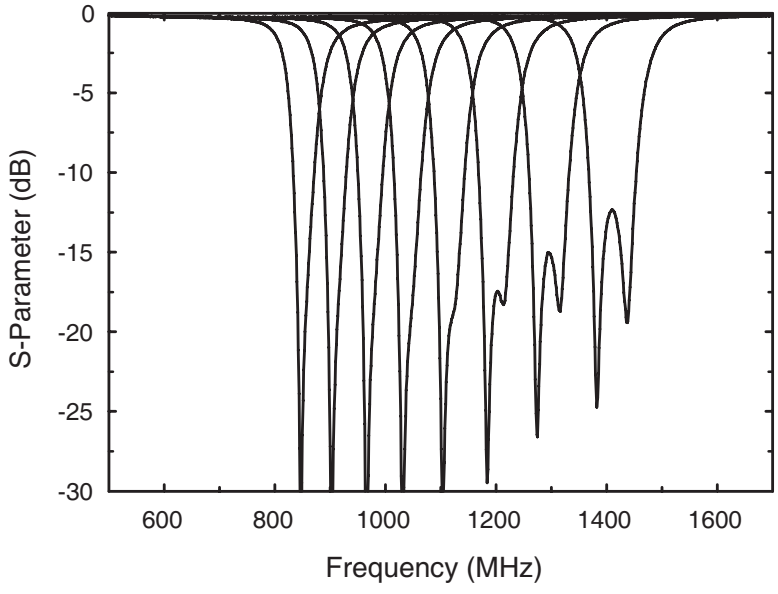

(b)

Figure 3.24: Measured S-parameters of the increasing fractional-bandwidth filter, (a) Measured S_{21} , (b) S_{11}. The bias voltage is between 2.8 V and 22 V.

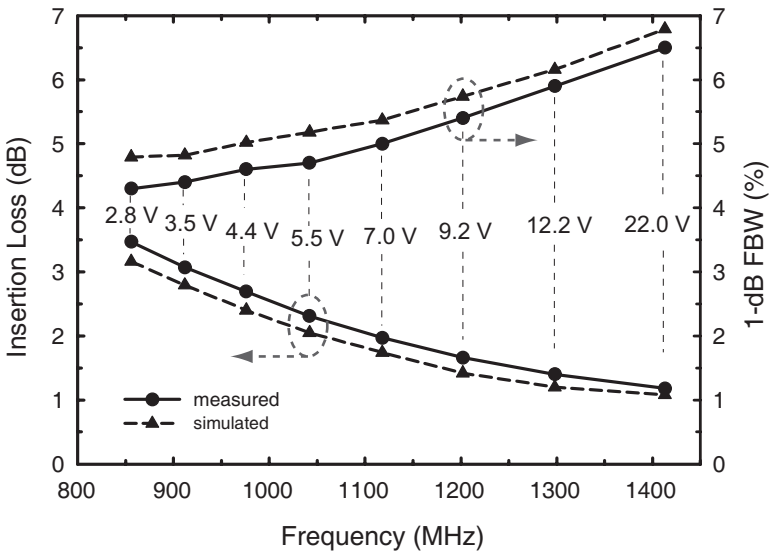

Figure 3.25: Measured and simulated insertion loss and 1-dB bandwidth of the increasing fractional-bandwidth filter.

s_1=2.1 mm) to reduce the electric coupling, which results in an increasing slope of k_{12} with frequency.

S-parameters are shown in Fig. 3.24. At 2.8 V bias, the center frequency is 856 MHz and the insertion loss and 1-dB fractional-bandwidth are 3.47 dB and 4.3% respectively. At 22 V bias, the center frequency reaches 1413 MHz and the insertion loss and 1-dB fractional-bandwidth are 1.18 dB and 6.5% respectively. The measured results are summarized in Table 3.5

The measured insertion loss and 1-dB fractional-bandwidth are plotted in Fig. 3.25 and clearly show an increasing fractional-bandwidth behavior (S-parameters are not shown for brevity). The insertion loss changes from 3.47 dB at the lowest frequency state to 1.18 dB at the highest frequency state. This change is the largest of all three filters and is due to the increase in fractional-bandwidth as well as the increase in filter Q. The measured and simulated responses are shown in Fig. 3.26 and are in excellent agreement. The measured 1-dB fractional-bandwidths are slightly smaller than the simulated values, and this is due to the parasitic fringing field caused by the lumped components and the copper etching tolerance. The effect of the lumped component fringing is not negligible when the coupling is small. The simulated and measured Q are both 52 at the lowest frequency state, and the

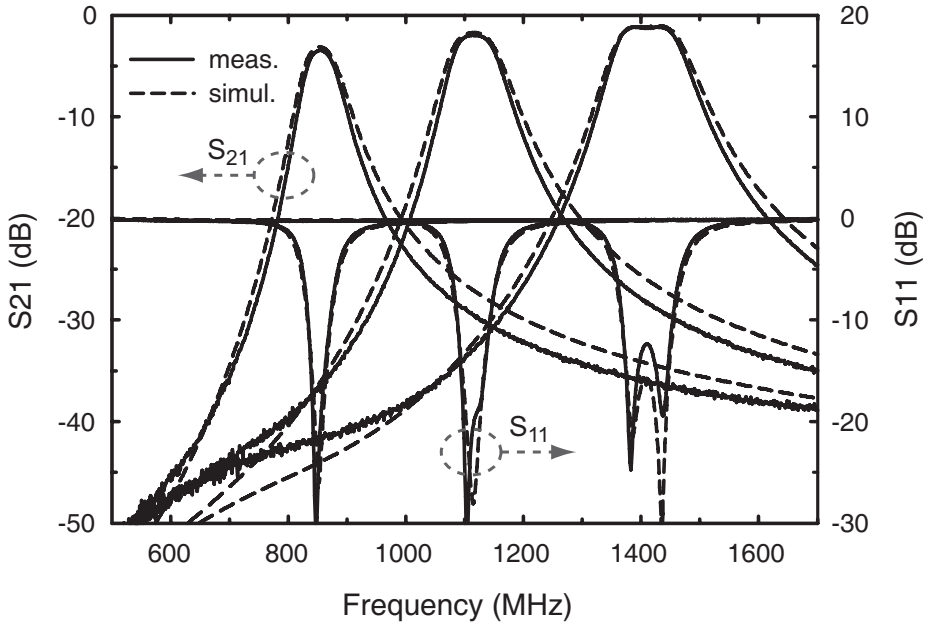

Figure 3.26: Measured and simulated S-parameters of the increasing fractional-bandwidth filter (V_b=2.8 V, 7.0 V, and 22 V).

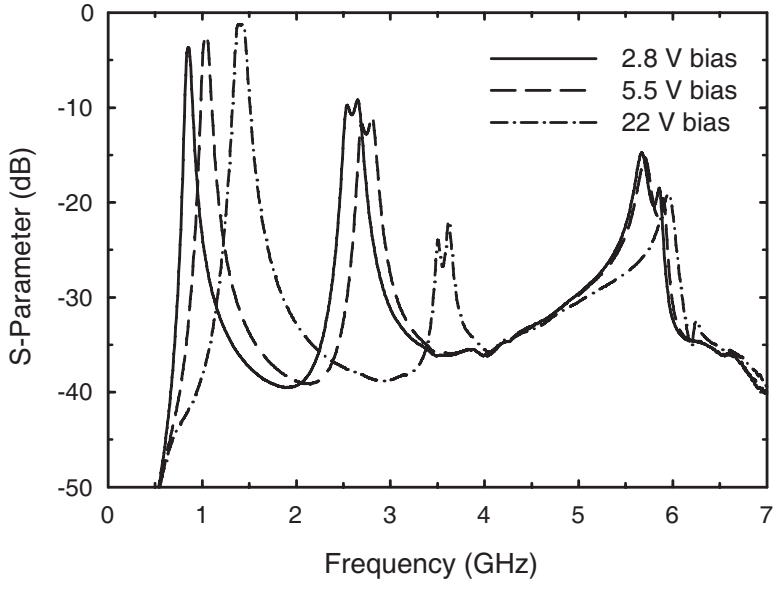

Figure 3.27: Measured harmonic responses of the increasing fractional-bandwidth filter.

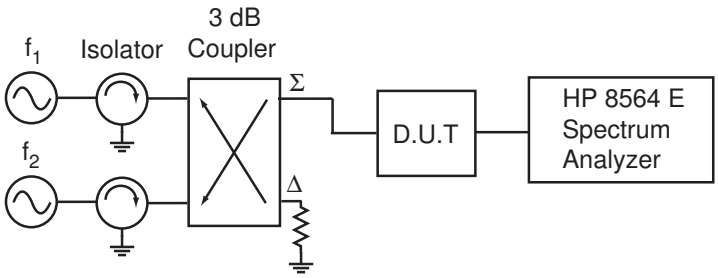

Figure 3.28: Experimental setup for intermodulation measurements.

simulated and measured Q are 132 and 143, respectively, at the highest frequency state.

The S_{11} responses of the filter in Fig. 3.24(b) show an over-coupled response at lower frequency states and under-coupled response at higher frequency states. This change with increasing frequency is opposite to that of the constant absolute-bandwidth filter and can be understood by the filter fractional-bandwidth change with almost constant Q_{ext} values. As shown in Fig. 3.27, the harmonic responses are again lower by more than 10 dB for all tuning states.

3.3.4 Nonlinear Characterization of the Tunable Filters

The nonlinear behavior of these filters is due to the schottky-diode varactors and the large voltage swings across the them. For example, for an input power of 10 dBm at 1095 MHz in the constant absolute-bandwidth filter, the RF peak to peak voltage across each diode is 3.4 V (the varactor is biased at 7.6 V with C_{tot}=1.6 pF). This results in a dynamic capacitance variation of 2.1-1.2 pF and therefore, substantial IM3 products when two signals are present. The nonlinear characterization is performed using the experimental setup shown in Fig. 3.28.

Fig. 3.29 shows the measured and simulated IIP3 of the three filters for different bias voltages. As the bias voltage increases and the frequency shifts upward, the operating point of the varactor moves toward the linear C-V curve region and the IIP3 products become higher. The simulation and measurement are in good agreement at 800 MHz-1200 MHz (V_b<20). For V_b=22 V and f_0=1350-1400 MHz, the simulated IIP3 values are larger by about 5.5 dB than the measured IIP3 values. This is due to the constant gamma varactor

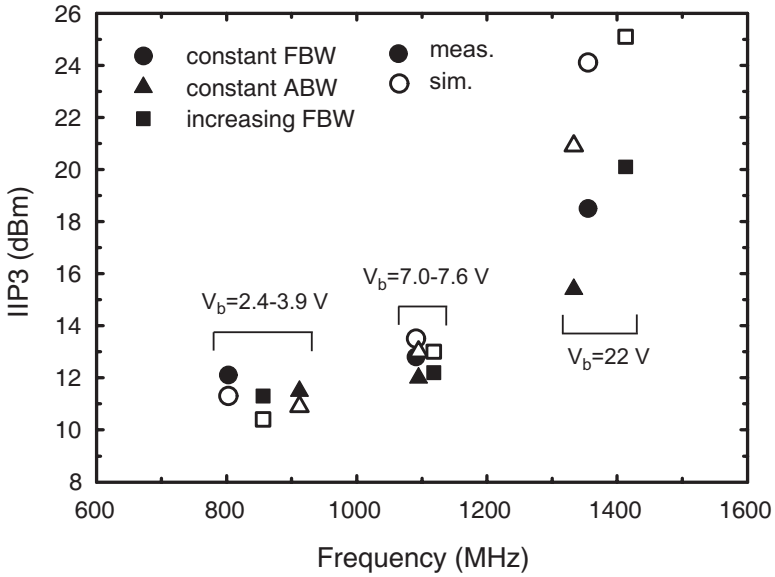

Figure 3.29: Measured IIP3 of the three tunable filters. FBW is fractional-bandwidth and ABS is absolute-bandwidth.

model in the simulation. The real diode has a constant gamma only at 2-20 V and exhibits more nonlinearity than the simulation model at 22 V bias.

The measured IIP3 of the constant absolute-bandwidth, constant fractional-bandwidth, and increasing fractional-bandwidth filters at 22 V bias are 15.4 dBm (2.9 % fractional-bandwidth), 18.5 dBm (5.1 % fractional-bandwidth), and 20.1 dBm (6.5 % fractional-bandwidth) respectively. These different IIP3 values at the same bias voltage are due to the different fractional-bandwidth of the three filters. A narrower fractional-bandwidth results in a higher Q_{ext}, and therefore, a larger voltage swing across the diodes. IIP2 measurements with Δf=1 MHz were limited by the spectrum analyzer and are virtually infinite due to the series connection of finite capacitance and the transformer coupling at the input and output ports.

The 1-dB compression points of the filters were simulated and measured to examine the power handling capacity (Table 3.6), and good agreement between measurement and simulation is obtained. Again, the filter with the narrower fractional-bandwidth results in the lower power handling. It is clear that schottky-diode based filters can handle 6-10 dBm of power at low bias voltages.

The S-parameter responses of the three filters with different input power levels are

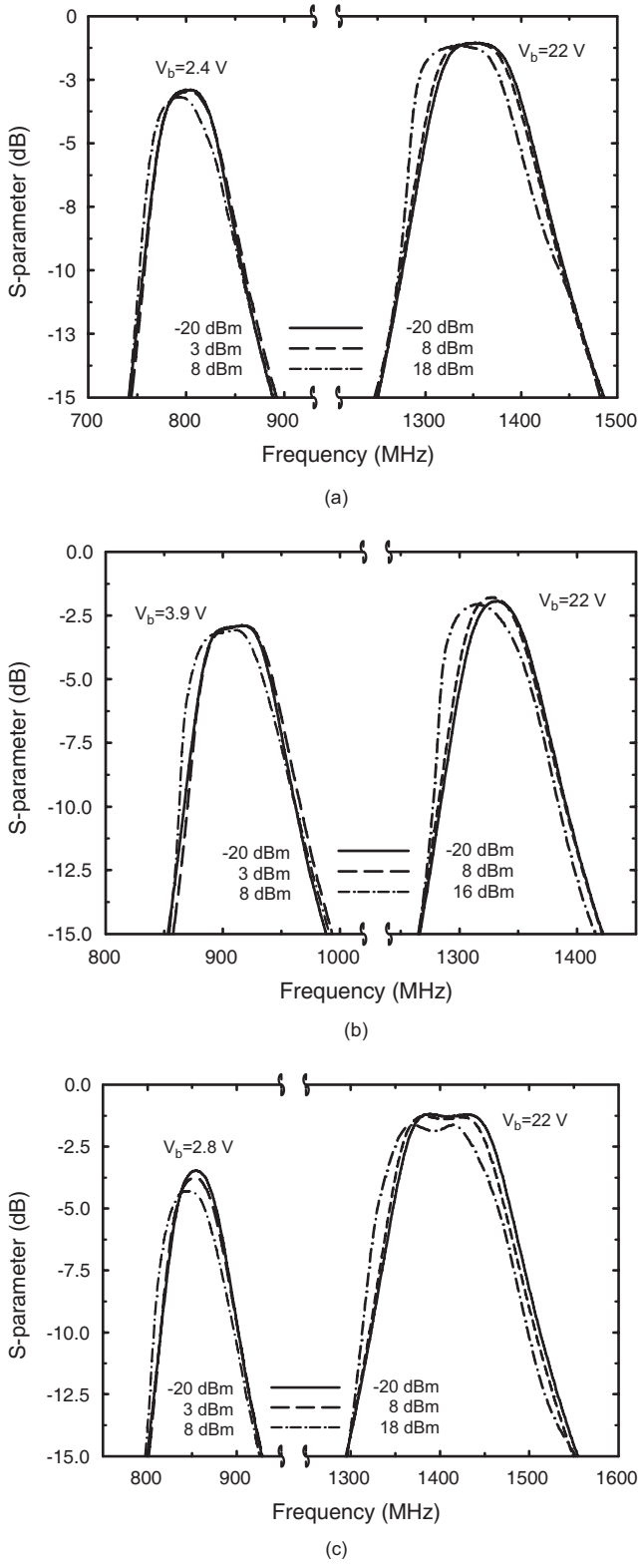

Figure 3.30: Measured S_{21} distortion of (a) the constant FBW filter, (b) the decreasing FBW filter, (c) and the increasing FBW filter with different input powers (FBW is fractional-bandwidth).

Table 3.6: Measured 1-dB compression points of the three filters. (frequencies are in MHz, biases are in V, and powers are in dBm, FBW is fractional-bandwidth and ABW is absolute-bandwidth)

	constant FBW		constant ABW		increasing FBW	
freq.	803	1355	912	1333	856	1413
Bias	2.4	22	3.9	22	2.8	22
P_{1dB} (meas.)	9.1	18.6	10.3	17.6	6.5	19.6
P_{1dB} (sim.)	8.3	20.7	9.0	18.6	8.7	21.4

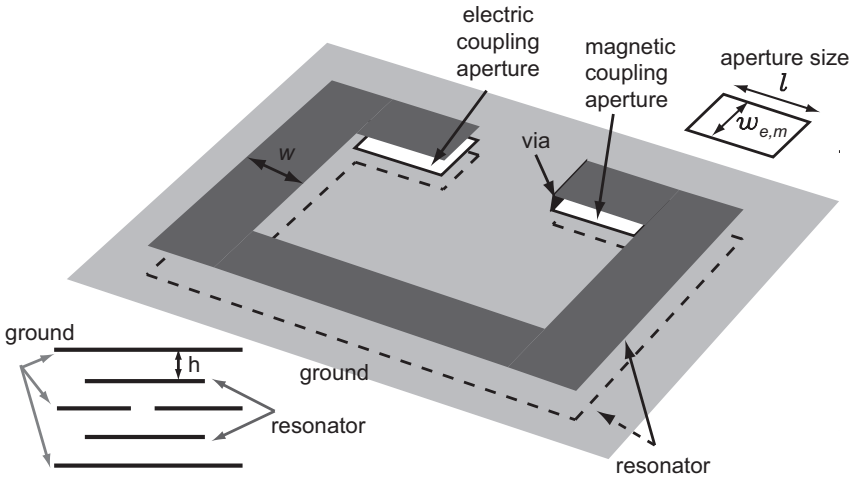

Figure 3.31: The realization of independent electric and magnetic coupling through the aperture coupling.

plotted in Fig. 3.30. Again, a power handling of 6-10 dBm is noticed before distortion occurs in the frequency response.

3.4 Multi-resonator implementation

The topology proposed in this paper has difficulty in realizing a large order (n≥3) filter with a planar implementation. A possible solution is to stack the resonators vertically with ground plane separations and couple them using electric and magnetic apertures (Fig. 3.31). A 4-pole filter will therefore consist of 4 resonators and 5 layers of ground planes (3 layers

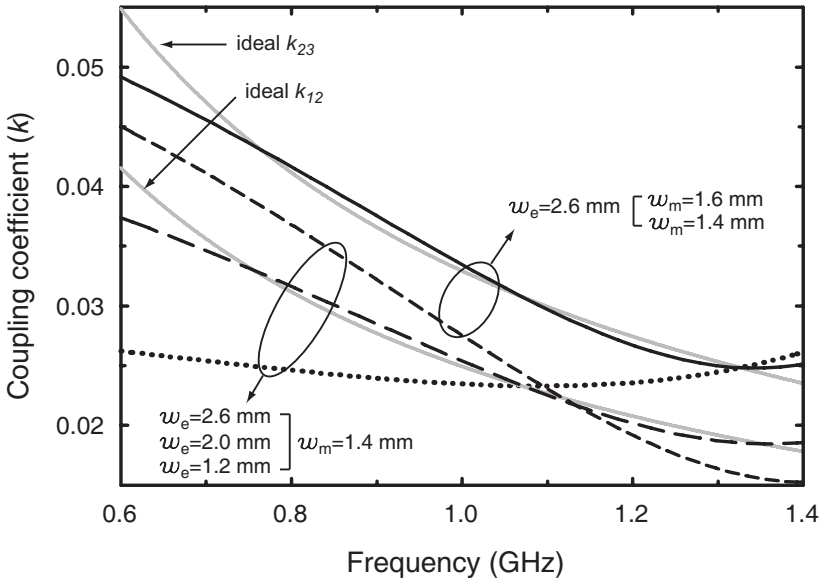

Figure 3.32: The coupling coefficient slope changes with different aperture sizes (l=2.8 mm for all cases).

for the ground with the coupling apertures and 2 layers for the top and bottom ground).

The coupling coefficients for two resonators of width w=1.2 mm (ϵ_r=2.2, h=0.508 mm) are plotted in Fig. 3.32. w_e and w_m are the width of the electric and magnetic coupling slots, respectively, and l is the length of the slot. The coupling coefficient slope is controlled by adjusting the electric coupling aperture, and the magnetic coupling aperture is responsible for a level change in the coupling.

The ideal coupling coefficients (k_{12} ideal, k_{23} ideal) for a constant absolute-bandwidth filter (0.05 dB ripple, 37 MHz bandwidth) are also shown in Fig. 3.32. The realized coupling coefficients (w_e=2.0, w_m=1.4 and w_e=2.6, w_m=1.6) are all very close ($\pm$0.01) to the ideal constant absolute-bandwidth ones in 700-1400 MHz frequency range. This shows that this topology can result in an octave-band tunable 4-pole constant absolute-bandwidth filter. As is shown in Fig. 3.32, almost any coupling coefficient variation can be realized by simply changing its slope and shifting its value on the y-axis.

3.5 Conclusion

Three filters with different predefined fractional-bandwidth variations were designed, fabricated, and measured. The three different coupling coefficient variations of these filters are accomplished mainly by controlling the amount of the electric coupling between the resonators and are due to the unique *independent* electric and magnetic coupling scheme in this filter topology.

Simulations and measurements are in excellent agreement for all three filters. The designs can easily be scaled to cover the 1600-2600 MHz frequency range using the same substrate. Nonlinear characterizations were performed and a power handling of 6-10 dBm was observed at V_b=2-3 V. In the future, the use of RF-MEMS or back-to-back diodes will significantly enhance the power handling and linearity of the filters. It may also be possible to add a transmission zero to enhance the upper-side stop-band attenuation characteristics by creating a direct coupling path between the input and output ports.

A transmission zero can also be placed to enhance the high-side stop-band attenuation characteristics by creating a direct coupling path between the source and the load. The detailed implementation of the additional source-load coupling path and its full-wave simulation results are given in Fig. 3.33. The reactance value of the source-load coupling path varies from -j21 kΩ to -j12 kΩ over the 880-1320 MHz frequency range, and has no effect on the pass band responses. Over the 1895-2085 MHz frequency range, however, this reactance value varies from -j5.3 kΩ to -j4.0 kΩ, which resonates with the inductive reactance of the main coupling path, resulting in a transmission zero.

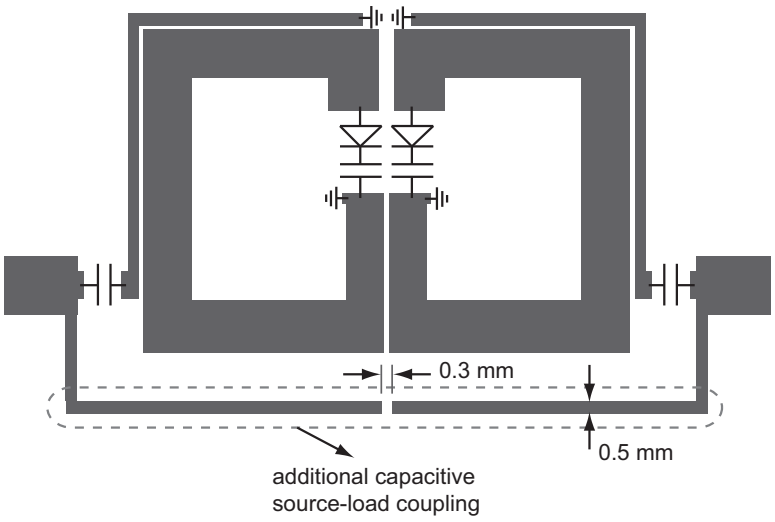

(a)

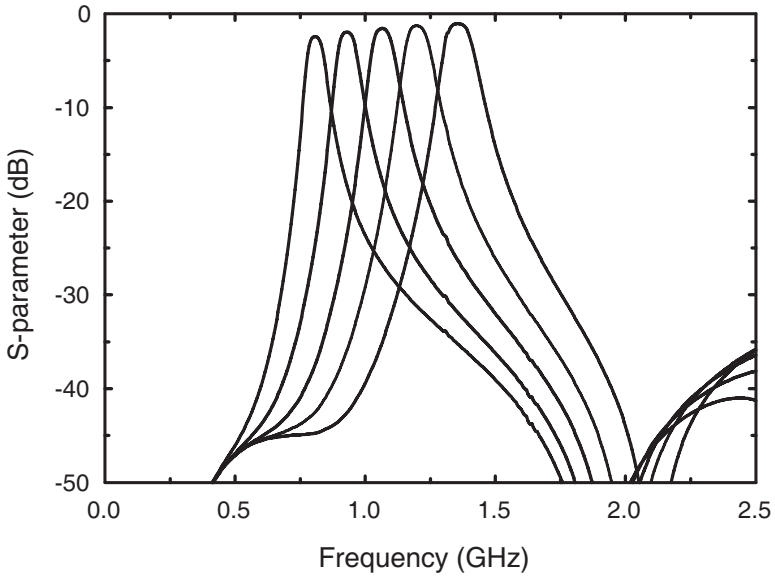

(b)

Figure 3.33: Full-wave simulation model of the tunable filter with an additional source-load coupling path (a) and its frequency responses (b). Simulated filter is identical to the constant fractional-bandwidth design of Fig. 3.13.

Chapter 4

Low Loss 5.15-5.70 GHz RF MEMS Switchable Filter for Wireless LAN Applications

4.1 introduction

Tunable filters are essential components for reconfigurable front-ends since they allow the use of a single component as opposed to a switched-filter bank, thereby reducing the system size and complexity. However, since they are placed between the antenna and the low-noise amplifier, they must exhibit very low loss and high linearity, especially in today's crowded RF environments. The tuning devices are solid-state varactor diodes or a p-i-n switch [12, 14, 15, 38], ferroelectric varactors [11, 45], or RF-MEMS devices have been shown to have very high Q at RF to mm-wave frequencies (Q > 200) and generate very low distortion levels (IM2 and IM3 components)[16]. Several notable examples of RF-MEMS tunable filters are found in [19–26]. A close examination of the RF-MEMS tunable filters in [19–25] shows overall resonator tunable Q values in the range of 40-60, which result in large insertion losses for 3-5% 2 and 3-pole filters, and therefore, it is imperative that the tunable Q be increased to > 200 if possible.

A tunable Q > 200 is not an easy feat using planar resonators. One needs to start with both a resonator Q and a tuning device Q > 200, and special attention needs to be placed on any leakage due to resistive bias lines and radiation loss which can significantly reduce the Q. Also, the filter poles need to be accurately modelled for 3-5% designs, and any deviation from the correct values can seriously degrade the input impedance in the pass-band response. Entesari et al. achieved a 5±0.5% tunable filter covering 6-10 GHz and with an excellent match (S_{11} < -16 dB), but the tunable Q was 40-50 over the 6-10 GHz range [23].

This work presents a 5% 2-pole tunable 5.15-5.70 GHz filter based on an RF MEMS switched capacitor and with a tunable resonator Q $\geq$ 150, which is about a 3$\times$ improvement over previous designs. This is achieved using microstrip-based high-Q resonators in a shielded cavity, accurate electromagnetic simulation and design, and low-loss bias lines. Also, a comprehensive design methodology for the loaded ring resonators is introduced. The frequency selection is chosen to demonstrate its use for a WLAN system, but it is evident from this work that the same filter topology can be applied anywhere in the 1-40 GHz range. The measured response agrees very well with simulations, and shows that high-Q planar tunable filters can be achieved with RF-MEMS devices.

4.2 Design

Hong et. al [46] showed how to extract the coupling and resonance frequency for the coupled open-loop structure presented in this paper using computer simulations. This method is very efficient for designing fixed frequency filters but for tunable filters, full analytic solutions need to be developed due to the introduction of tuning elements. The open-loop resonator with a loading varactor was also suggested by Makimoto et. al [47] (Fig. 4.1) but in that paper, only the analytical expression for a single capacitively-loaded resonator was given. The resonance frequency of a single *uncoupled* capacitively-loaded resonator is different from that of *coupled* capacitively-loaded resonators, and as the center frequency of the filter is varied by controlling the tuning elements, all of the filter parameters change. Therefore, to keep track of the tunable filter responses properly, analytical equations need to be developed.

4.2.1 Calculating Admittance Matrix of the Coupled Resonators

The *uncoupled* input admittance of the capacitively-loaded ring resonator (Fig. 4.1) can be found using:

$$Y_{in} = \frac{(-jY_1 \cot\phi_1 + j\omega C_L)^2 - (jY_1 \csc\phi_1 - j\omega C_L)^2}{-jY_1 \cot\phi_1 + j\omega C_L} \tag{4.1}$$

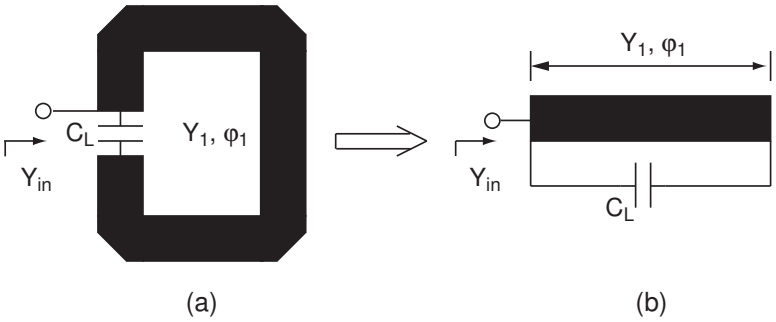

Figure 4.1: Electrical circuit model of the resonator.

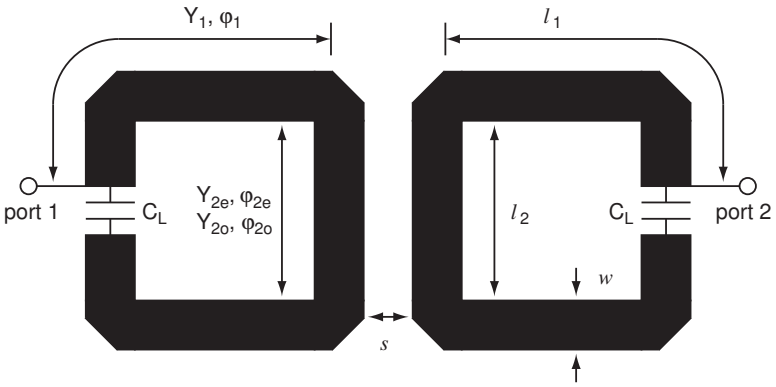

Figure 4.2: Electrical circuit model of the coupled-resonator filter with 2 ports.

The above relation is easily determined by calculating the two-port network of Fig. 4.1b and open circuiting one of the ports.

Calculating the admittance network of the coupled resonators in Fig. 4.2 requires more steps. The even-odd mode self admittances, Y_{ts_e} and Y_{ts_o} and mutual admittances, Y_{tm_e} and Y_{tm_o} of the coupled resonators are:

$$Y_{ts\_e} = \frac{A_e}{B_e} + j\omega C_L, \quad Y_{ts\_o} = \frac{A_o}{B_o} + j\omega C_L \tag{4.2}$$

$$Y_{tm\_e} = -\frac{1}{B_e} - j\omega C_L, \quad Y_{tm\_o} = -\frac{1}{B_o} - j\omega C_L \tag{4.3}$$

where

$$A_e = \cos 2\phi_1 \cos \phi_{2e} - \frac{1}{2}\left(\frac{Y_{2e}}{Y_1} + \frac{Y_1}{Y_{2e}}\right) \sin 2\phi_1 \sin \phi_{2e} \tag{4.4}$$

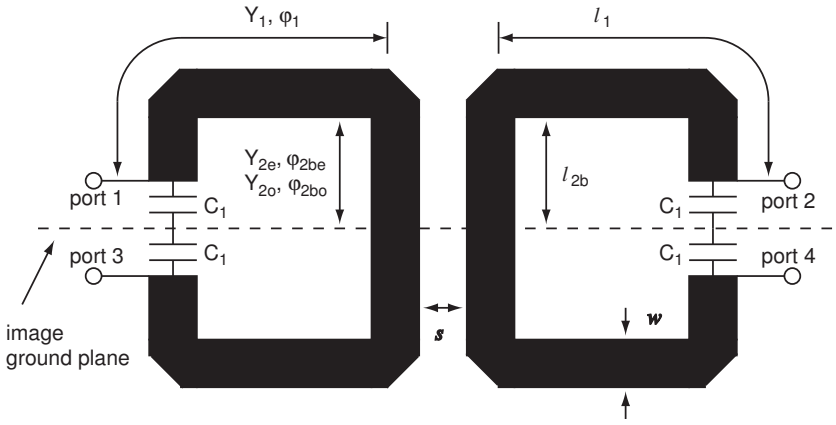

Figure 4.3: Electrical circuit model of the coupled resonator filter with 4 ports.

$$B_e = \left(\frac{j\cos^2\phi_1}{Y_{2e}} - \frac{jY_{2e}\sin^2\phi_1}{Y_1^2}\right)\sin\phi_{2e} + \frac{j\sin 2\phi_1\cos\phi_{2e}}{Y_1} \tag{4.5}$$

$$A_o = \cos 2\phi_1\cos\phi_{2o} - \frac{1}{2}\left(\frac{Y_{2o}}{Y_1} + \frac{Y_1}{Y_{2o}}\right)\sin 2\phi_1\sin\phi_{2o} \tag{4.6}$$

$$B_o = \left(\frac{j\cos^2\phi_1}{Y_{2o}} - \frac{jY_{2o}\sin^2\phi_1}{Y_1^2}\right)\sin\phi_{2o} + \frac{j\sin 2\phi_1\cos\phi_{2o}}{Y_1} \tag{4.7}$$

The even-odd mode input admittances of the coupled resonators are then:

$$Y_{in\_e} = \frac{Y_{ts\_e}^2 - Y_{tm\_e}^2}{Y_{ts\_e}}, \quad Y_{in\_o} = \frac{Y_{ts\_o}^2 - Y_{tm\_o}^2}{Y_{ts\_o}}. \tag{4.8}$$

The overall admittance matrix of the capacitively-loaded coupled resonators is then [40]:

$$Y = \begin{bmatrix} \dfrac{Y_{in\_e} + Y_{in\_o}}{2} & \dfrac{Y_{in\_e} - Y_{in\_o}}{2} \\ \\ \dfrac{Y_{in\_e} - Y_{in\_o}}{2} & \dfrac{Y_{in\_e} + Y_{in\_o}}{2} \end{bmatrix}. \tag{4.9}$$

4.2.2 Design of the Tunable Filter Using Analytical Methods

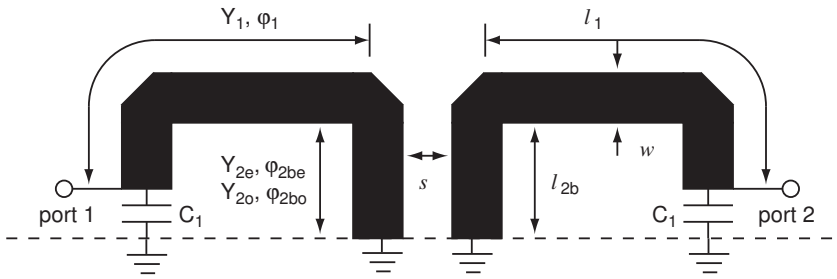

Figure 4.4: Electrical circuit model of the tunable filter with half-plane symmetry.

Calculating the loading capacitor, C_L, and even-odd mode admittances, Y_{2e} and Y_{2o}

The admittance network above (Fig. 4.2) needs to satisfy two conditions to be a filter network. The network should have the resonance frequency and the coupling coefficient of the desired filter. The two conditions are:

$$Im[Y_{11}(\omega_0)] = 0, \quad \frac{Im[Y_{12}(\omega_0)]}{b} = k_{12} \tag{4.10}$$

where

$$b = \frac{\omega_0}{2}\frac{\partial Im[Y_{11}(\omega_0)]}{\partial \omega}, \quad k_{12} = \frac{\Delta}{\sqrt{g_1 g_2}} \tag{4.11}$$

Solving (4.10) and (5.8) gives the loading capacitance, C_L, and even-odd admittances, Y_{2e} and Y_{2o}. As can be seen in the above equation, the slope parameter, b, is a function of the loading capacitance, C_L. Because Y_{2e}, Y_{2o} and C_L are coupled in (4.10) and (5.8), it is not easy to find the explicit solutions.

The difficulty in the above design equations can be bypassed if the symmetric property of the filter network is considered. As can be seen in Fig. 4.3, there is a virtual ground plane in the center plane of the filter. Because of this plane, it is possible to take into account only the upper or lower half of the filter network.

Fig. 4.4 shows the equivalent upper half of the filter network. This filter network is a capacitively-loaded $\lambda/4$ coupled structure and it is possible to decouple C_1 from the slope parameter, b. Therefore, explicit expressions for C_1, Y_{2e}, and Y_{2o} can be found as follows:

a) The even-odd mode input admittances of the filter network in Fig. 4.4 are:

$$Y_{re} = \frac{-jY_1Y_{2e}\cot\phi_{2be} + jY_1^2\tan\phi_1}{Y_1 + Y_{2e}\cot\phi_{2be}\tan\phi_1} \tag{4.12}$$

$$Y_{ro} = \frac{-jY_1Y_{2o}\cot\phi_{2bo} + jY_1^2\tan\phi_1}{Y_1 + Y_{2o}\cot\phi_{2bo}\tan\phi_1} \tag{4.13}$$

b) The overall admittance matrix of this filter network is:

$$Y_r = \begin{bmatrix} \frac{Y_{re}+Y_{r_o}}{2} + j\omega C_1 & \frac{Y_{re}-Y_{ro}}{2} \\ \\ \frac{Y_{re}-Y_{ro}}{2} & \frac{Y_{re}+Y_{ro}}{2} + j\omega C_1 \end{bmatrix} \tag{4.14}$$

c) The resonance condition, $Im[Y_{r11}(\omega_0)] = 0$, gives:

$$C_1 = -Im\left[\frac{Y_{re}(\omega_0) + Y_{ro}(\omega_0)}{2\omega_0}\right] \tag{4.15}$$

d) From the above result, b is then calculated using:

$$b = Im\left[\frac{\omega_0}{4}\frac{\partial\{Y_{re}(\omega_0) + Y_{ro}(\omega_0)\}}{\partial\omega} - \frac{Y_{re}(\omega_0) + Y_{ro}(\omega_0)}{4}\right] \tag{4.16}$$

e) Once b is determined, the even-odd admittances, Y_{2e}, Y_{2o}, are found explicitly by:

$$\frac{Im[Y_{re}(\omega_0) - Y_{ro}(\omega_0)]}{Im\left[\frac{\omega_0}{2}\frac{\partial\{Y_{re}(\omega_0)+Y_{ro}(\omega_0)\}}{\partial\omega} - \frac{Y_{re}(\omega_0)+Y_{ro}(\omega_0)}{2}\right]} = \frac{\Delta}{\sqrt{g_1g_2}} \tag{4.17}$$

which utilizes the property of the coupling coefficient:

$$k_{12} = \frac{Im[Y_{r12}(\omega_0)]}{b} = \frac{\Delta}{\sqrt{g_1g_2}}. \tag{4.18}$$

After determining the even-odd admittances, Y_{2e} and Y_{2o}, the loading capacitance, C_1,

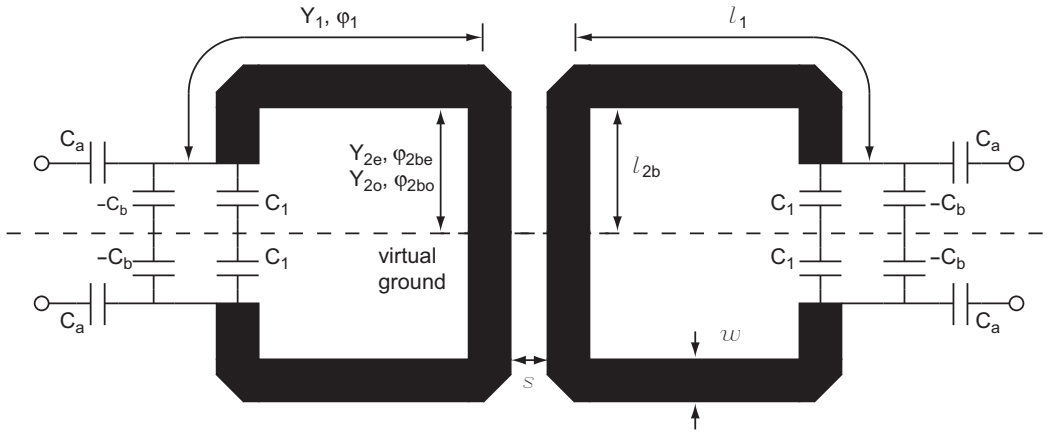

Figure 4.5: The balanced filter with the capacitive J-inverter section.

can be calculated using (4.15).

The original filter network in Fig. 4.3 has the same filter response as Fig. 4.4 due to the symmetry. Therefore, the even-odd admittances, Y_{2e} and Y_{2o}, are the same as (4.12) and (4.13) and the loading capacitor, C_L, is $C_1/2$.

Realizing external coupling, Q_{ext}

For a tunable filter, the tapping or transformer coupling methods are not appropriate when a wide tuning range is required. As is well known, the slope parameter, b, is dependent on the frequency, and any change in b results in a poor impedance match. Capacitive coupling is a good candidate for realizing wide frequency tuning because by changing the capacitance values, the slope parameter variation can be compensated completely. A frequency scaling network (*J-inverter*) consisting of a series positive capacitance with a shunt negative capacitance is the most popular solution [48].

For the *balanced*-type filter in Fig. 4.5, it is easy to realize the external coupling capacitance network because the negative capacitance value, -C_b, of the *J-inverter* section can be absorbed by the loading capacitance, C_1, by virtue of the image ground plane presented in the symmetry plane. The modified loading capacitor, C_{Lb}, and input capacitor, C_a, are

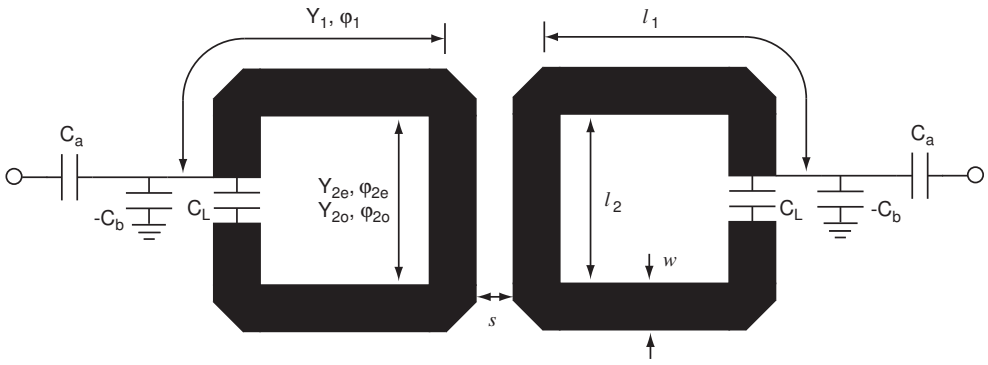

Figure 4.6: The single-ended filter with the capacitive J-inverter section.

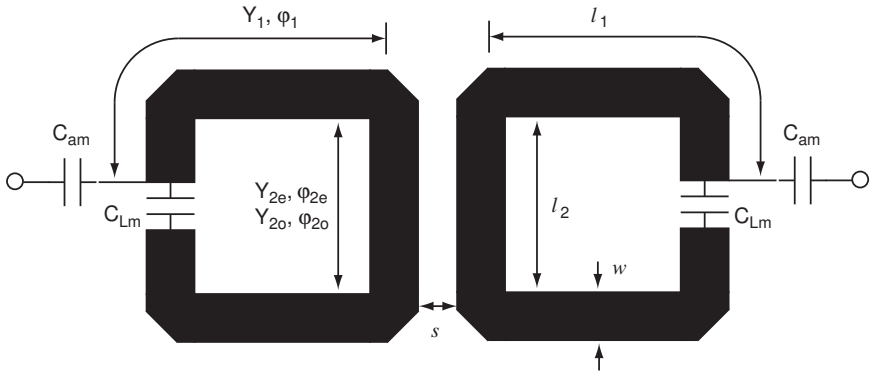

Figure 4.7: The single-ended filter with modified input and loading capacitors.

given by:

$$C_{Lb} = \frac{C_1 - C_b}{2}, \quad C_a = \frac{J_{01}}{\omega_0 \sqrt{1 - (J_{01}/Y_0)^2}} \tag{4.19}$$

where

$$J_{01} = \sqrt{\frac{Y_0 b \Delta}{g_0 g_1}}, \quad C_b = \frac{J_{01}^2}{\omega_0^2 C_a} \tag{4.20}$$

The single-ended filter needs special attention when the *J-inverter* section is realized by series/shunt capacitances (Fig. 4.6). J_{01} in (4.20) needs to be calculated using b in (5.8) and the negative capacitance, -C_b, cannot be absorbed in the loading capacitor, C_L, because the symmetry plane does not exist in the structure any more. Therefore, instead of using the capacitive *J-inverter* section, the modified input capacitance C_{am}, and modified loading capacitor, C_{Lm}, in Fig. 4.7 can be directly found by setting two conditions: Let Z_j and Z_m

be the impedance matrices of the filter networks in Fig. 4.6 and Fig. 4.7, respectively. The reactance value of Z_{m11} and its slope parameter, x_m, should be the same as the reactance value of Z_{j11} and its slope parameter, x_j, around the designed frequency, ω_0. The two conditions are:

$$Im[Z_{m11}(\omega_0)] = Im[Z_{j11}(\omega_0)], \quad x_m(\omega_0) = x_j(\omega_0) \tag{4.21}$$

where

$$x_m = \frac{\omega}{2}\frac{\partial Im\left[Z_{m11}\right]}{\partial\omega}, \quad x_j = \frac{\omega}{2}\frac{\partial Im\left[Z_{j11}\right]}{\partial\omega} \tag{4.22}$$

Equation (4.21) can be solved in terms of C_{am} and C_{Lm} because the impedance Z_{j11} and reactance slope parameter, x_j, can be obtained with known capacitance values, C_a and C_b in Fig. 4.6.

Assuming the admittance, Y_{Lm11}, as Y_{11}, in (6.5) with C_L replaced by C_{Lm}, the impedance, Z_{m11}, is:

$$Z_{m11} = Z_{Lmr} + \frac{1}{j\omega C_{am}} \tag{4.23}$$

where

$$Z_{Lmr} = \frac{Y_{Lm11}}{Y_{Lm11}^2 - Y_{Lm12}^2} \tag{4.24}$$

From the first equality in (4.21), C_{am} is expressed as:

$$C_{am} = \frac{1}{\omega_0} Im\left[\frac{1}{Z_{j11}(\omega_0) - Z_{Lmr}(\omega_0)}\right] \tag{4.25}$$

The reactance slope parameter, x_m, of the modified filter network in Fig. 4.7 is:

$$x_m(\omega_0) = \frac{\omega_0}{2}\frac{\partial Im\left[Z_{Lmr}(\omega_0)\right]}{\partial\omega} + \frac{1}{2\omega_0 C_{am}} \tag{4.26}$$

By using (4.25), x_m can be a function of only C_{Lm}, and is given by:

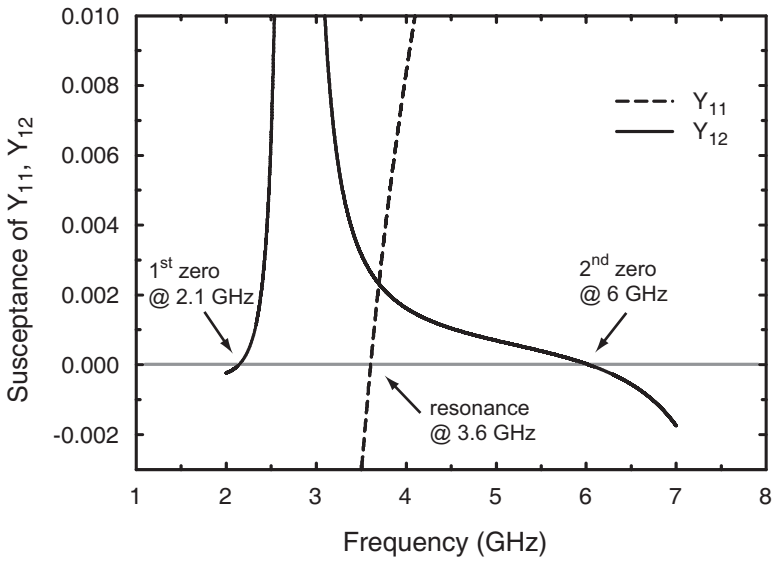

Figure 4.8: Susceptance values of 3.6 GHz filter.

$$x_m(\omega_0) = Im\left[\frac{\omega_0}{2}\frac{\partial Z_{Lmr}(\omega_0)}{\partial\omega} + \frac{1}{Z_{j11}(\omega_0) - Z_{Lmr}(\omega_0)}\right] \tag{4.27}$$

Using the above equation, the second equality in (4.21) gives C_{Lm} and C_{am}, can be then found using (4.25)

4.2.3 Design of the Fixed 3.6 GHz Single-Ended Filter

A 0.1 dB ripple filter with a center frequency of 3.6 GHz and a 4.2% (150 MHz) bandwidth was designed using the equations in the previous section. The initial design parameters are, $w = 1$ mm, $l_1 = 4.6$ mm, $l_2 = 1.5$ mm on a 0.508 mm quartz substrate.

From (4.17), the calculated even-odd mode impedances, Z_{2e} and Z_{2o}, are 59.9 Ω and 43.9 Ω, respectively, and the corresponding gap, s is 0.40 mm. Once the even-odd admittances of the coupled section are found, the loading capacitance, C_1, is given by (4.15). The calculated value of $C_1 = 0.84$ pF, and this corresponds to a loading capacitor, $C_L = 0.42$ pF.

Using the dimensions above, the susceptance values of Y_{11} and Y_{12} in (6.5) are plotted in Fig. 4.8. As can be seen, this filter network resonates at 3.6 GHz and has two transmission zeroes, one at 2.1 GHz and the other at 6 GHz. The locations of the two zeroes will change

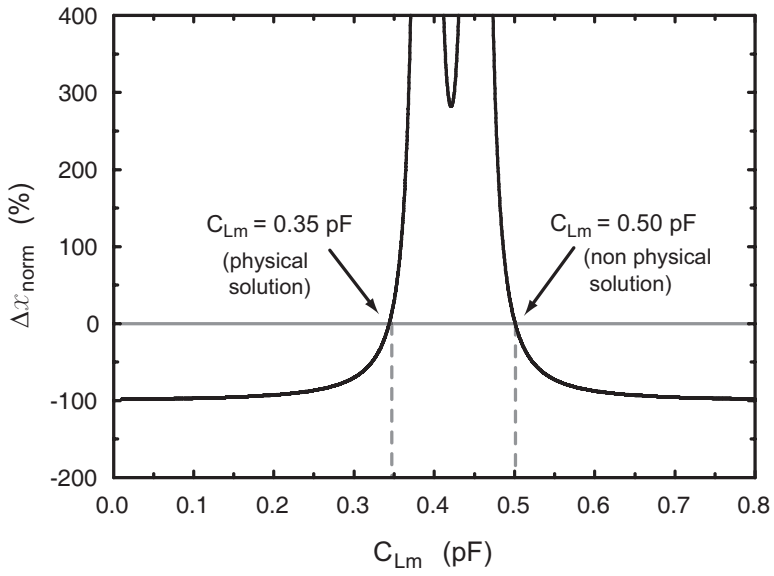

Figure 4.9: Δx_{norm} in terms of C_{Lm}.

slightly after the J-inverter coupling sections are added in the filter.

The modified loading capacitor, C_{Lm}, is found using (4.21) and (4.27). In this case, the variable, Δx_{norm} was defined and plotted in Fig. 4.9. The variable Δx_{norm} is:

$$\Delta x_{norm} = \frac{x_m(\omega_0) - x_j(\omega_0)}{x_j(\omega_0)} \tag{4.28}$$

From Fig. 4.9, C_{Lm} values of 0.35 pF and 0.50 pF are found, but the 0.50 pF is neglected because it results in a negative value of C_{am}. The modified input capacitance, C_{am}, is then given by (4.25) and is 0.40 pF.

4.2.4 Implementation of the Fixed 3.6 GHz Single-Ended Filter

A full-wave simulation of the coupled resonator structure in Fig. 4.3 (without capacitors) is performed using Sonnet[42] and the 4-port Y-parameters are extracted. The 4-port full-

wave Y-matrix is:

$$Y^{4p} = \begin{bmatrix} Y_{11}^{4p} & Y_{12}^{4p} & Y_{13}^{4p} & Y_{14}^{4p} \\ Y_{12}^{4p} & Y_{11}^{4p} & Y_{14}^{4p} & Y_{13}^{4p} \\ Y_{13}^{4p} & Y_{14}^{4p} & Y_{11}^{4p} & Y_{12}^{4p} \\ Y_{14}^{4p} & Y_{13}^{4p} & Y_{12}^{4p} & Y_{11}^{4p} \end{bmatrix} \tag{4.29}$$

The 2-port Y-parameters of the coupled resonator structure in Fig. 4.4 (with capacitors) are found using the symmetric property of the 4-port full-wave network. The 2-port full-wave Y-matrix is:

$$Y^{2p} = \begin{bmatrix} Y_{11}^{4p} - Y_{13}^{4p} + j\omega C_1 & Y_{12}^{4p} - Y_{14}^{4p} \\ Y_{12}^{4p} - Y_{14}^{4p} & Y_{11}^{4p} - Y_{13}^{4p} + j\omega C_1 \end{bmatrix} \tag{4.30}$$

and C_1 is calculated by satisfying $Y_{11}^{2p} = 0$:

$$C_1 = -Im\left[\frac{Y_{11}^{4p}(\omega_0) - Y_{13}^{4p}(\omega_0)}{\omega_0}\right] \tag{4.31}$$

The 2-port Y-parameters of the filter in Fig. 4.2 are then found by inserting C_L between ports 1 and 3 and ports 2 and 4 in (5.24), and open-circuiting ports 3 and 4. The 2-port full-wave Y-matrix is:

$$Y_f = \begin{bmatrix} Y_{f11} & Y_{f12} \\ Y_{f12} & Y_{f11} \end{bmatrix} \tag{4.32}$$

and the Y_{f11} and Y_{f12} are:

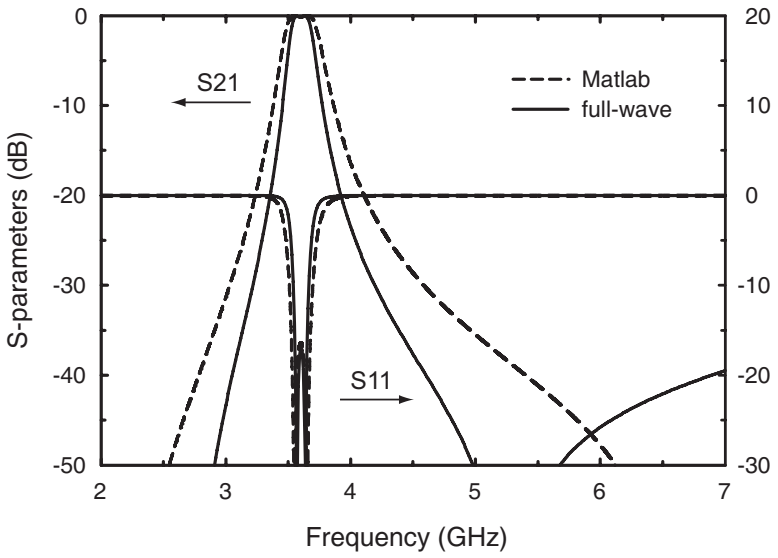

Figure 4.10: Matlab and full-wave simulation of the fixed 3.6 GHz filter.

$$Y_{f11} = Y_{b11}^{4p} - \frac{Y_{b11}^{4p}[(Y_{b13}^{4p})^2 + (Y_{14}^{4p})^2] - 2Y_{12}^{4p}Y_{b13}^{4p}Y_{14}^{4p}}{(Y_{b11}^{4p})^2 - (Y_{12}^{4p})^2} \tag{4.33}$$

$$Y_{f12} = Y_{12}^{4p} - \frac{2Y_{b11}^{4p}Y_{b13}^{4p}Y_{14}^{4p} - Y_{12}^{4p}[(Y_{b13}^{4p})^2 + (Y_{14}^{4p})^2]}{(Y_{b11}^{4p})^2 - (Y_{12}^{4p})^2} \tag{4.34}$$

where

$$Y_{b11}^{4p} = Y_{11}^{4p} + j\omega C_L, \quad Y_{b13}^{4p} = Y_{13}^{4p} - j\omega C_L \tag{4.35}$$

C_{Lm} and C_{am} are then calculated using the procedures in (22)-(29), and are 0.47 pF and 0.36 pF, respectively. The filter responses from the MATLAB calculation [34] and the full-wave simulation are compared in Fig. 4.10. The full-wave simulation results in a larger C_{Lm} than the MATLAB calculation, and this is due to the mitered corners. The mittered corners result in a shorter l_1 and this in turn results in a larger capacitance value than the analytical solution (MATLAB). Also, the full-wave simulation shows a smaller bandwidth

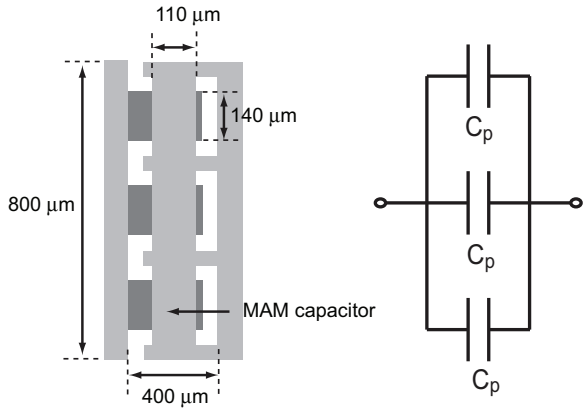

Figure 4.11: Realization of the capacitance values, C_{Lm} and C_{am} (C_p=153 fF, C_{Lm}=C_{am}=3C_p = 460 fF).

(3.4%) than the MATLAB simulation in Fig. 4.10. In the full-wave structure, the resonators are bent inward twice and because of this bending, there is coupling between the l_1 section and the l_2 section. This coupling reduces the coupling in section l_2 and results in a smaller bandwidth. This also explains why the transmission zeros are at different frequencies for the analytical calculation and the full-wave simulations.

When the capacitance values C_{am} and C_{Lm} are physically realized, one needs to consider that although (30) assumes point ports at the open ends of the resonators, a finite area is required to physically implement C_{am} and C_{Lm}. Both C_{am} and C_{Lm} are 0.40 mm long and 0.80 mm wide. The point port assumption is good for C_{Lm} because C_{Lm} fits in the 0.4 mm gap between the open ends of the resonators. However, the point port assumption does not produce the correct value of C_{am} because of the 0.8 mm phyical width of C_{am}. Therefore, in the full-wave simulation including the physical capacitors, the capacitance values are modified to compensate for the shifted input/output ports and the junction effect of the input capacitor. The capacitance values resulting from the MATLAB calculations, the SONNET simulation assuming "point" ports, and the SONNET simulation with physical capacitors are summarized in Table 4.1. The physical C_{Lm} and C_{am} are shown in Fig. 4.11 and are composed of 3 metal-air-metal capacitors, each of value $C_p = 153$ fF ($C_{Lm} = C_{am} = 460$ fF).

Table 4.1: Comparison of Simulated Capacitance Values for the Fixed 3.6 GHz Filter (capacitances are in fF)

	$MATLAB$ (calculation)	$SONNET$ (point ports)	$SONNET$ (physical ports)
C_{Lm}	350	470	460
C_{am}	400	360	460

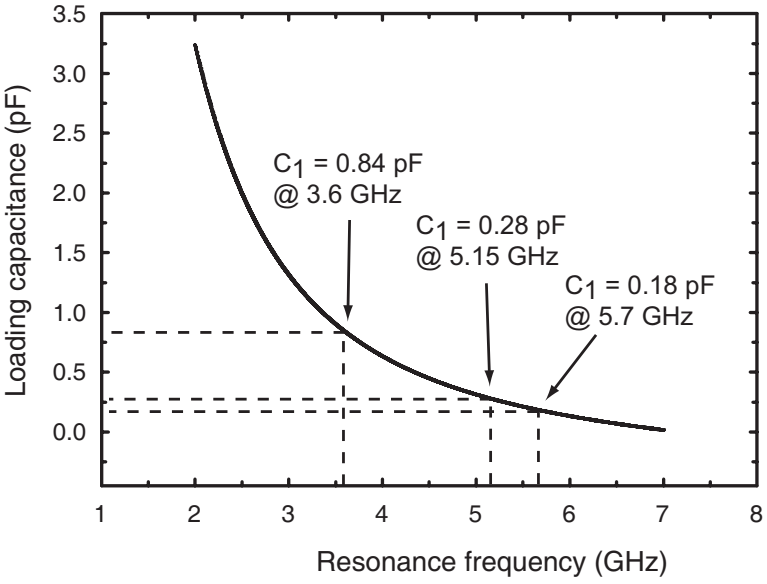

Figure 4.12: Loading capacitor, C_1, in terms of resonance frequency.

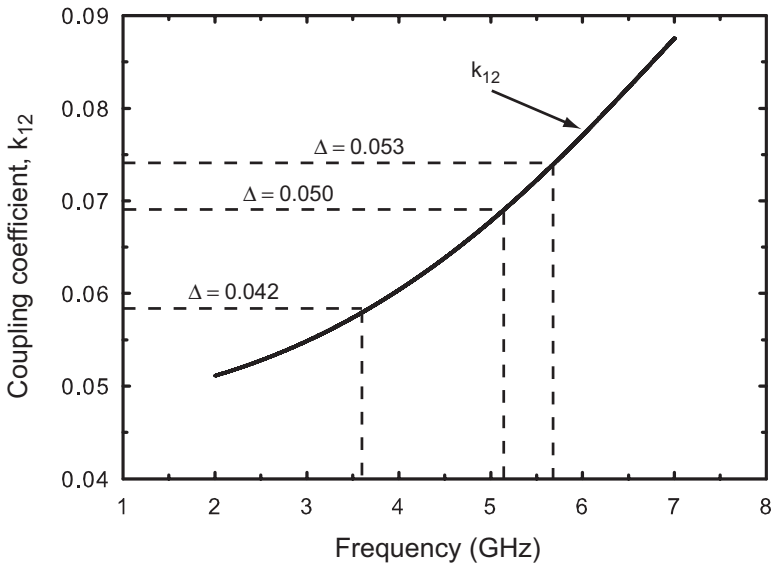

Figure 4.13: Simulated coupling coefficient of the 2-pole filter at 3-6 GHz.

4.2.5 Implementation of the Tunable 5.15-5.70 GHz RF MEMS Filter

The same dimensions as the 3.6 GHz filter are used to design a tunable 5.15-5.70 GHz filter, and the loading capacitances are calculated using (4.15). Fig. 4.12 shows the variation of loading capacitance, C_1, as a function of the resonance frequency, f_0. At 5.15 GHz and 5.70 GHz, the loading capacitance values are 0.28 pF and 0.18 pF, respectively.

In designing a tunable filter, it is important to keep track of the coupling coefficient variation in terms of resonance frequency. Using the relation in (4.17), the coupling coefficient, k_{12} is plotted as a function of f_0 (Fig. 5.7). At 3.6 GHz, the coupling coefficient value corresponds to 4.2% fractional bandwidth. At 5.15 GHz and 5.70 GHz, the coupling coefficient, k_{12}, corresponds to fractional bandwidths of 5.0% and 5.3% respectively.

The calculated (MATLAB) C_{Lm} and C_{am} for 5.15 GHz are 92 fF and 230 fF, respectively and the full-wave simulation results for the same C_{Lm} and C_{am} are 150 fF and 240 fF, respectively. At 5.70 GHz, the MATLAB calculations result in C_{Lm} and C_{am} values of 46 fF and 210 fF, respectively, while the full-wave simulation results are 94 fF and 210 fF, respectively. Again this is mainly due to the mitered corners which have a similar effect at 5.15-5.70 GHz.

To realize the changes in the loading and input capacitance values, the 1-bit switch

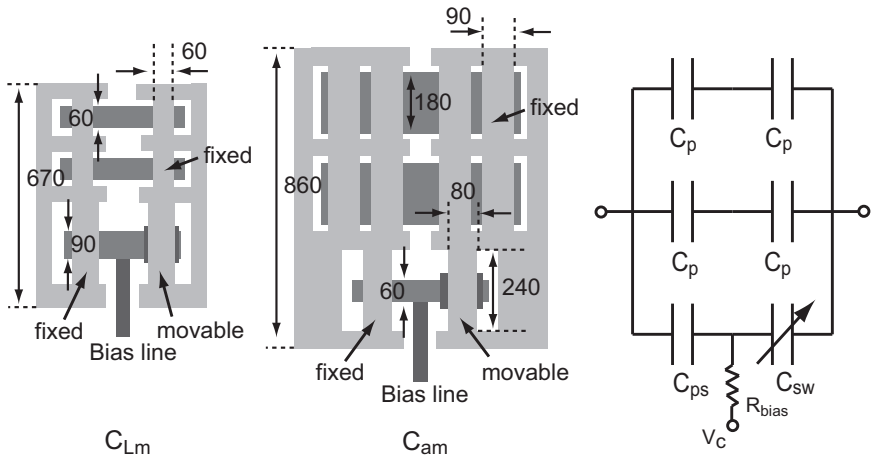

Figure 4.14: Realization of 1-bit capacitance switch network (All dimensions in μm. For C_p and C_{ps} values, see Table 4.2).

Table 4.2: Capacitance Values in Switch Network for the 5.15-5.70 GHz Switchable Filter (capacitances are in fF)

	C_{ps}	C_p	$C_{sw}^{up}/C_{sw}^{down}$	$C_{total}^{up}/C_{total}^{down}$
C_{Lm}	90	45	95/1470	90/130
C_{am}	55	275	70/950	305/325

Table 4.3: Comparison of Simulated Capacitance Values in Switch Network for the 5.15-5.70 GHz Switchable Filter (capacitances are in fF)

$5.15/5.70\ GHz$

	$MATLAB$ (calculation)	$SONNET$ (point ports)	$SONNET$ (physical ports)
C_{Lm}	92/46	150/94	130/90
C_{am}	230/210	240/210	325/300

circuit shown in Fig. 4.14 is proposed, and because of the MEMS fabrication issues, the dimension and aspect ratio of the capacitors are limited. The capacitance values for the switch network are summarized in Table 4.2. In the C_{Lm} networks, there are lines that connect capacitors in series and C_{am} newtorks have 0.86 mm width. Therefore, in full-wave simulation including the capacitors, the capacitance values were modified to compensate for the reactive effects of the lines and the shifted port of the capacitors. (Table 4.3).

4.3 Fabrication and Measurements

4.3.1 3.6 GHz Fixed Filter

The filters were fabricated on a 0.508 mm quartz substrate ($\epsilon_r = 3.78$ and $\tan\delta = 0.0001$) using a standard RF MEMS process developed at the University of Michigan [23], [49]. The resonators are electroplated to 3 μm thick using a low stress gold solution. For the 3.6 GHz filter, metal-air-metal capacitors are used to realize the loading and input capacitors, C_{Lm} and C_{am}. The top electrode of the metal-air-metal capacitor is 3 μm thick. The bottom electrode is 0.6 μm thick and the air gap, g_0, is 1.1$\pm$0.1 μm.

The fabricated 3.6 GHz fixed filter and the measurement set up are shown in Figs. 4.15 and 4.16. The C_{Lm} and C_{am} consist of three metal-air-metal capacitors connected in parallel. The calibration is done using SOLT (Short-Open-Load-Thru) and is referenced to the RF connector. The measurement includes 0.1 dB loss due to the coax-microstrip transition of input ports. The measured and simulated results are plotted in Fig. 4.17, and

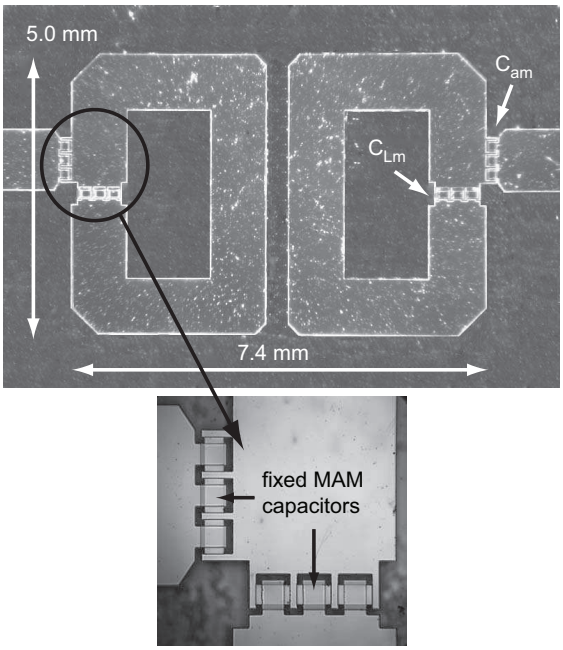

Figure 4.15: Fabricated 3.6 GHz fixed filter on quartz substrate.

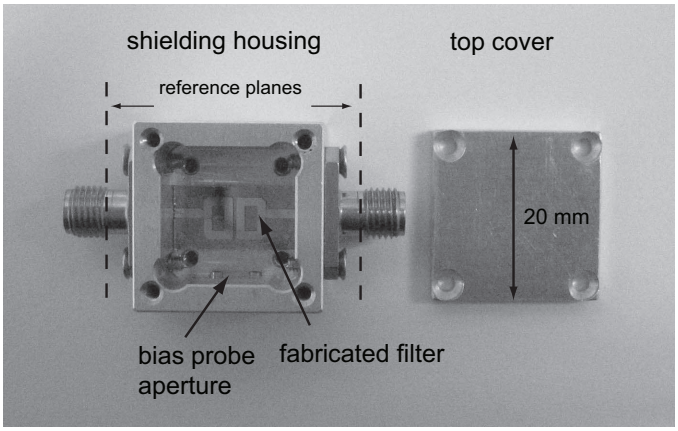

Figure 4.16: The fabricated filter in the shielding housing (cover removed).

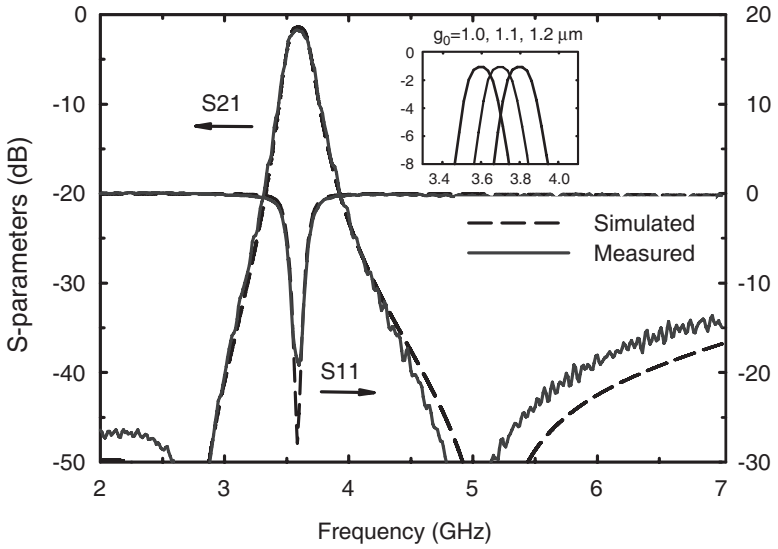

Figure 4.17: Measurement vs. simulation of the fixed 3.6 GHz filter (g_0=1.0 μm).

are in excellent agreement. The measured and simulated insertion loss are 1.8 and 1.7 dB, respectively and the 1 dB bandwidth is 4.0% (144 MHz). The unloaded Q of capacitively loaded resonator was simulated (Q_u = 140) and measured (Q_u = 120) using the critical point method [50].

It is important to note that in Fig. 4.17, we have used g_0 as a fitting parameter in the simulated S-parameters. The reason is that we have a ± 0.1μm uncertainty on g_0 (1.1± 0.1 μm) and the final gap height is not known. A change of ± 0.1μm in g_0 results in a change of ±45 fF in C_{Lm} (or C_{am}) and a change of ±120 MHz in the filter response. In the future, and for precise frequency control, a small analog varactor or a mini-MEMS switch capacitor needs to be used [51].

4.3.2 5.15-5.70 GHz RF MEMS Filter

The fixed metal-air-metal capacitors (C_{sp}, C_p) for the switchable filter have the same characteristics as the previous section. The switch capacitor, C_{sw} uses a 0.18 μm thick Si_3N_4 layer between the MEMS bridge and the bottom electrode. The 0.8 μm sputtered gold layer is suspended 1.1±0.1 μm above the pull-down electrode and the bias lines are fabricated using 0.08 μm-thick $SiCr$ with a resistivity of approximately 2 kΩ/sq and a line

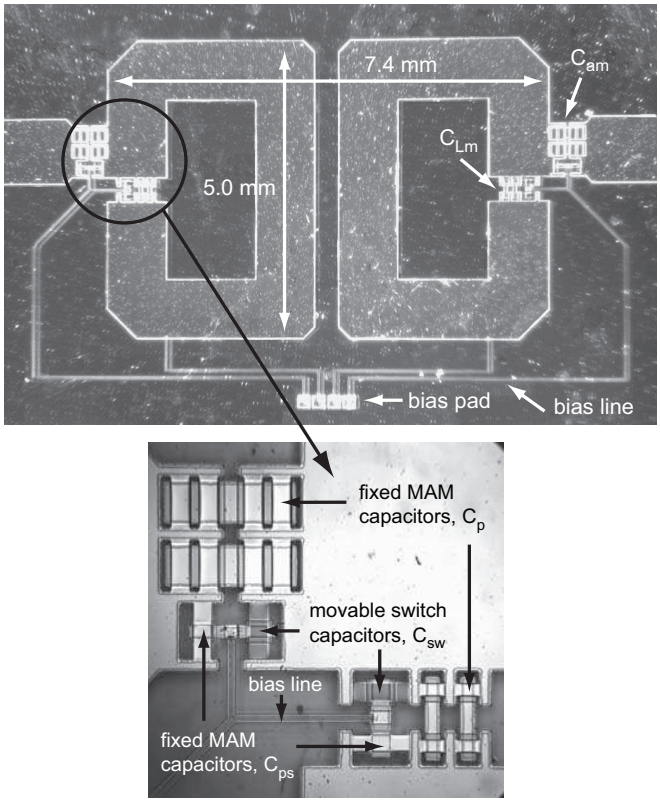

Figure 4.18: Fabricated 5.15-5.70 GHz switchable filter on a quartz substrate.

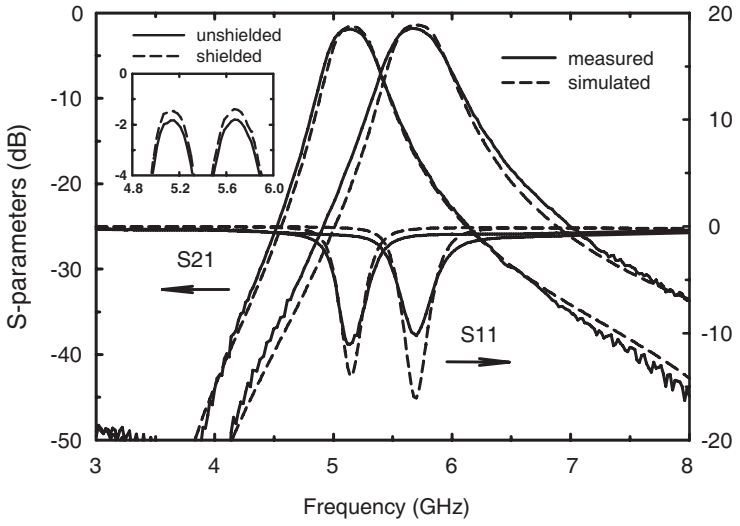

Figure 4.19: Measurement vs. simulation of the 5.15-5.70 GHz tunable filter (g_0=1.1 μm).

Table 4.4: Measured and Simulated Values for the 5.15-5.70 GHz Switchable Filter

Measured/Simulated

	f_0 (GHz)	I.L. (dB)	BW (%)	Q
up-state	5.69/5.70	1.4/1.3	5.0/4.9 (285 MHz)	150/160
down-state	5.14/5.15	1.5/1.4	5.0/4.8 (257 MHz)	140/150

width of 20 μm. The bias line, if not well designed, can degrade filter performance by 1-2 dB [23]. However, in this case, the bias lines have virtually no effect on the filter performance due to the microstrip nature of the filter and the very low coupling to the 2 kΩ/sq lines. The measured pull-down voltage, V_p, is 25 V which corresponds to a spring constant of 67 N/m for a gap of 1.1 μm, and a residual stress of 85 MPa. The mechanical resonance frequency, f_0, quality factor, Q_m and the switching time ($V_a = 1.2V_p$) of the switch are 120 kHz, 0.7, and 4-5 μs, respectively [1].

The fabricated 5.15-5.70 GHz tunable filter is shown in Fig. 4.18. It has two switchable capacitance networks at each resonator. The positive bias lines are connected to each switch (bottom electrode) and the DC ground bias lines are connected to the resonators. Fig.4.19 presents the measured and simulated frequency responses. The center frequencies of both the up and down-states shifted a little (15 MHz). The shift appears to be caused by slightly larger than predicted input capacitance. At 5.15 and 5.70 GHz the measured insertion loss of the filter is 1.8 dB and results in an unloaded Q of 120 (fitted to simulation). When the filters are completely shielded using a top cover, the insertion loss improves by 0.3 dB. Also, the transition loss (0.1 dB) can be extracted from the measured loss. Therefore the actual loss of this filter is 1.5 to 1.4 dB corresponding to an unloaded Q of 140 to 150. The measured and simulated results are summarized in Table. 4.4.

4.3.3 Power Handling of 5.15-5.70 GHz RF-MEMS Filter

The power handling capability of this filter can be studied by analyzing the rms RF voltage across the MEMS switch using a linear model in ADS [37]. This RF voltage partially actuates the MEMS switch and changes the capacitance values of both C_{Lm} and C_{am}. The RF-MEMS switches in C_{Lm} and C_{am} are connected in series, which allows the switches to handle four times more power than the standard shunt switch configuration. Simulations show that the voltage across the C_{Lm} MEMS switch network is more than twice that of the C_{am} switch network and is therefore the main focus of this section. For an RF power of 150 mW, a 10 V rms voltage is present across the C_{Lm} MEMS switch and this reduces the switch height by 0.04 μm and changes the value of C_{Lm} by 0.9 fF. This change is small and a negligible effect on the frequency response is observed. At 350 mW, the rms voltage across the switch becomes 15 V and this corresponds to a switch height change of 0.1 μm and a 2.3 fF change in C_{Lm}. This value is not negligible and shifts the center frequency of the filter by 25 MHz. It should be also noted that in the down-state position and 350 mW RF power, the rms voltage across the switch is only 1.8 V which is smaller than the hold down voltage ($\sim$ 5 V) of the switch. The power handling of this filter can be therefore predicted to be around 300 mW.

4.4 Conclusion

This paper presents a planar RF-MEMS filter with a tunable resonator Q $\simeq$ 150. The filter is based on a capacitively-loaded open-loop resonators which result in a high resonator Q while still allowing for an excellent tuning response. The RF-MEMS tunable filter results in a 5% bandwidth for a tuning range of 5.15$-$5.70 GHz with an insertion loss of only 1.4 to 1.5 dB. It is evident from this work that RF-MEMS are an essential component for high-Q tunable filters. Future work includes improving the tunable resonator Q to $>$ 250 using suspended substrates and demonstration of this technique in the 10-40 GHz range.

Chapter 5

Low-Loss 4-6 GHz Tunable Filter With 3-bit High-Q Orthogonal RF-MEMS Capacitance Network

5.1 Introduction

Low-loss tunable filters are essential for modern wide-band communication systems. Most of them can be classified in three categories; YIG (Yittrium-Iron-Garnet) filters [10], varactor diode filters [12, 14, 15], and RF-MEMS (Micro-Electro-Mechanical-Systems) filters [22, 23, 25, 39]. The YIG filters have muti-octave tuning ranges and a Q up to 10,000, however, their power consumption, tuning speed, size, and weight limit their use in highly integrated communication systems. The varactor diode tuned filters are small in size and with nanosecond tuning speed, but their loss, low power handling, and low linearity have been limiting factors for their use in wireless systems. The RF-MEMS tunable filters occupy a sweet spot between YIG and Schottky-diode filters in terms of being planar and physically small and have zero power consumption, microsecond tuning speeds and excellent linearity (IP3>40 dBm) [16].

The RF-MEMS tunable filters reported so far have an estimated Q of 20-150[22, 23, 25, 39]. The equivalent filter Q is usually 30-80 except for a narrow band switchable case as demonstrated by Park *etal* [39]. In the previous RF-MEMS tunable filters, the loss mechanisms of the multi-bit capacitance tuning network have not been investigated intensively, and as will be shown in this paper, this can have a significant effect on the filter loss.

In this work, the loss mechanisms of the multi-bit capacitance network are analyzed and a novel orthogonal capacitance network design is introduced. Previously, an admittance matrix method based on even and odd-mode analysis was presented in [39] for a two-

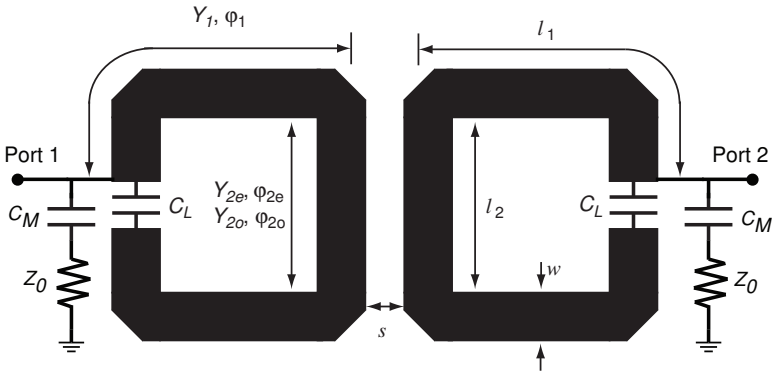

Figure 5.1: Electrical circuit model of the coupled-resonator filter with 2 ports.

state tunable filter. This paper simplifies the design equations in [39] by calculating the loading and matching capacitances directly from the admittance matrix and also taking into account the source-load impedances into the admittance matrix. A design method for the orthogonal capacitance network to achieve uniform step coverage in the frequency response is also presented in detail. These design methods are applied on a capacitively-loaded 2-pole 4-6 GHz tunable filter with 3-bit frequency control (8 states) to achieve state-of-the-art performance.

5.2 Design

5.2.1 Filter Admittance Matrix With Source-Load Impedance Loading

The overall admittance matrix of the filter in Fig. 5.1 is

$$[Y] = \begin{bmatrix} Y_{r11} + \dfrac{j\omega C_M}{1 + Z_0 j\omega C_M} & Y_{r12} \\ Y_{r12} & Y_{r11} + \dfrac{j\omega C_M}{1 + Z_0 j\omega C_M} \end{bmatrix} \tag{5.1}$$

where

$$[Y_r] = \begin{bmatrix} \dfrac{Y_{in\_e} + Y_{in\_o}}{2} & \dfrac{Y_{in\_e} - Y_{in\_o}}{2} \\ \dfrac{Y_{in\_e} - Y_{in\_o}}{2} & \dfrac{Y_{in\_e} + Y_{in\_o}}{2} \end{bmatrix} \tag{5.2}$$

$$Y_{in\_e} = \frac{(c_e - 1)(c_e + 1 - 2d_e\omega C_L)}{j(c_e d_e - d_e^2\omega C_L)} \tag{5.3}$$

$$Y_{in\_o} = \frac{(c_o - 1)(c_o + 1 - 2d_o\omega C_L)}{j(c_o d_o - d_o^2\omega C_L)} \tag{5.4}$$

$$c_{e,o} = \cos 2\phi_1 \cos \phi_{2e,o} - \frac{1}{2}\left(\frac{Y_{2e,o}}{Y_1} + \frac{Y_1}{Y_{2e,o}}\right) \sin 2\phi_1 \sin \phi_{2e,o} \tag{5.5}$$

$$d_{e,o} = \frac{\sin 2\phi_1}{Y_1} \cos \phi_{2e,o} + \left(\frac{\cos^2 \phi_1}{Y_{2e,o}} - \frac{Y_{2e,o} \sin^2 \phi_1}{Y_1^2}\right) \sin \phi_{2e,o} \tag{5.6}$$

and $[Y_r]$ is the filter admittance matrix without C_M and the source-load impedance, Z_0 [39].

5.2.2 Filter Design Using Admittance Matrix Method

Realizing the coupling section of the filter

The coupling section of the filter can be realized using the following coupling condition. The condition is

$$\frac{Im[Y_{r12}(\omega_0)]}{b} = k_{12} \tag{5.7}$$

where

$$b_r = \frac{\omega_0}{2}\frac{\partial Im[Y_{r11}(\omega_0)]}{\partial \omega}, \quad k_{12} = \frac{\Delta}{\sqrt{g_1 g_2}}. \tag{5.8}$$

The slope parameter, b_r, is a function of the design parameters, Y_1, $Y_{2e,o}$, ϕ_1, $\phi_{2e,o}$ and loading capacitor C_L. However, C_L should be decoupled from b_r so as to obtain the design parameters independent of C_L. From the resonance condition, $Im[Y_{r11}(\omega_0)] = 0$, C_L can be rewritten as

$$C_L = \frac{-B(\omega_0) + \sqrt{B(\omega_0)^2 - 4A(\omega_0)D(\omega_0)}}{2\omega_0 A(\omega_0)} \tag{5.9}$$

where

$$A = 2d_o^2 d_e(c_e - 1) + 2d_e^2 d_o(c_o - 1) \tag{5.10}$$

$$B = -2d_o d_e(2c_o c_e - c_o - c_e) - d_o^2(c_e^2 - 1) - d_e^2(c_o^2 - 1) \tag{5.11}$$

$$D = c_o d_o(c_e^2 - 1) + c_e d_e(c_o^2 - 1). \tag{5.12}$$

With C_L replaced with (5.9) in b_r and Y_{r12}, the left-hand side of (5.7) becomes only a function of the distributed design parameters. By choosing the design parameters satisfying (5.7), the filter coupling section can be completed.

Loading and matching capacitor values with source-load impedance loading

Fig. 5.1 shows a complete filter circuit with external coupling elements. When the filter external circuit is realized using a reactive element, one finds that its resonance frequency is shifted due to the complex loading effect of the source-load impedance. To take this complex loading effect into account, the admittance matrix of the complete filter circuit, Y, needs to be used to obtain accurate values of the loading capacitor, C_L, and matching capacitor, C_M.

The value of C_L in (5.9) does not result in the correct resonance frequency (ω_0) when C_M is present. The modified value of C_L and C_M are found by solving the resonance and external coupling conditions, respectively, using (6.5) as,

$$Im[Y_{11}(\omega_0)] = 0 \tag{5.13}$$

$$\frac{b}{Re[Y_{11}(\omega_0)]} = Q_{ext} \tag{5.14}$$

where

$$b = \frac{\omega_0}{2}\frac{\partial Y_{r11}(\omega_0)}{\partial \omega} + \frac{\omega_0}{2}\frac{C_M(1 - Z_0^2\omega_0^2 C_M^2)}{(1 + Z_0^2\omega_0^2 C_M^2)^2} \tag{5.15}$$

$$Q_{ext} = \frac{g_0 g_1}{\Delta}. \tag{5.16}$$

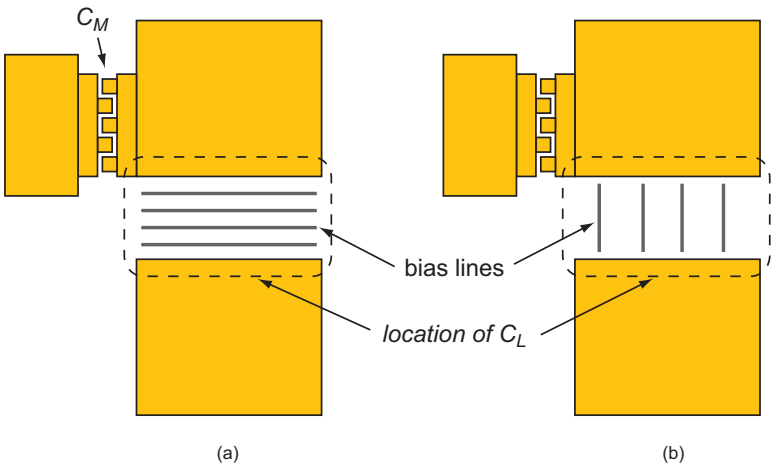

Figure 5.2: The orthogonal (a) and parallel (b) (to the electric field) configuration of the bias lines.

The b and $Re[Y_{11}(\omega_0)]$ include both C_L and C_M and need to be simplified to a function containing only one of them. C_M can be replaced with an equation in terms of $Y_{r11}(\omega_0)$ (function of C_L only) using (5.13). C_M with respect to $Y_{r11}(\omega_0)$ is

$$C_M = \frac{-1 + \sqrt{1 - 4B_{11}^2 Z_0^2}}{2B_{11}Z_0^2} \tag{5.17}$$

where

$$B_{11} = Im[Y_{r11}(\omega_0)]. \tag{5.18}$$

By replacing C_M using (5.17), the left-hand side of the (5.14) becomes a function of only C_L, and C_L can be solved using (5.14). C_M is then determined using (5.17).

5.2.3 Low-Loss Orthogonal Capacitance Network

As is well known, RF-MEMS capacitance networks require high resistance bias lines to actuate the MEMS switches. When multiple bits are realized, the bias lines in the capacitance network couples to the the RF signal and result in additional losses[23].

The effect of the resonant electric field coupled to the bias lines has not been emphasized adequately, but it has significant effect on filter Q. To examine the effects of the resonant electric field in the resonator gap on the bias lines, a 90 MHz butterworth filter centered

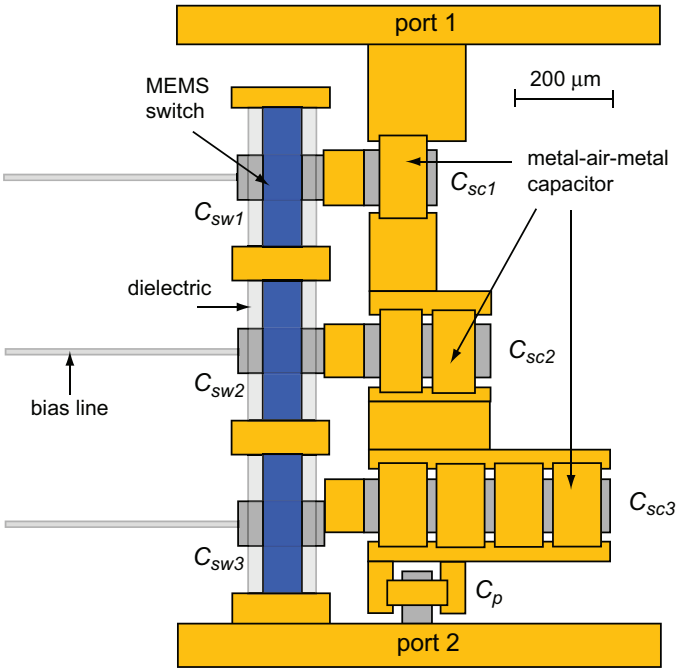

Figure 5.3: The low-low 3-bit C_L orthogonal capacitance network (figure is to scale).

at 5.95 GHz was simulated with the two different bias-line configurations (Fig. 5.2). In this simulation, 5 μm bias line width and 1 kΩ/sq bias line resistance were assumed. The results indicate significantly different pass-band insertion losses. The orthogonal bias-line configuration in Fig. 5.2(a) has almost identical loss (1.08 dB) as the filter without bias lines (1.07 dB) and is independent of the bias line resistance. On the other hand, the parallel bias-line configuration in Fig. 5.2(b) results in 5.14 dB and 1.63 dB insertion loss for 1 kΩ/sq and 10 kΩ/sq. bias-line sheet resistance, respectively. Therefore, the bias lines should be placed orthogonal to, and as far away as possible from, the high electric field area. The suggested *orthogonal* capacitance network in Fig. 5.3 meets all those requirements.

The equivalent circuit is given in Fig. 5.4. Each MEMS switch, C_{sw}, is in series with the scaling capacitor C_{sc} and the C_{sw}-C_{sc} series pairs are all connected in parallel. C_p is used to adjust the overall reactance level of the network and C_f is to take into account the fringing capacitance of port 1 and 2.

The net capacitance value of this network is obtained by calculating the total reactance

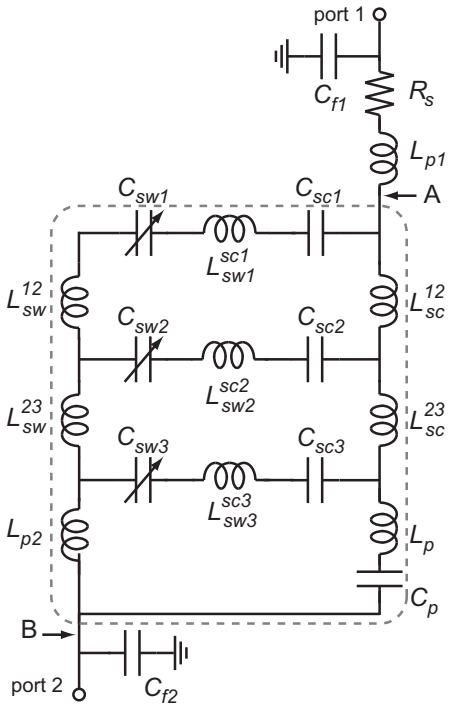

Figure 5.4: The equivalent circuit model of the low-low 3-bit C_L capacitance network.

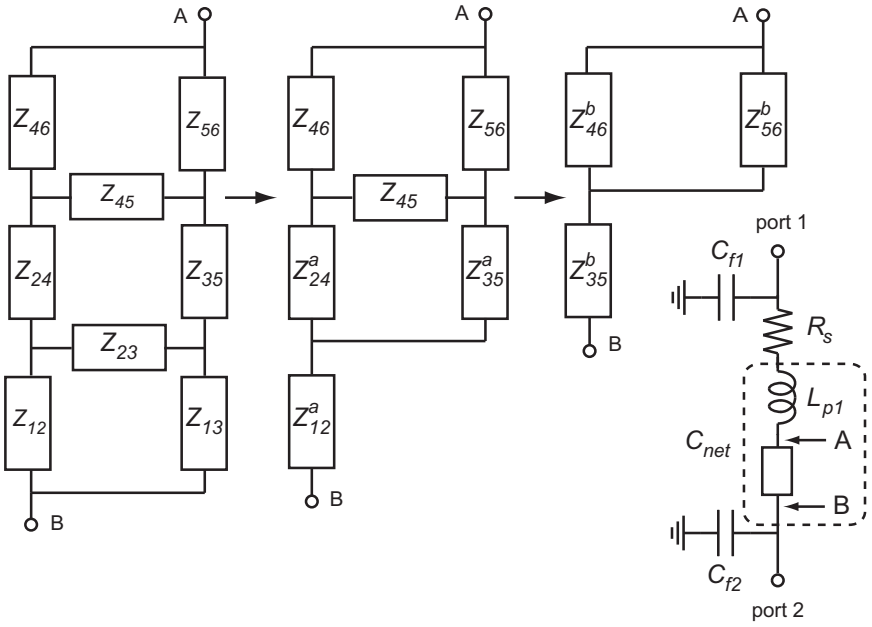

Figure 5.5: The Δ-Y transformation to calculate the net capacitance values of the 3-bit C_L capacitance network.

values. The impedances of the network in Fig. 5.4 are represented in Fig. 5.5 as:

$$Z_{12} = j\omega L_{p2}, \quad Z_{24} = j\omega L_{sw}^{23} \tag{5.19}$$

$$Z_{35} = j\omega L_{sc}^{23}, \quad Z_{56} = j\omega L_{sc}^{12}$$

$$Z_{13} = j\omega L_p + \frac{1}{j\omega C_p}$$

$$Z_{23} = j\omega L_{sw3}^{sc3} + \frac{1}{j\omega C_{sw3}} + \frac{1}{j\omega C_{sc3}}$$

$$Z_{45} = j\omega L_{sw2}^{sc3} + \frac{1}{j\omega C_{sw2}} + \frac{1}{j\omega C_{sc2}}$$

$$Z_{46} = j\omega L_{sw}^{12} + j\omega L_{sw1}^{sc1} + \frac{1}{j\omega C_{sw1}} + \frac{1}{j\omega C_{sc1}}.$$

After performing the first Δ-Y transformations (Fig. 5.5), the impedance values are

$$Z_{12}^a = \frac{Z_{12}Z_{13}}{Z_{12} + Z_{13} + Z_{23}} \tag{5.20}$$

$$Z_{24}^a = \frac{Z_{12}Z_{23}}{Z_{12} + Z_{13} + Z_{23}} + Z_{24}$$

$$Z_{35}^a = \frac{Z_{23}Z_{13}}{Z_{12} + Z_{13} + Z_{23}} + Z_{35}.$$

A second transformation results in

$$Z_{35}^b = Z_{12}^a + \frac{Z_{24}^a Z_{35}^a}{Z_{24}^a + Z_{45} + Z_{35}^a} \tag{5.21}$$

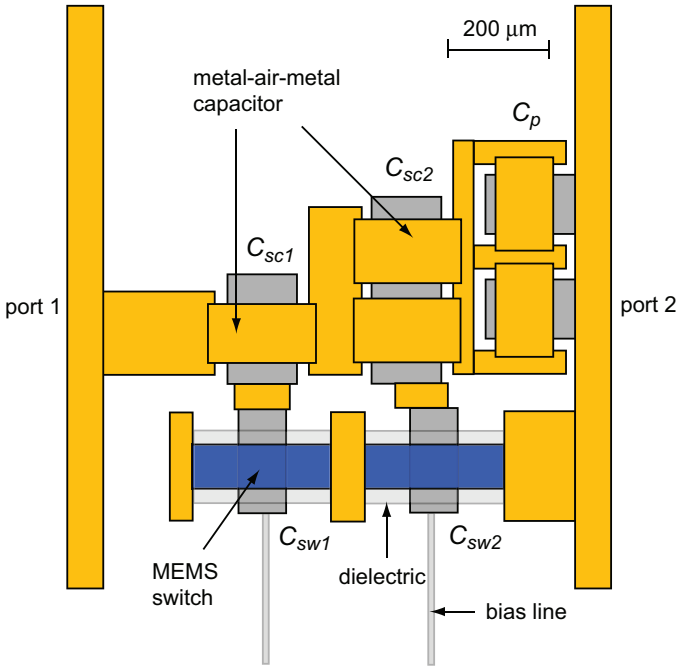

Figure 5.6: The low-low 3-bit C_M orthogonal capacitance network (figure is to scale).

$$Z_{46}^{b} = \frac{Z_{24}^{a} Z_{45}}{Z_{24}^{a} + Z_{45} + Z_{35}^{a}} + Z_{46}$$

$$Z_{56}^{b} = \frac{Z_{45} Z_{35}^{a}}{Z_{24}^{a} + Z_{45} + Z_{35}^{a}} + Z_{56}.$$

The total impedance of the network is therefore

$$Z_{tot} = Z_{35b} + \frac{Z_{46b} Z_{56b}}{Z_{46b} + Z_{56b}} + j\omega L_{p1} + R_s. \tag{5.22}$$

Finally, the total net capacitance value of the capacitance network is

$$C_{net} = \frac{1}{\omega} Im \left[\frac{1}{Z_{tot}} \right]. \tag{5.23}$$

If the fringing capacitance, C_f, is not negligible, it can be added to the above result, and the additional capacitance is C_{f1} in series with C_{f2} due to the differential voltage mode at resonance.

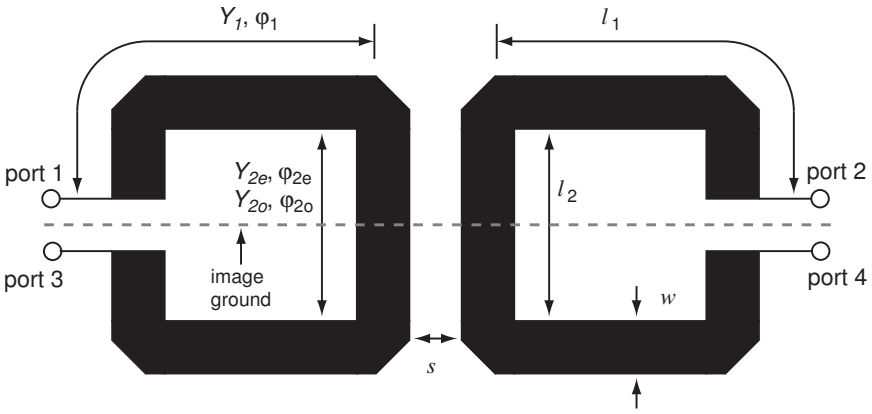

Figure 5.7: Electrical circuit model of the balanced coupled-resonator with 4 ports.

The matching capacitance, C_M, is realized using the same concept as C_L and the layout is shown in Fig. 5.6. The calculation of the net capacitance value also follows the same approach.

5.3 Implementation of the 4-6 GHz Tunable Filter

To design the 4-6 GHz filter, a full-wave simulation of the coupled resonator structure in Fig. 5.7 (without capacitors) is performed using Sonnet[42] and the 4-port Y-parameters are extracted. The full-wave 4-port Y-matrix are

$$[Y^{4p}] = \begin{bmatrix} Y_{11}^{4p} & Y_{12}^{4p} & Y_{13}^{4p} & Y_{14}^{4p} \\ Y_{12}^{4p} & Y_{11}^{4p} & Y_{14}^{4p} & Y_{13}^{4p} \\ Y_{13}^{4p} & Y_{14}^{4p} & Y_{11}^{4p} & Y_{12}^{4p} \\ Y_{14}^{4p} & Y_{13}^{4p} & Y_{12}^{4p} & Y_{11}^{4p} \end{bmatrix}. \tag{5.24}$$

Calculation of the loading capacitance value giving resonance are simpler if the symmetrical properties of this structure are used [39]. The 2-port Y-parameters of the coupled resonator structure with the image ground plane and the loading capacitance, C_{Ls}, between

the port and image ground plane is

$$[Y^{2p}] = \begin{bmatrix} Y_{11}^{4p} - Y_{13}^{4p} + j\omega C_{Ls} & Y_{12}^{4p} - Y_{14}^{4p} \\ \\ Y_{12}^{4p} - Y_{14}^{4p} & Y_{11}^{4p} - Y_{13}^{4p} + j\omega C_{Ls} \end{bmatrix}. \tag{5.25}$$

and the loading capacitance, C_{Ls}, which results in the resonance, $Y_{11}^{2p} = 0$, is

$$C_{Ls} = -Im\left[\frac{Y_{11}^{4p}(\omega_0) - Y_{13}^{4p}(\omega_0)}{\omega_0}\right]. \tag{5.26}$$

The slope parameter of this symmetric network, b^{2p} is

$$b^{2p} = \frac{\omega_0}{2}\frac{\partial Im[Y_{11}^{4p}(\omega_0) - Y_{13}^{4p}(\omega_0)]}{\partial\omega} - \frac{Im[Y_{11}^{4p}(\omega_0) - Y_{13}^{4p}(\omega_0)]}{2} \tag{5.27}$$

and k_{12} is

$$k_{12} = \frac{Im[Y_{12}^{2p}(\omega_0)]}{b^{2p}} = \frac{\Delta}{\sqrt{g_1 g_2}}. \tag{5.28}$$

Determining the coupling of the filter can be done by finding a full-wave simulation set satisfying (5.28) and the loading capacitance, C_{Ls}, is then given by (5.26).

To complete the design with C_M and the modified C_L, the 2-port full-wave Y-parameters in Fig. 5.1 without C_M and source-load loading need to be calculated. The 2-port full-wave matrix is obtained by inserting C_L between ports 1 and 3 and ports 2 and 4 of the 4-port full-wave matrix and open-circuiting ports 3 and 4. The 2-port full-wave Y-matrix is

$$[Y_f] = \begin{bmatrix} Y_{f11} & Y_{f12} \\ Y_{f12} & Y_{f11} \end{bmatrix} \tag{5.29}$$

and the Y_{f11} and Y_{f12} are

$$Y_{f11} = Y_{b11}^{4p} - \frac{Y_{b11}^{4p}[(Y_{b13}^{4p})^2 + (Y_{14}^{4p})^2] - 2Y_{12}^{4p}Y_{b13}^{4p}Y_{14}^{4p}}{(Y_{b11}^{4p})^2 - (Y_{12}^{4p})^2} \tag{5.30}$$

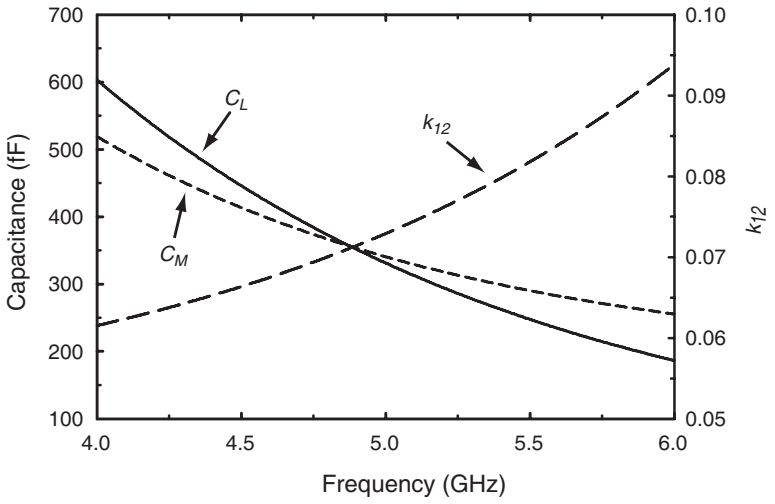

Figure 5.8: The loading capacitor, C_L, matching capacitor, C_M, and coupling coefficient, k_{12}.

$$Y_{f12} = Y_{12}^{4p} - \frac{2Y_{b11}^{4p}Y_{b13}^{4p}Y_{14}^{4p} - Y_{12}^{4p}[(Y_{b13}^{4p})^2 + (Y_{14}^{4p})^2]}{(Y_{b11}^{4p})^2 - (Y_{12}^{4p})^2} \tag{5.31}$$

where

$$Y_{b11}^{4p} = Y_{11}^{4p} + j\omega C_L, \quad Y_{b13}^{4p} = Y_{13}^{4p} - j\omega C_L. \tag{5.32}$$

The modified C_L and C_M values are then calculated using the method explained in 5.

The k_{12}, C_L, and C_M values obtained using full-wave simulations are shown in Fig. 5.8. k_{12} is calculated using (5.28) and increases with frequency due to the partial magnetic coupling nature of the filter. C_{Ls} is calculated using (5.26), and the C_L value between the open ends of the resonator in Fig. (5.7) is half the value of C_{Ls}.

To obtain the capacitance changes in Fig. 5.8, the capacitance networks in Fig. 5.3 and Fig. 5.6 are realized. The parasitic circuit elements of Fig. 5.4 were individually found using full-wave simulations. All the capacitance values were first calculated using the area and height of the MEMS or metal-air-metal capacitors and then the fringing capacitances and the parasitic inductances were extracted by fitting the circuit model to the full-wave simulation model.

To achieve a capacitance change that covers 4-6 GHz frequency range with continuous

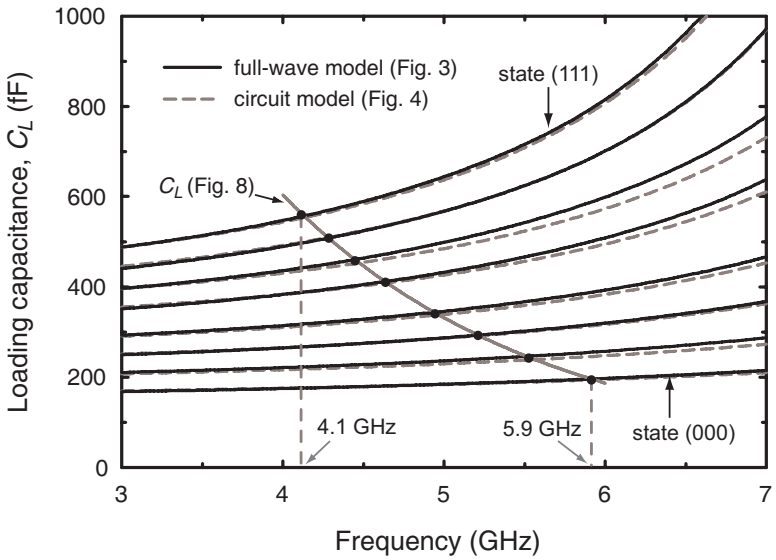

Figure 5.9: The calculated C_{net} using circuit model and full-wave simulation model in fig. 5.3.

step coverage, several simulation steps are needed. First, the C_{sc} values and C_p value are calculated in the equivalent circuit model giving the best step coverage between 4-6 GHz (C_{sw} is fixed due to the fabrication condition of the MEMS device). Then these values are physically realized and simulated using full-wave simulation. The parasitic values such as fringing capacitance and parasitic inductances are extracted with this simulation result, and then the new C_{sc} and C_p are calculated. These steps are repeated until the desired 8 capacitance states are achieved. The equivalent circuit model and full-wave simulation model show a good match at 4-6 GHz. The required C_L values (Fig. 5.8) are also plotted in Fig. 5.9 and show that the realized capacitance network covers well the 4.1-5.9 GHz frequency range.

5.4 Fabrication and Measurements

The RF-MEMS filter was fabricated on a 0.508 mm quartz substrate (ϵ_r=3.78 and tanδ=0.0001) using a standard RF-MEMS process[23]. The MEMS switch has a 0.3-μm thick bottom Au layer and 0.18 μm Si_3N_4 as a dielectric layer, and the 0.8 μm sputtered gold membrane is suspended 1.4-1.6 μm above the dielectric layer. The bias line is 5 μm wide

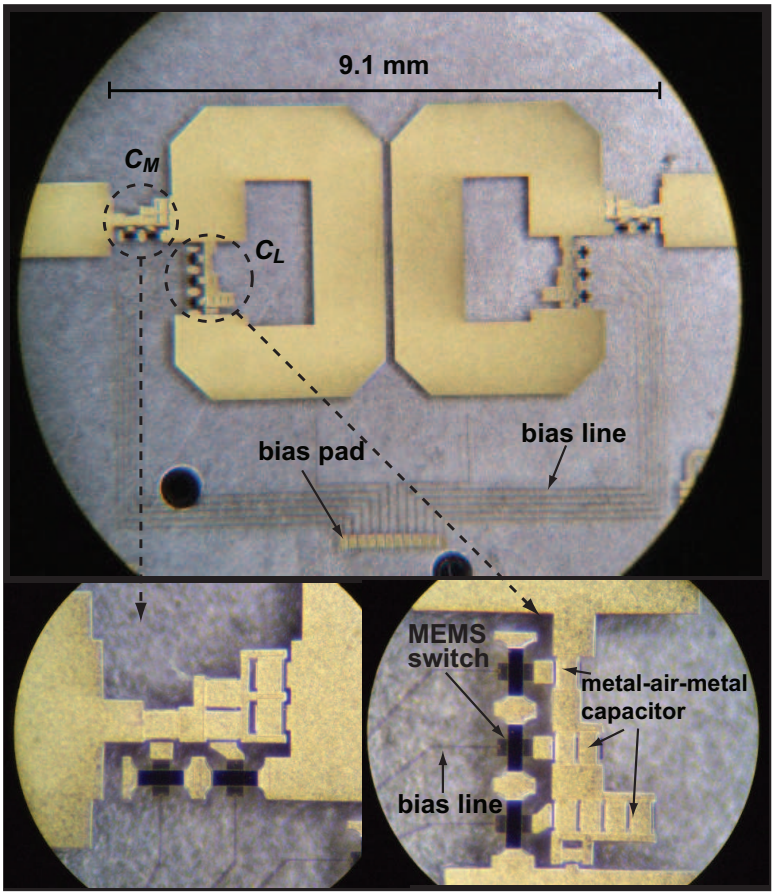

Figure 5.10: Fabricated RF-MEMS tunable filter on quartz substrate.

Table 5.1: Measured 8 states of the RF-MEMS filter.

state	111	011	101	001	110	010	100	000
f_0 (GHz)	4.17	4.38	4.56	4.76	4.97	5.24	5.53	5.91
I.L.(dB)	2.75	2.45	2.37	2.22	2.07	1.73	1.53	1.53
1-dB BW(%)	4.0	4.1	4.4	4.5	4.7	4.6	4.6	4.7
1-dB BW(MHz)	167	180	201	214	234	241	254	278

close to the resonator to minimize the coupling to the electric field and gradually increases to 10-40 μm at the biasing pad. The measured bias line resistance is 8-10 kΩ/sq. The metal-air-metal capacitor is electroplated to 4 μm thick with an air gap of 1.8 μm (dimensions vary between 50 by 60 to 120 by 120 μm). The average pull-down voltage of the MEMS switch is 50 V (40-70 V) and the corresponding spring constant is 196 N/m (residual stress is 260 MPa). The fabricated RF-MEMS filter and its C_L and C_M capacitance networks are shown in Fig. 5.10.

The filter was measured in a shielded box which has an opening on one side for the bias probe. The HFSS[33] simulation shows that the radiation loss 0.05 dB and 0.15 dB with and without the shielding box, respectively (Fig. 5.13). The SOLT (Short-Open-Load-Thru) calibration planes are defined at the connectors. The measured S-parameters are shown in Fig. 5.11. The measured filter covers 4.17 GHz to 5.91 GHz with continuous coverage and 2 to 3 dB crossovers. The measured insertion loss and 1-dB bandwidth at 4.17-5.91 GHz are 2.75-1.53 dB and 4.0-4.7 %, respectively. The fitted Q is 85 at 4.17 GHz and increases to 170 at 5.91 GHz. The measured S_{11} shows an excellent match ($>$ 15 dB) over the entire tuning range except the highest frequency state ($\backsim$ 12 dB), and this is due to one un-actuated switch in C_M. The measured results are summarized in Table 5.1.

The measured and simulated results are plotted in Fig. 5.12 for states (000), (110), and (111). The simulation results are obtained by combining the full-wave model of the coupled resonators (Fig. 5.7) with the model of the capacitance networks. The simulated response is identical with either the equivalent circuit capacitance model or with the full-wave capacitance model and the results are 30-80 MHz lower than the measured values. The

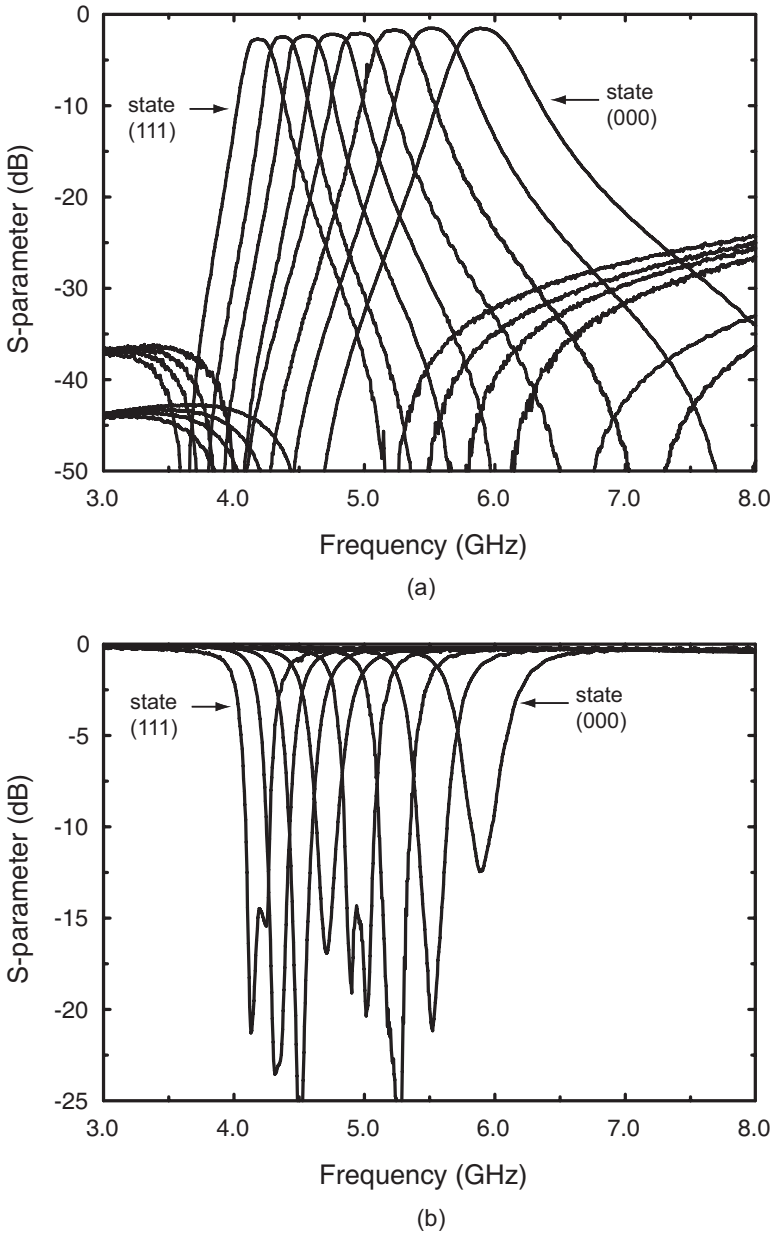

Figure 5.11: Measured S_{21} (a) and S_{11} (b) of the RF-MEMS tunable filter. S_{22} is nearly identical to S_{11} and is not shown.

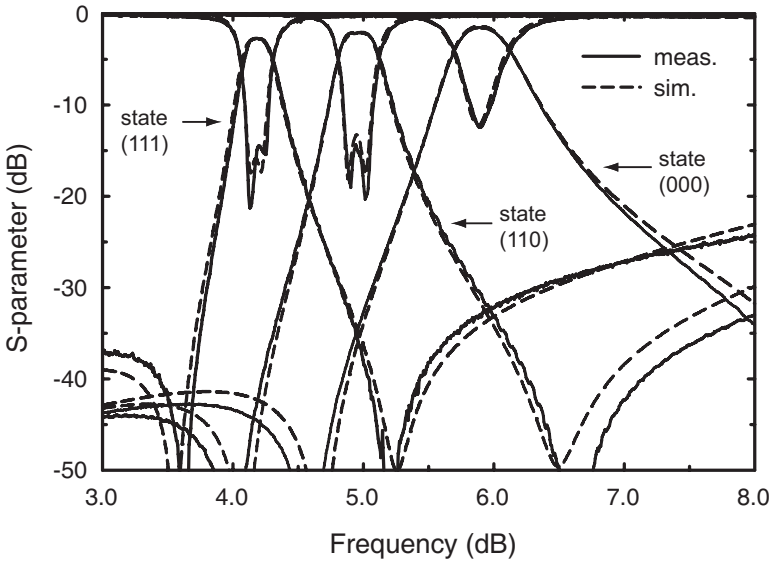

Figure 5.12: Measured and simulated responses of the RF-MEMS tunable filter.

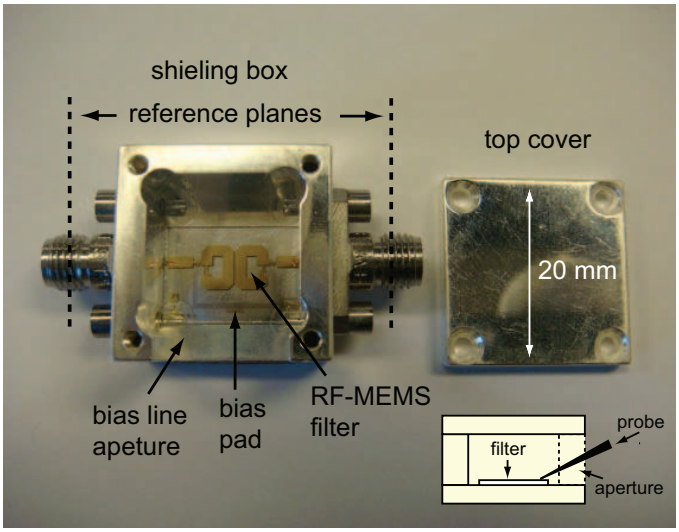

Figure 5.13: RF-MEMS filter in the shielding box.

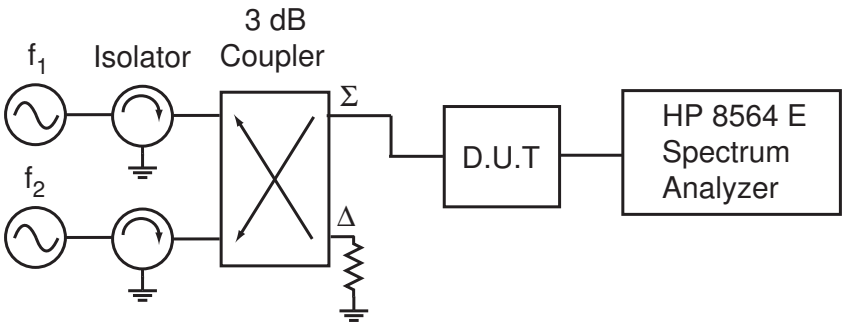

Figure 5.14: Experimental setup for intermodulation measurements.

fabricated Si_3N_4 has a dielectric constant of 6-9 depending on the fabrication conditions and in the original simulation model, the dielectric constant is assumed to be 4.0 due to the roughness of the surface[1]. The simulations in Fig. 5.12 are therefore done with a dielectric constant of 3.75 (instead of 4.0) and show excellent agreement with measurements.

The resonator with 4 μm plating thickness and 1.2 mm width is simulated using Sonnet and the intrinsic Q simulated is 210-245 at 4-6 GHz. This is much higher than the fitted Q of 85-170 and is due to the effected series resistance of the C_L network (R_s=0.9 Ω fitted). The series resistance of C_L is mostly from the thin bottom metal layer (0.3 μm) which is only 0.2-0.25 skin depth thick at 4-6 GHz. A 0.3 μm metal thickness was used for good step coverage in the bridge membrane. If the thickness of the bottom metal layer is increased to 0.6 μm, the series resistance becomes 0.45 Ω, and the overall Q of the loaded resonator increases to 125-210 resulting in an insertion loss of 1.75-1.10 dB at 4-6 GHz.

The nonlinear characterization was done using the experimental setup in Fig. 5.14. The measurement was done on the highest frequency state where all the MEMS switches are in the up-state position and with the highest filter Q and this results in the worst IM_3 products (Fig. 5.15). Measurements show that the IIP_3 is $>$ 37 dBm for $\Delta f >$ 300 kHz. For the RF-MEMS switches, the intermodulation component follows the mechanical response of the bridge, and the IIP_3 level drops by 40 dB/decade for $\Delta f > f_0$ ($f_0 \sim$ 180 kHz). At Δf=1 MHz, the IIP3 is 57 dBm and this is the limit of our measurement setup.

The power handling capability of the filter was investigated by measuring the P-1dB of the filter (Fig. 5.16). The measurement was also done in the highest frequency state and maximum filter Q. One of the switches was actuated down around 27 dBm and this results

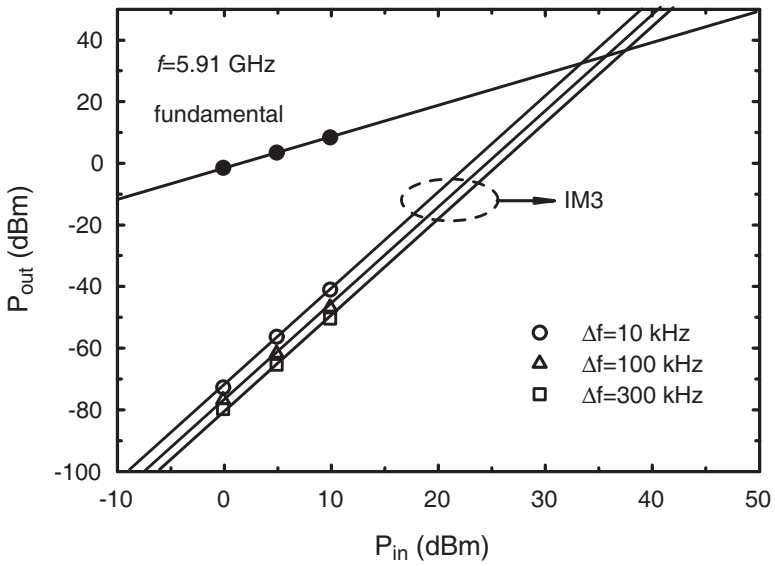

Figure 5.15: Measured IM-products of the RF-MEMS tunable filter.

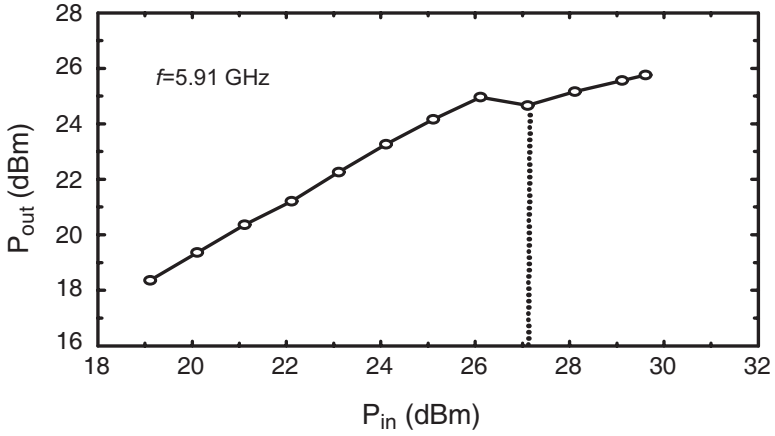

Figure 5.16: Measured P-1dB of the RF-MEMS tunable filter.

in a frequency shift and a 3 dB power loss. Simulations show that an RF power of 0.5-1.0 W results in an RF rms voltage of 30-40 V at C_{sw3}, and this is enough to move switch and distort the filter response.

5.5 Conclusion

Low-loss tunable filter with 3-bit high-Q Orthogonal RF-MEMS capacitance network were designed, fabricated, and measured. The lossy coupling between the resonant electric field and the bias lines in the multi-bit RF-MEMS capacitance network were analyzed and the orthogonal capacitance network design was suggested to minimize the lossy coupling. The Q of the measured filter is 85-170 at 4-6 GHz and this is a state-of-the-art result. The Q can be enhanced to 125-210 with the use of a thicker bottom electrode (0.6 μm). A suspended resonator design with small loading capacitance values ($X_C >$ j300 Ω) can result in a filter Q up to 300 and this is being done at UCSD.

Chapter 6

5.1-5.8 GHz CPW RF-MEMS Switchable Filter on Si Substrate with Mirrored Transmission Zeroes

6.1 Introduction

In this work, a switchable RF-MEMS filter with mirrored transmission zeroes is presented. Each transmission zero at the up and down-state is designed to be located close to the other frequency band, and as a result, the isolation between the two frequency bands is enhanced by more than 10 dB. A detailed design consideration for controlling the transmission zero location is presented, and a coupling sign change for the switching transmission zero is discussed. The filter is designed on a Si substrate with a CPW implementation for possible integration with CMOS technology.

6.1.1 Design

Fig. 6.1 shows the electrical circuit model of the filter. The loading capacitor, C_{L0}, is located at the open end of the uncoupled section and this reduces the resonator length, and the switchable capacitor, C_{Lsw}, and the coupling capacitor, C_C, are placed at the end of the coupled section. C_{Lsw} controls the resonance frequency, and C_C balances the absolute values of coupling in the up and down-states, realizing mirrored transmission zeroes when the switch is activated.

When the even-mode is excited, C_C becomes zero due to the even-mode symmetry, and the even-mode admittance seen from port 1 to the upper section of the resonator is

$$Y_{ue} = Y_{2e}\frac{\left(Y_3\frac{j\omega C_{L0} + jY_3\tan\phi_3}{Y_3 - \omega C_{L0}\tan\phi_3} + j\omega C_{Lsw}\right) + jY_{2e}\tan\phi_{2e}}{Y_{2e} + j\left(Y_3\frac{j\omega C_{L0} + jY_3\tan\phi_3}{Y_3 - \omega C_{L0}\tan\phi_3} + j\omega C_{Lsw}\right)\tan\phi_{2e}}. \tag{6.1}$$

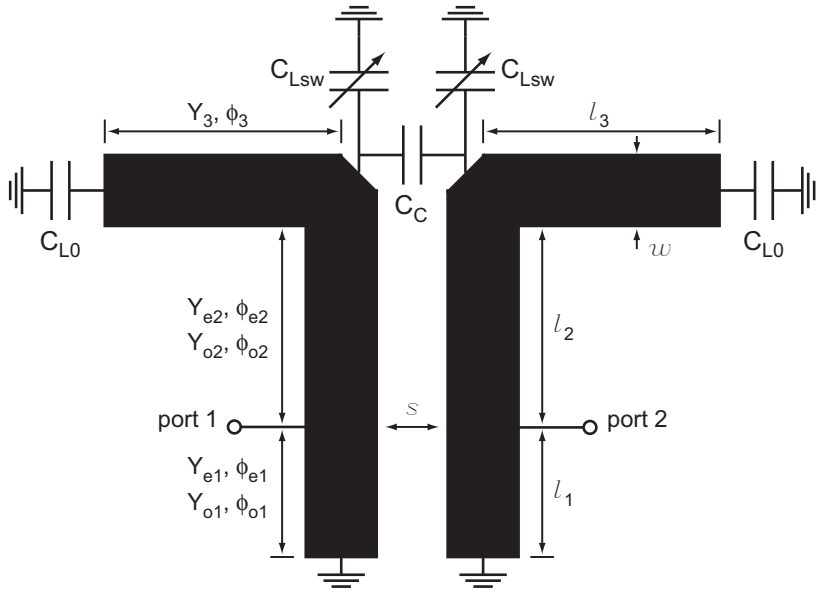

Figure 6.1: Electrical circuit model of the switchable filter.

With the odd-mode excitation, C_C becomes $2C_C$ due to the virtual ground plane, and the odd-mode admittance from port 1 to the upper section of the resonator is

$$Y_{uo} = Y_{2o}\frac{\left(Y_3\frac{j\omega C_{L0}+jY_3\tan\phi_3}{Y_3-\omega C_{L0}\tan\phi_3}+j\omega C_{Lsw}+j\omega 2C_C\right)+jY_{2o}\tan\phi_{2o}}{Y_{2o}+j\left(Y_3\frac{j\omega C_{L0}+jY_3\tan\phi_3}{Y_3-\omega C_{L0}\tan\phi_3}+j\omega C_{Lsw}+j\omega 2C_C\right)\tan\phi_{2o}}. \tag{6.2}$$

The even and odd-mode admittances of the lower section are the admittances of the even and odd mode lines shorted at one ends. The lower and upper sections are connected in parallel, therefore, the even and odd-mode admittances seen from port 1, Y_{ine} and Y_{ino}, are, respectively

$$Y_{ine} = Y_{2e}\frac{\left(Y_3\frac{j\omega C_{L0}+jY_3\tan\phi_3}{Y_3-\omega C_{L0}\tan\phi_3}+j\omega C_{Lsw}\right)+jY_{2e}\tan\phi_{2e}}{Y_{2e}+j\left(Y_3\frac{j\omega C_{L0}+jY_3\tan\phi_3}{Y_3-\omega C_{L0}\tan\phi_3}+j\omega C_{Lsw}\right)\tan\phi_{2e}} - jY_{1e}cot\phi_{1e}, \tag{6.3}$$

$$Y_{ino} = Y_{2o}\frac{\left(Y_3\frac{j\omega C_{L0}+jY_3\tan\phi_3}{Y_3-\omega C_{L0}\tan\phi_3}+j\omega C_{Lsw}+j\omega 2C_C\right)+jY_{2o}\tan\phi_{2o}}{Y_{2o}+j\left(Y_3\frac{j\omega C_{L0}+jY_3\tan\phi_3}{Y_3-\omega C_{L0}\tan\phi_3}+j\omega C_{Lsw}+j\omega 2C_C\right)\tan\phi_{2o}} - jY_{1o}cot\phi_{1o}. \tag{6.4}$$

The overall admittance matrix of the 2-port filter network is

$$Y = \begin{bmatrix} \frac{Y_{ine}+Y_{ino}}{2} & \frac{Y_{ine}-Y_{ino}}{2} \\ \frac{Y_{ine}-Y_{ino}}{2} & \frac{Y_{ine}+Y_{ino}}{2} \end{bmatrix} \tag{6.5}$$

The network needs to satisfy two filter conditions, and the two conditions are

$$Im[Y_{11}(\omega_0)] = 0, \tag{6.6}$$

$$\frac{Im[Y_{12}(\omega_0)]}{b} = k_{12}, \tag{6.7}$$

where

$$b = \frac{\omega_0}{2}\frac{\partial Im[Y_{11}]}{\partial \omega}, \quad k_{12} = \frac{\Delta}{\sqrt{g_1 g_2}}. \tag{6.8}$$

Solving (6.6) and (6.7) are not straight forward because Y_{11} and Y_{12} are functions of all other design parameters (Fig. 6.1). The first design step is to determine the characteristic impedance of the resonator. It can a value result in the highest Q, or the most balanced value for this specific geometry. Once the resonator impedance is set, C_{L0} is chosen for the admittance slope and appropriate resonator length. The coupled line section, C_{Lsw} and C_C are then calculated based on the up and down-state frequencies and the locations of the two transmission zeroes. Calculating all the design parameters using (6.6) and (6.7) is difficult because all the lumped parameters C_{L0}, C_{Lsw}, and C_C are coupled in (6.6) and (6.7). The complexity of the design equations can be significantly reduced by re-defining ports at the junction of upper and lower resonator sections (Fig. 6.2).

The even and odd-mode input admittances of the coupled resonators with shifted ports are

$$Y_{ine}^{p} = Y_3\frac{j\omega C_{L0} + jY_3\tan\phi_3}{Y_3 - \omega C_{L0}\tan\phi_3} + j\omega C_{Lsw} + Y_{2e}\frac{-jY_{1e}\cot\phi_{1e} + jY_{2e}\tan\phi_{2e}}{Y_{2e} + Y_{1e}\cot\phi_{1e}\tan\phi_{2e}}, \tag{6.9}$$

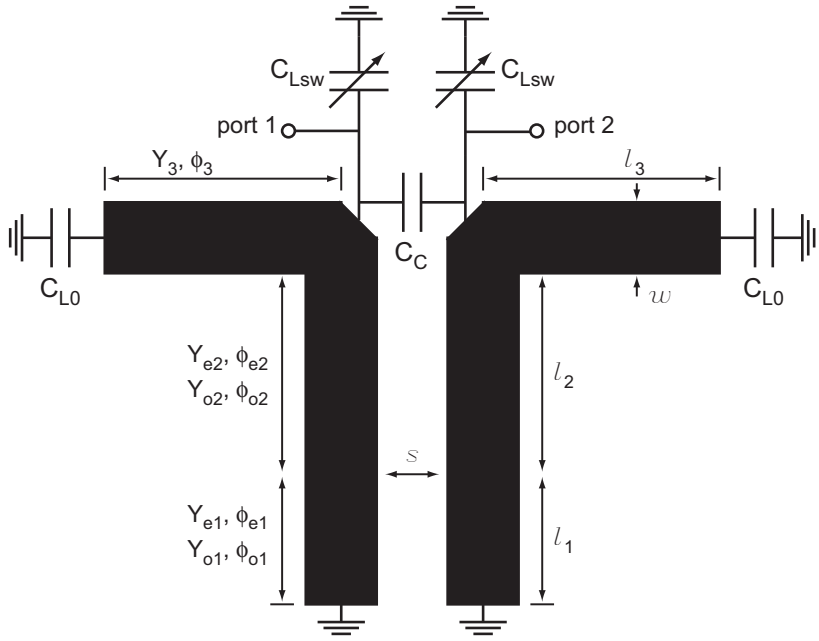

Figure 6.2: Electrical circuit model of the switchable filter.

$$Y_{ino}^{p} = Y_3 \frac{j\omega C_{L0} + jY_3 \tan\phi_3}{Y_3 - \omega C_{L0} \tan\phi_3} + j\omega C_{Lsw} + j2\omega C_C + Y_{2o} \frac{-jY_{1o}\cot\phi_{1o} + jY_{2o}\tan\phi_{2o}}{Y_{2o} + Y_{1o}\cot\phi_{1o}\tan\phi_{2o}}. \quad (6.10)$$

The overall admittance matrix of the filter with shifted ports is

$$[Y^p] = \begin{bmatrix} \frac{Y_{ine}^p + Y_{ino}^p}{2} & \frac{Y_{ine}^p - Y_{ino}^p}{2} \\ \frac{Y_{ine}^p - Y_{ino}^p}{2} & \frac{Y_{ine}^p + Y_{ino}^p}{2} \end{bmatrix}. \quad (6.11)$$

$[Y^p]$ can be rewritten in terms of $Y_{ue,o}^p$ (even/odd-mode admittance toward upper section) and $Y_{de,o}^p$ (even/odd-mode admittance toward lower section), and is

$$Y^p = \begin{bmatrix} \frac{Y_{ue}^p + Y_{de}^p + Y_{uo}^p + Y_{do}^p}{2} + j\omega C_{Lsw} + j\omega C_C & \frac{Y_{ue}^p + Y_{de}^p - Y_{uo}^p - Y_{do}^p}{2} + j\omega C_{Lsw} - j\omega C_C \\ \frac{Y_{ue}^p + Y_{de}^p - Y_{uo}^p - Y_{do}^p}{2} + j\omega C_{Lsw} - j\omega C_C & \frac{Y_{ue}^p + Y_{de}^p + Y_{uo}^p + Y_{do}^p}{2} + j\omega C_{Lsw} + j\omega C_C \end{bmatrix}, \quad (6.12)$$

where

$$Y_{ue}^p = Y_3 \frac{j\omega C_{L0} + jY_3 \tan\phi_3}{Y_3 - \omega C_{L0}\tan\phi_3}, \quad Y_{uo}^p = Y_3 \frac{j\omega C_{L0} + jY_3 \tan\phi_3}{Y_3 - \omega C_{L0}\tan\phi_3}, \quad (6.13)$$

$$Y_{de}^{p} = Y_{2e}\frac{-jY_{1e}\cot\phi_{1e} + jY_{2e}\tan\phi_{2e}}{Y_{2e} + Y_{1e}\cot\phi_{1e}\tan\phi_{2e}}, \quad Y_{do}^{p} = Y_{2o}\frac{-jY_{1o}\cot\phi_{1o} + jY_{2o}\tan\phi_{2o}}{Y_{2o} + Y_{1o}\cot\phi_{1o}\tan\phi_{2o}}. \tag{6.14}$$

By applying (6.6) to $[Y^p]$, C_{Lsw} and C_C can be given by

$$\omega_0 C_{Lsw} + \omega_0 C_C = -Im\left[Y_{r11}(\omega_0)\right], \tag{6.15}$$

where

$$Y_{r11} = \frac{Y_{ue}^{p} + Y_{de}^{p} + Y_{uo}^{p} + Y_{do}^{p}}{2}. \tag{6.16}$$

The slope parameter, b, is then

$$b = \frac{\omega_0}{2}\frac{\partial Im[Y_{r11}(\omega_0)]}{\partial\omega} - \frac{Im[Y_{r11}(\omega_0)]}{2}. \tag{6.17}$$

The steps given so far decouple C_{Lsw} and C_C from the slope parameter, b, thus simplify (6.6) and (6.7). The coupling condition (6.7) with simplified b is

$$\frac{Im[Y_{r12}(\omega_0)] - Im[Y_{r11}(\omega_0)] - 2\omega_0 C_C}{\frac{\omega_0}{2}\frac{\partial Im[Y_{r11}(\omega_0)]}{\partial\omega} - \frac{Im[Y_{r11}(\omega_0)]}{2}} = \frac{\Delta}{\sqrt{g_1 g_2}}, \tag{6.18}$$

where

$$Y_{r12} = \frac{Y_{ue}^{p} + Y_{de}^{p} - Y_{uo}^{p} - Y_{do}^{p}}{2}. \tag{6.19}$$

The filter has two pass-bands (up and down-states) and two mirrored transmission zero frequencies. By applying these four conditions to (6.18), the design parameters, $l_1 + l_2$, s, C_{L0}, and C_C can be determined:

$$\frac{Im[Y_{12}^{p}(\omega_1)]}{b(\omega_1)} = \frac{\Delta}{\sqrt{g_1 g_2}}, \quad , \frac{Im[Y_{12}^{p}(\omega_2)]}{b(\omega_2)} = \frac{\Delta}{\sqrt{g_1' g_2'}}, \tag{6.20}$$

$$Im[Y_{12}^{p}(\omega_{p1})] = 0, \quad Im[Y_{12}^{p}(\omega_{p2})] = 0, \tag{6.21}$$

where ω_1 and ω_2 are 1^{st} and 2^{nd} pass band, and ω_{p1} and ω_{p2} are 1^{st} and 2^{nd} transmission

Table 6.1: Design parameters of the 2-pole 4% filter on a 0.508 mm, Si-substrate (dimensions are in mm, impedances are in Ω).

w/g	s	l_1	l_2	l_3
0.2 / 0.1	0.3	0.4	0.8	0.4
Z_{e1}	Z_{o1}	Z_{e2}	Z_{o2}	Z_3
77.0	29.0	77.0	29.0	50.5
ϵ_{eff}^{e1}	ϵ_{eff}^{o1}	ϵ_{eff}^{e2}	ϵ_{eff}^{o2}	ϵ_{eff}^{3}
6.27	6.15	6.27	6.15	6.32

zero frequencies. Once $l_1 + l_2$, s, C_{L0}, and C_C are found, the up and down-state switchable capacitances, C_{Lsw}^{up}, and C_{Lsw}^{down} can be obtained using (6.15), and this completes filter design procedures.

A tapping input is used to realize an external coupling of the filter. External quality factor, Q_{ext}, is a function of tapping position, l_1, and can be given by

$$\frac{b}{Y_0} = \frac{\frac{\omega_0}{2}\frac{\partial Im[Y_{r11}(\omega_0)]}{\partial\omega} - \frac{Im[Y_{r11}(\omega_0)]}{2}}{Y_0} = \frac{g_0 g_1}{\Delta}. \tag{6.22}$$

6.1.2 Implementation

A 0.1 dB ripple, 4 % filter was designed using the admittance matrix method in the above section. The up-state frequency is 5.80 GHz, and its transmission zero is located at 5.6 GHz. The down-sate is centered at 5.10 GHz, and its transmission zero frequency is 5.4 GHz. The overall resonator length and characteristic impedances are 1.6 mm, and 50.5 Ω, respectively, and the resonator width, w, and the gap between the resonator and CPW ground, g, are 0.2 mm, and 0.1 mm, respectively. From (6.21) and (6.20), the even and odd-mode impedances of coupled resonators are 77.0 Ω and 29.0Ω, respectively, which corresponds to s and $l_1 + l_2$ of 0.3 mm and 1.2 mm, respectively. Detailed design parameters are summarized in Table 6.1.

The actual layout of the filter can be seen in Fig. 6.3. The switchable capacitor, C_{Lsw}, is composed of two series connected capacitors: the scaling capacitor, C_{sc}, and the switch

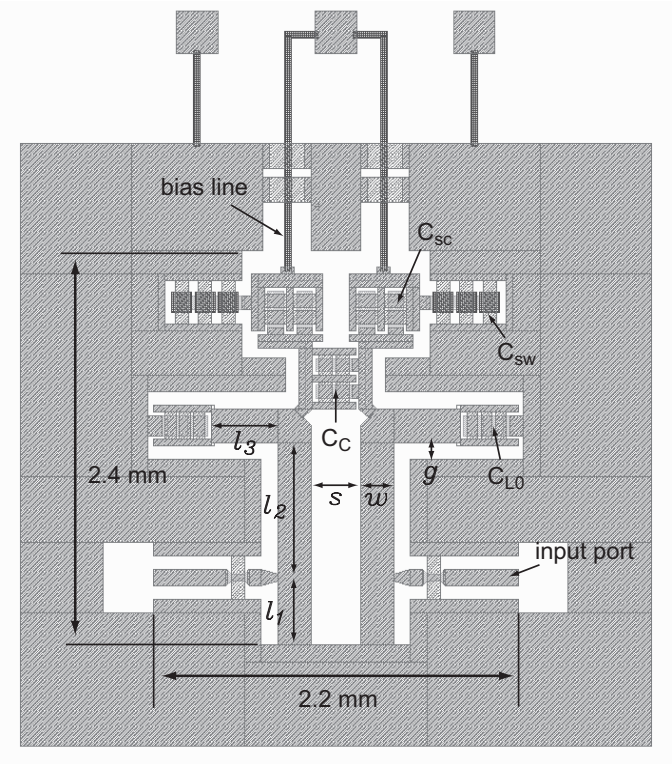

Figure 6.3: Layout of the switchable filter.

Table 6.2: Capacitance values for 5.15 - 5.80 GHz switchable filter (capacitances are in pF)

C_{sw}^{up} / C_{sw}^{up}	C_{sc}	C_C	C_{L0}
0.29 / 7.11	0.35	0.28	0.32

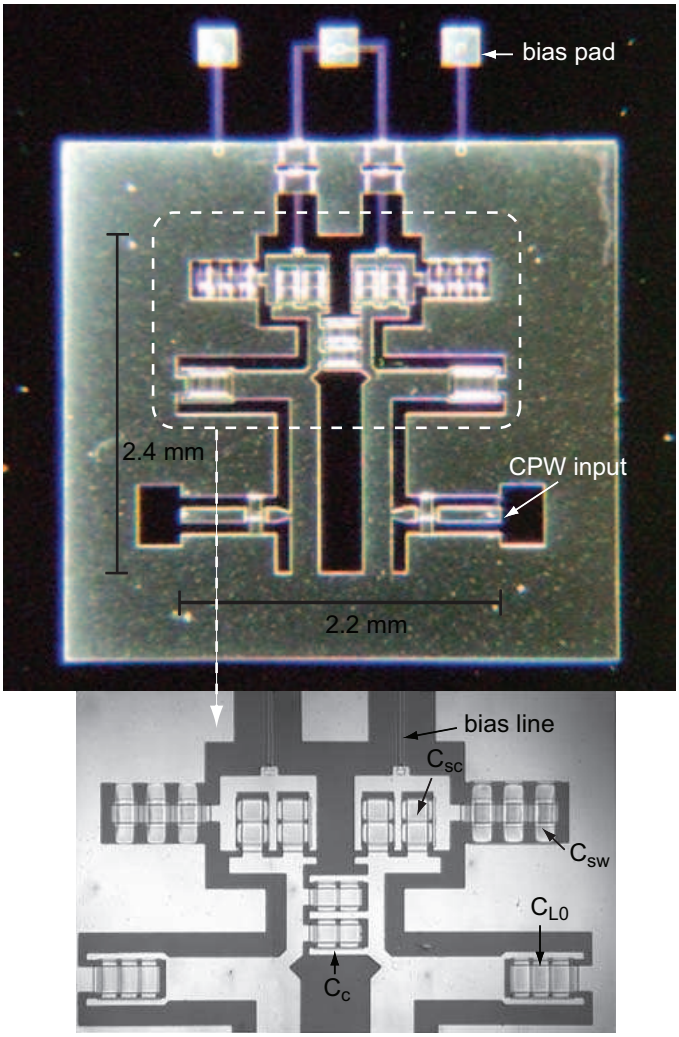

Figure 6.4: Layout of the switchable filter.

capacitance, C_{sw}. Capacitance values for C_{Lsw}, C_C, and C_{L0} are summarized in Table 6.2.

6.1.3 Fabrication and Measurement

The filter was fabricated on 0.508 mm thick Si substrate (ϵ_r=10.6) using standard MEMS process [23, 49]. (Fig. 6.4). The resonators and metal-air-metal capacitors are electroplated to 3 μm thick and the bottom electrode has 0.6 μm thickness. The MEMS capacitive switch is 0.8 μm thick sputtered gold and is suspended 1.4-1.6μm above 0.2 μm thick deposited Si_3N_4 dielectric on the bottom metal. Bias lines are realized using 20μm width $SiCr$ layer and the measured resistance is 3kΩ/sq. The actuation voltage is about 23 V and

Table 6.3: Simulated and measured results of the mirrored response filter.

simulated/measured

	f_0 (GHz)	I.L. (dB)	1-dB BW (%)	f_p (GHz)
up	5.78/5.95	2.3/9.8	4.0/3.0	5.40/5.46
down	5.12/5.21	2.9/9.1	4.0/3.0	5.63/5.76

its corresponding spring constant and mechanical resonance frequency are 25 N/m, and 72 kHz, respectively. The overall size of the fabricated filter is 2.4 x 2.2 mm^2.

Fig. 6.5 shows the simulated responses of the tunable filter. The down and up-state center frequencies are 5.12 GHz and 5.78 GHz, respectively, and their corresponding losses are 2.3 dB for both states. Each state has a transmission zero close to the other frequency band and the down and up-state transmission zero frequencies are 5.63 GHz and 5.40 GHz, respectively. With these mirrored transmission zeroes, the isolation between two pass-bands are enhanced by more than 10-dB.

The measured results are shown in Fig. 6.6, and they have about 7 dB more loss than the simulated ones. In the simulation, the resistivity of the Si substrate was assumed to be 3-10 kΩ-cm, and this substrate was not used in the fabrication. By measuring transmission line structure on the Si wafer, it is found that the Si substrate used has a 5 Ω-cm resistivity, and a simulation with 5 Ω-cm substrate also show the same 7 dB extra loss. Simulated and measured responses are given in Table 6.3.

6.2 Conclusion

A 5.1-5.8 GHz RF-MEMS CPW switchable filter was fabricated and measured on a Si substrate. The measured result of the both states have insertion loss of 9.3 dB, and the locations of the transmission zeroes are 5.40 GHz and 5.63 GHz for the up and down-state, respectively. Despite the fact that the measured losses are about 7 dB higher than simulated ones, which is due to the use of 5 Ω-cm Si substrate instead of the intended 3-10 kΩ-cm one, the idea of flipping transmission zero and its design in the CPW switchable filter are

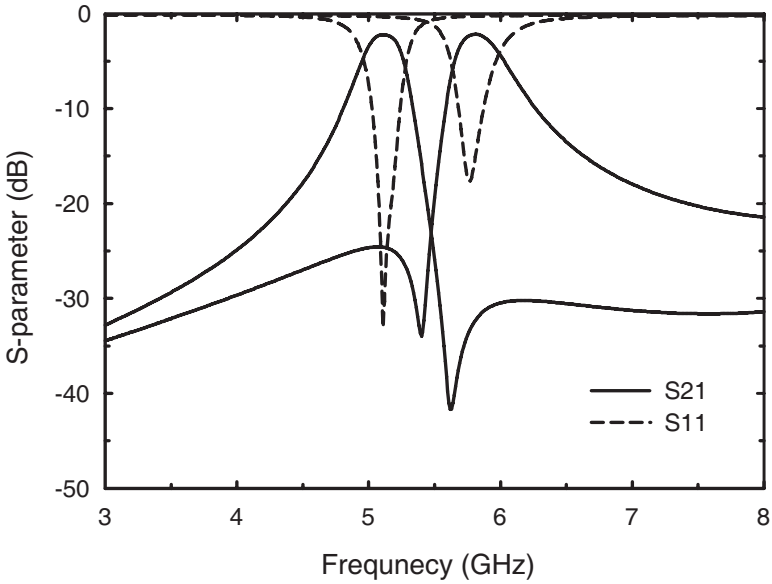

Figure 6.5: Full-wave simulation responses of the switchable filter.

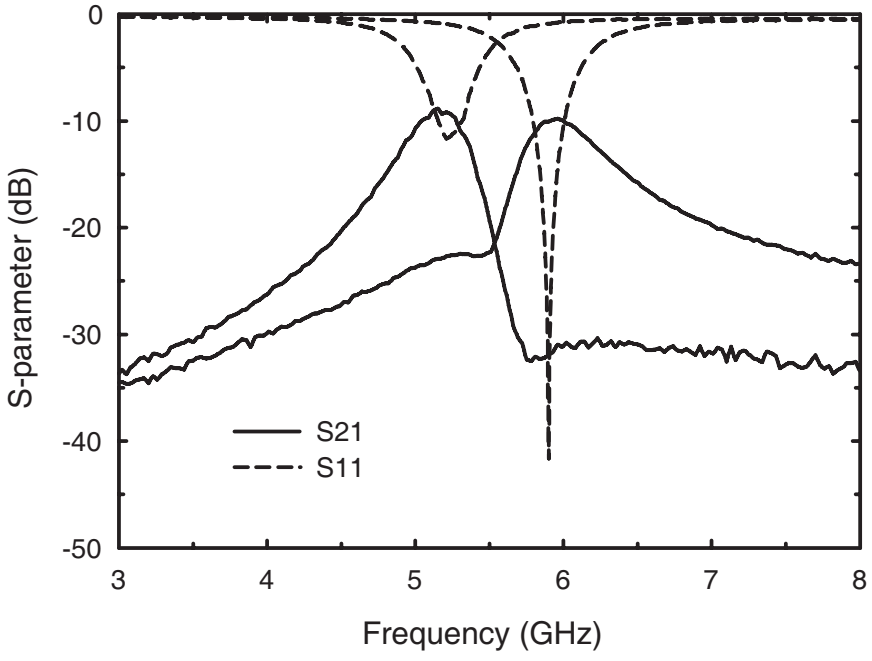

Figure 6.6: Measured responses of the switchable filter.

proven with the measurement results. With the design technique in this work, the isolation between each switched states can be improved by more than 10 dB. The isolation can be further improved when a higher order (n >3) filter is designed.

Chapter 7

Very High-Q Tunable Evanescent-Mode Cavity Filter with Low-Loss RF-MEMS Switch Network

7.1 Introduction

In modern multi-band and multi-mode devices, tunable filters are indispensable parts with immense importance due to their ability to cover different communication standards with a single device. Tunable filters could replace the use of a switched-filter bank with a single component, and therefore, reduce system size and complexity to a great extent. Low-loss tunable filters in this frequency agile system are essential, however, to our knowledge tunable filters with $Q > 200$ have not yet been reported at 2-10 GHz.

To realize a tunable filter with a $Q_u > 500$ at 2-10 GHz, both the resonator and tunable device must have a $Q_u > 500$. The resonator Q using planar technology is 100-250 depending on the substrate loss. The Q can be increased to 500 using a suspended stripline configuration, but this requires a mechanical structure as a substrate support and two ground planes, which occupies a substantial volume. Standard (full size) cavity resonators can also be used in tunable filters for the best Q ($> 5{,}000$), but their large volume at 2-10 GHz and incompatibility with fabricated tuning devices limit their usefulness for wireless systems.

The volume of cavity resonators can be significantly reduced when the evanescent mode is used. The inductive evanescent mode with a capacitive post in the cavity creates a resonance at a much lower frequency than the resonance frequency of the original cavity, thus reducing the cavity volume considerably [52]. Evanescent-mode cavity resonators have Q_u in the range of 2,000-5,000 and have been extensively used in industry [53, 54].

In this work, the evanescent-mode cavity is utilized as a high-Q resonator and a novel

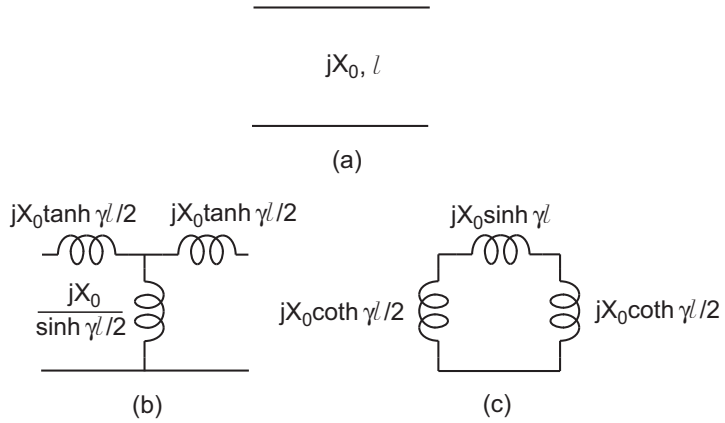

Figure 7.1: Evanescent mode waveguide (a) and its T (b) and Π equivalent lumped circuit models.

high-Q cantilever-switch capacitance network is introduced as a tuning network as a tuning network. The coupling effects between the cavity electric field and the bias-lines are significantly reduced with the use of metal-bridge cover. Also, RC circuits on the bias-path are used to minimize the energy loss throughout the biasing channel. The measured results with $fixed$ interdigital capacitance chips show the Q_u of 535-845 at 4.2-6.6 GHz. As of the writing of this thesis, there are no measurements on a evanescent-mode filter with a *tunable* RF-MEMS capacitance network

7.2 Design and Implementation of the Filter

7.2.1 Evanescent-Mode Waveguide

The waveguide mode in a waveguide below cutoff cannot propagate, and as a result creates a localized reactive region. The characteristic impedance of this region can be either inductive or capacitive depending on the mode inside the cavity. The characteristic impedances, Z_0, of the evanescent-modes in the waveguide are

$$Z_0 = \frac{\omega\mu}{k_z} \quad for \quad TE-mode \tag{7.1}$$

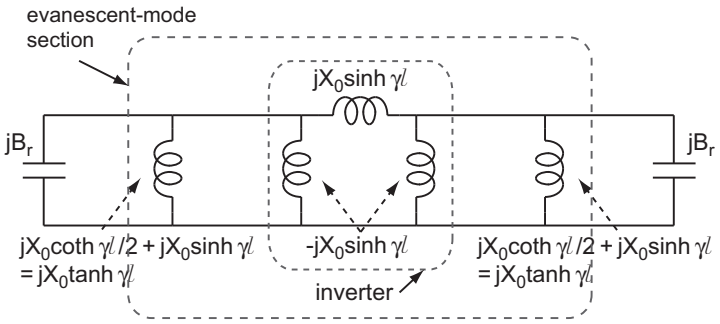

Figure 7.2: The realization of the shunt L and inverter with the evanescent-mode waveguide section.

$$Z_0 = \frac{k_z}{\omega\epsilon} \quad for \quad TM - mode \tag{7.2}$$

where

$$k_z = \sqrt{k^2 - k_c^2} = -j\gamma \tag{7.3}$$

$$\gamma = \sqrt{k_c^2 - k^2}. \tag{7.4}$$

For the TE evanescent-mode, the wave impedance becomes

$$Z_0 = jX_0 = \frac{j\eta}{\sqrt{\left(\frac{k_c}{k}\right)^2 - 1}}, \quad \eta = 377\Omega, \tag{7.5}$$

where

$$k_c = \sqrt{\left(\frac{\pi}{a}\right)^2 + \left(\frac{\pi}{b}\right)^2} \tag{7.6}$$

and (a, b) are waveguide cross-sectional dimensions.

The characteristic impedance of the TE evanescent-mode is inductive and this is equivalent to either a T or a Π circuit model (Fig. 7.1). As is well know, these inductances can be utilized as a coupling and loading element in a filter circuit. For example, a filter circuit can be designed using either the T or Π equivalent circuit in Fig. 7.1 with the proper amount of series (Fig. 7.1 (b)) or shunt (Fig. 7.1 (c)) capacitances. It is usually easier to realize a shunt capacitance than a series one in a waveguide, and a possible filter circuit

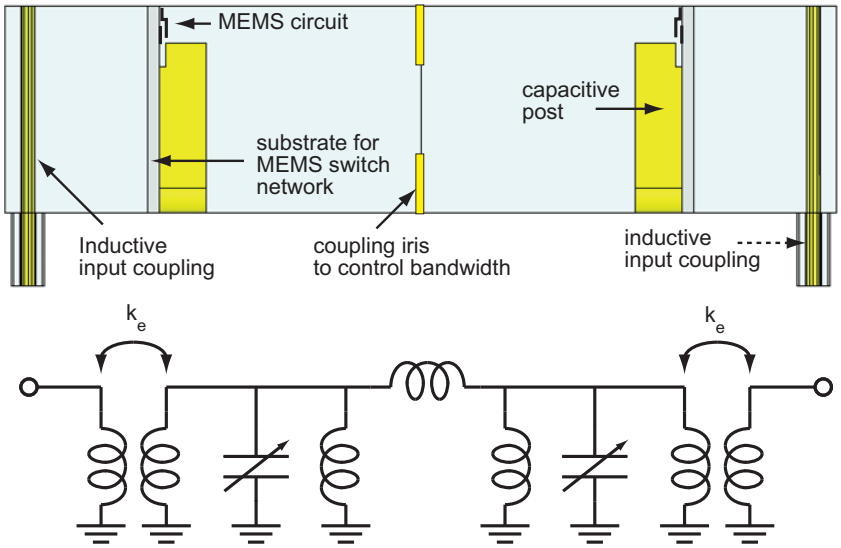

Figure 7.3: Evanescent mode cavity filter concept.

with shunt capacitances is shown in Fig. 7.2. Using the resonance condition, the required shunt capacitance values can be found by

$$\omega_0 C_r = B_r = \frac{1}{X_0} \coth \gamma l. \tag{7.7}$$

7.2.2 Extracting C_L, Q_e, and k_c of the Filter

A conceptual evanescent-mode waveguide tunable filter with external coupling and its equivalent circuit model is shown in Fig. 7.3. The shunt capacitances are implement with capacitive posts in the waveguide, and a substrate with an RF-MEMS tunable switch network is mounted on each side of the posts to tune the resonance frequency. An inductive loop coupling scheme is utilized as an external coupling circuit due to its matching characteristics over a wide frequency range.

The filter circuit in Fig. 7.3 can be simplified to the model in Fig. 7.4 due to symmetry, and the PEC/PMC (Perfect-Electric-Conductor/Perfect-Magnetic-Conductor) boundaries represent the even and odd-mode resonances of the waveguide cavity. The even and odd-mode resonance frequencies (f_e/f_o), Q_u, k_e, and Q_e can be extracted from this model using

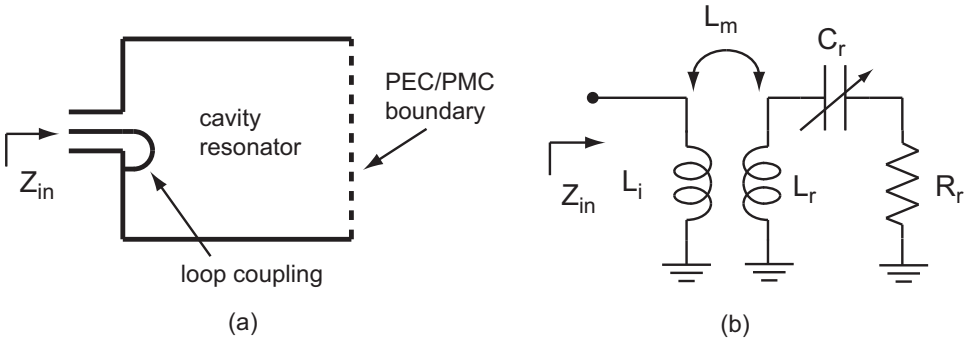

Figure 7.4: The evanescent-mode cavity resonator with inductive loop coupling (a) and its equivalent circuit model (b). L_i is a parasitic inductance of the coupling loop, and L_m is the coupling inductance.

the reflection coefficients [3]. The input impedance of the cavity resonator is

$$Z_{in} = j\omega L_i + \frac{R_i}{1 + jQ_u\left(\frac{\omega}{\omega_0} - \frac{\omega_0}{\omega}\right)}, \tag{7.8}$$

where

$$\omega_0 = \frac{1}{\sqrt{L_r C_r}}, \quad Q_u = \frac{\omega_0 L_r}{R_r}, \quad R_i = \frac{(\omega L_m)^2}{R_r}. \tag{7.9}$$

The complex input reflection coefficient, Γ_i, is plotted in Fig. 7.5. The loaded resonance frequency, ω_L, is the frequency where the magnitude of the Γ_i has its minimum. If the coupling coefficient diminishes to zero, the input reflection coefficient becomes Γ_D. The vector Γ_i-Γ_D creates a circle on the Smith chart, and is given by [55]

$$\Gamma_i - \Gamma_D = \frac{2e^{-j2tan^{-1}x_1}}{(1 + 1/k_e)(1 + j2Q_L\delta_L)}, \tag{7.10}$$

where

$$x_1 = \frac{\omega L_i}{Z_0}, \quad k_e = \frac{R_i}{Z_0(1 + x_1^2)}, \tag{7.11}$$

$$Q_L = \frac{Q_u}{1 + k_e}, \quad \delta_L = \frac{\omega - \omega_L}{\omega_0}. \tag{7.12}$$

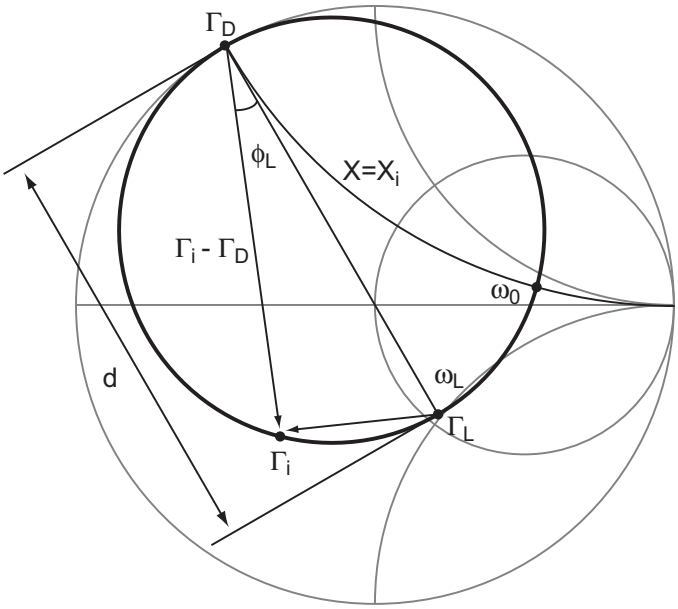

Figure 7.5: The input reflection coefficient variation of the resonator (Fig. 7.4) with frequency

When ω=ω_L, the magnitude of the vector specified in (7.10) has its maximum:

$$|\Gamma_i - \Gamma_D|_{max} = d = \frac{2}{1 + 1/k_e}. \tag{7.13}$$

The coupling coefficient is then

$$k_e = \frac{d}{2 - d}. \tag{7.14}$$

If two frequencies, f_3 and f_4 are selected to have ϕ_L=+45° and -45°, respectively, the Q_L value form (7.10) is

$$Q_L = \frac{f_0}{f_3 - f_4} \approx \frac{f_L}{f_3 - f_4}. \tag{7.15}$$

The unloaded resonator Q_u and external coupling, Q_e are then

$$Q_u = Q_L(1 + k_e), \tag{7.16}$$

$$Q_e = \frac{Q_u}{k_e}. \tag{7.17}$$

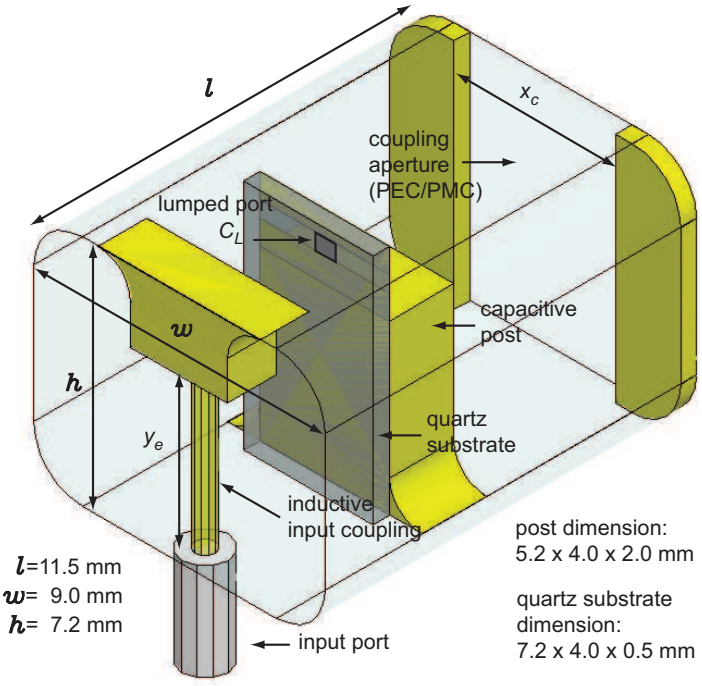

Figure 7.6: Full-wave simulation model of the evanescent-mode cavity resonator with loop coupling.

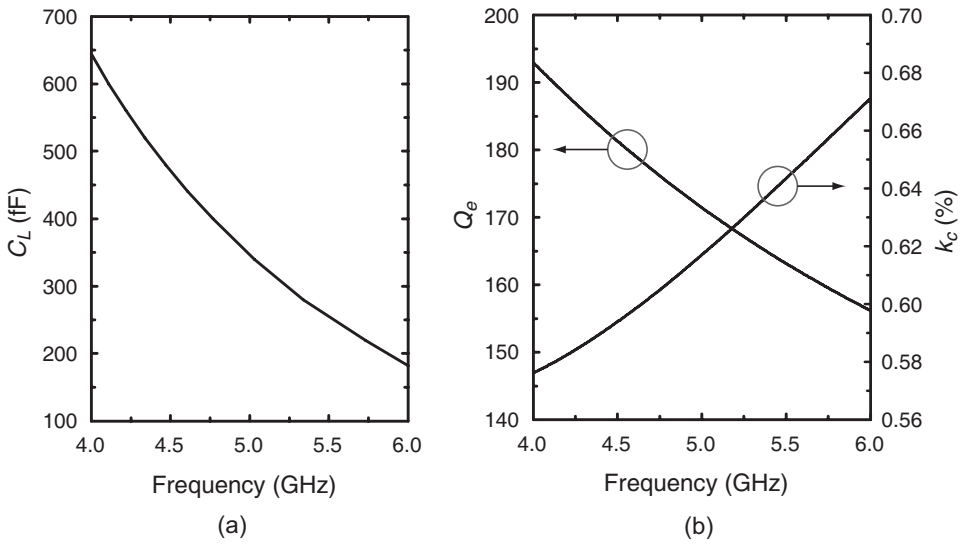

Figure 7.7: The extracted C_L (a), Q_e, and k_c (b) with the resonance frequency change (y_e=5 mm, x_c=2.5 mm). The calculations are done at 5 GHz with the cavity in Fig. 7.6.

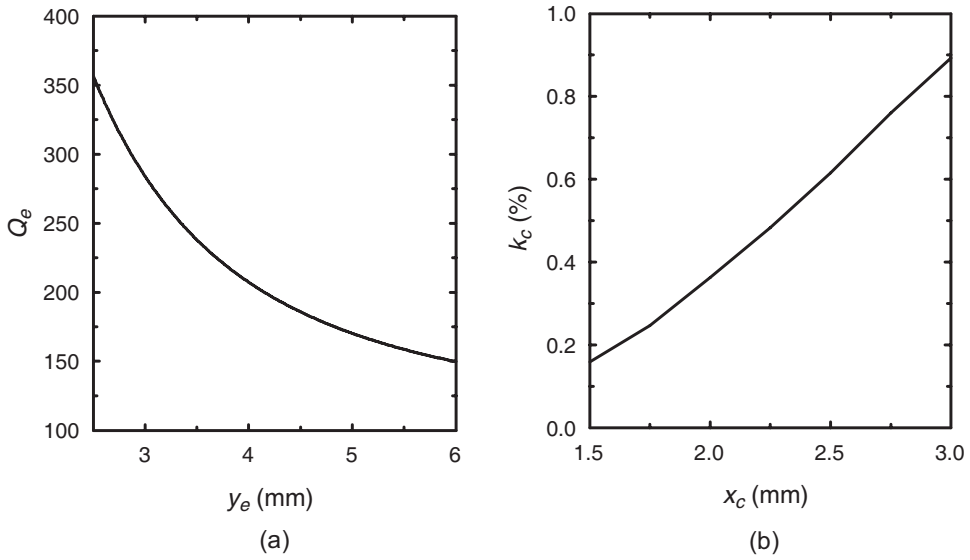

Figure 7.8: The extracted Q_e (x_c=2.5 mm) (a) and k_c (y_e=5 mm) for the cavity resonator in Fig. 7.6 with different y_e and x_c, respectively. The calculations are done at 5 GHz with the cavity in Fig. 7.6.

The full-wave simulation model for the evanescent-mode cavity resonator was built (Fig. 7.6) and HFSS simulations were performed to extract f_e, f_o, Q_e, Q_L, and C_L. A lumped-port is placed between the cavity wall and the post to include C_L in the simulation in addition to a wave-port at the coaxial input. The coupling coefficient of the filter, k_c, is calculated using the pole-splitting method, and is given by

$$k_c = \frac{f_e^2 - f_o^2}{f_e^2 + f_o^2}. \tag{7.18}$$

The extracted C_L, Q_e, and k_c values are plotted versus resonance frequency in Fig. 7.7. C_L values of 640 fF and 180 fF give a resonance frequencies of 4.0 GHz and 6.0 GHz, respectively, and Q_e and k_c values of 170±23 and 0.0062±0.0005, respectively. The frequency dependence in k_c shows a constant fractional-bandwidth behavior (23-40 MHz 3-dB bandwidth at 4-6 GHz), and the filter maintains a good matching over the frequency range due to the decrease in Q_e.

The external coupling of the resonator is controlled by the area between the cavity wall and the coaxial pin, and by changing y_e, the external coupling, k_e, can be adjusted. The symmetry plane of the filter in the resonator is set to PEC or PMC to obtain even or odd-

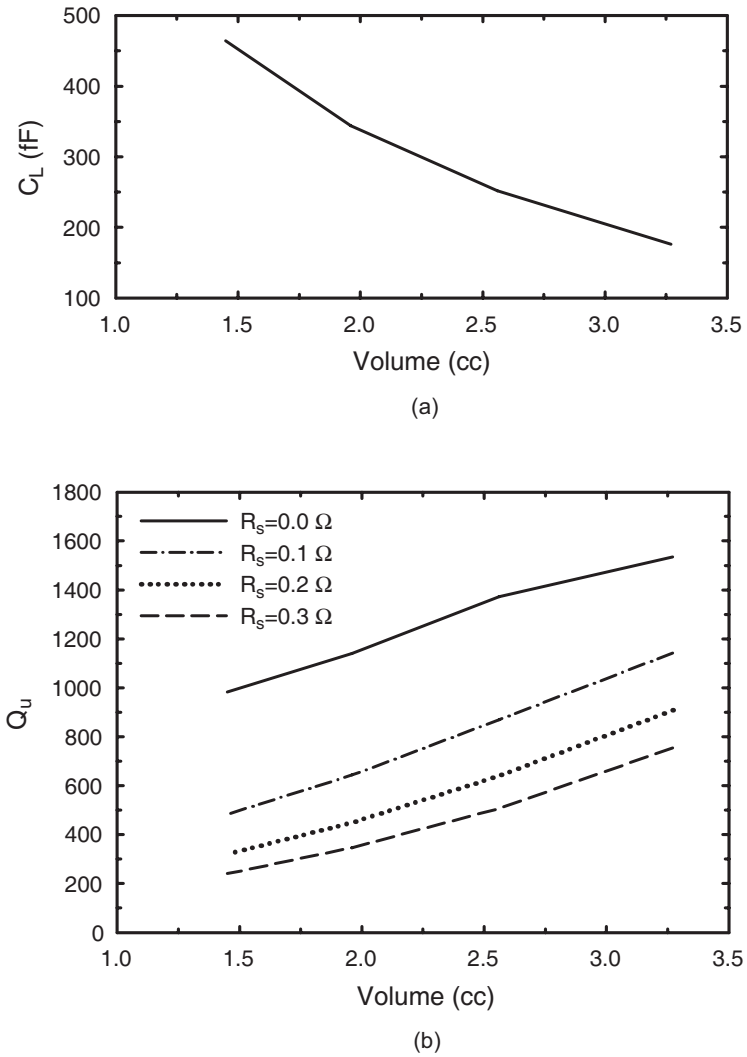

Figure 7.9: The loading capacitance, C_L, (a) and unloaded Q (b) with the volume of the cavity. R_s is the series resistance of the loading capacitor, C_L.

mode resonance frequency. The extracted Q_e and k_c values versus y_e and x_e are plotted in Fig. 7.8.

7.2.3 High-Q RF-MEMS Cantilever-Switch Capacitance Network and The Filter Implementation

A narrow-band filter design requires an estimation of the resonator Q to predict the filter insertion loss, and it is convenient to use a closed form expression relating the fractional bandwidth, Δ, unloaded Q, Q_u, and the insertion loss, L_A. With a given Δ and Q_u, L_A is

[7]

$$L_A = 4.343 \sum_{i=1}^{n} \frac{g_i}{\Delta Q_{ui}} \tag{7.19}$$

where g_i is the low-pass prototype element value.

It can be estimated from (7.19) that an unloaded Q of 580 (870) is needed to realize a 0.05% 2-pole butterworth filter with an insertion loss of 3.0 (2.0) dB (a butterworth is chosen since we are defining the filter bandwidth at the 3-dB level). The unloaded Q of the evanescent-mode cavity resonator is proportional to the volume to surface ratio, and can be few thousand depending on the size of the cavity. Designing such a narrow-band filter at a fixed frequency is not an issue, however the tunable filter design requires lossy tuning elements, and these loss of the tuning elements can have a significant effect on the resonator Q. Fig. 7.9 shows the Q_u change of a evanescent-mode cavity resonator with different volume and series resistance, R_s, in the tuning element, C_L (the C_L change with the volume is also given). It can be seen that the Q_u of the resonator can easily drop from 1,000 to 300-400 with only few tenths of an Ohm in R_s. It is therefore essential to build a very high-Q ($>$ 300-400) tuning circuit to realize a tunable filter with $Q_u > 400$. Until now RF-MEMS (Micro-Electro-Mechanical-Systems) is the only planar tunable technology with such a high Q.

The bias-line configuration and its effect on the resonator Q

In the tunable filter design with RF-MEMS, the tunable capacitance networks are placed where the electric field is maximum in the resonators. This high resonant electric field can easily coupled to the bias-lines and greatly degrades the resonator Q. Park *et al.* showed that the bias-line configuration can significantly affect the resonator Q, and suggested the *orthogonal* high-Q capacitance network to solve the problem (see chapter 5). In this chapter, the Q of interest was around 100-200, and the Q enhancement in the orthogonal capacitance network was enough to reach such a moderate Q. However, in the design of a filter with $Q > 400$, the power dissipations in the orthogonal bias-line configuration are not negligible and could even be dominant. In order to investigate this, several simulations were done with different and their effects on the resonator Q were investigated (Fig. 7.10). Even

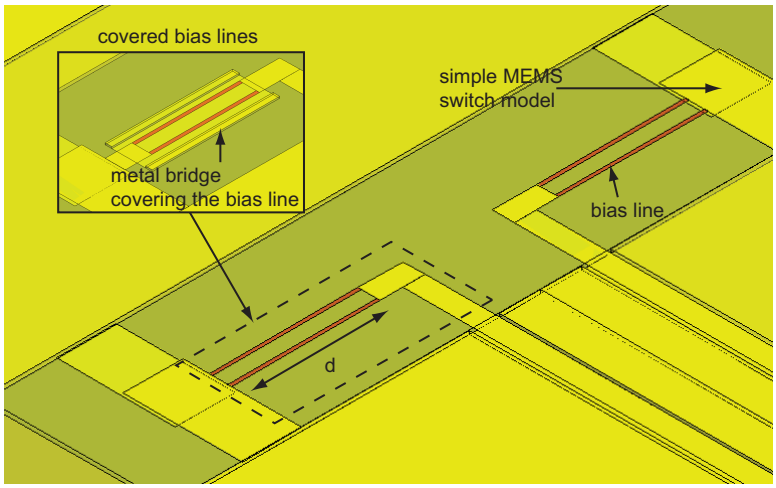

Figure 7.10: The 4-bit capacitance network model with bias-lines and simple MEMS switch models.

though all the bias-lines are configured perpendicular to the electric field in the cavity, Q_u shows a strong dependence on the bias-line resistance and its length (Fig. 7.11). The effect of the bias lines can be significantly reduced by covering them by a metal bridge. The tangential electric field diminishes to an insignificant level on the metal bridge, and therefore the electric-field coupling to the bias-lines can be substantially reduced. This is clear shown in Fig. 7.11.

The RC network on the biasing channel

The tunable capacitance network inside the cavity needs to be biased, and therefore requires a connection to the external voltage source. This means that the evanescent-mode cavity must have an opening somewhere on the cavity wall, and for this high-Q resonant cavity, it is very important to minimize radiation loss through this biasing channel. Fig. 7.12 shows the simulation model of a complete high-Q tunable capacitance network on a quartz chip (inside the evanescent-mode cavity) and its connection to the external bias-wires. The loading capacitor, C_L, is realized using 4-bit RF-MEMS cantilever-switch network and each switch has two bias-lines attached to it. The additional bias-line is for analog tuning, and this analog tuning will be discussed in the following section. To minimize the impact on the filter Q, the bias-line length is minimized and the connections between the bias-lines and

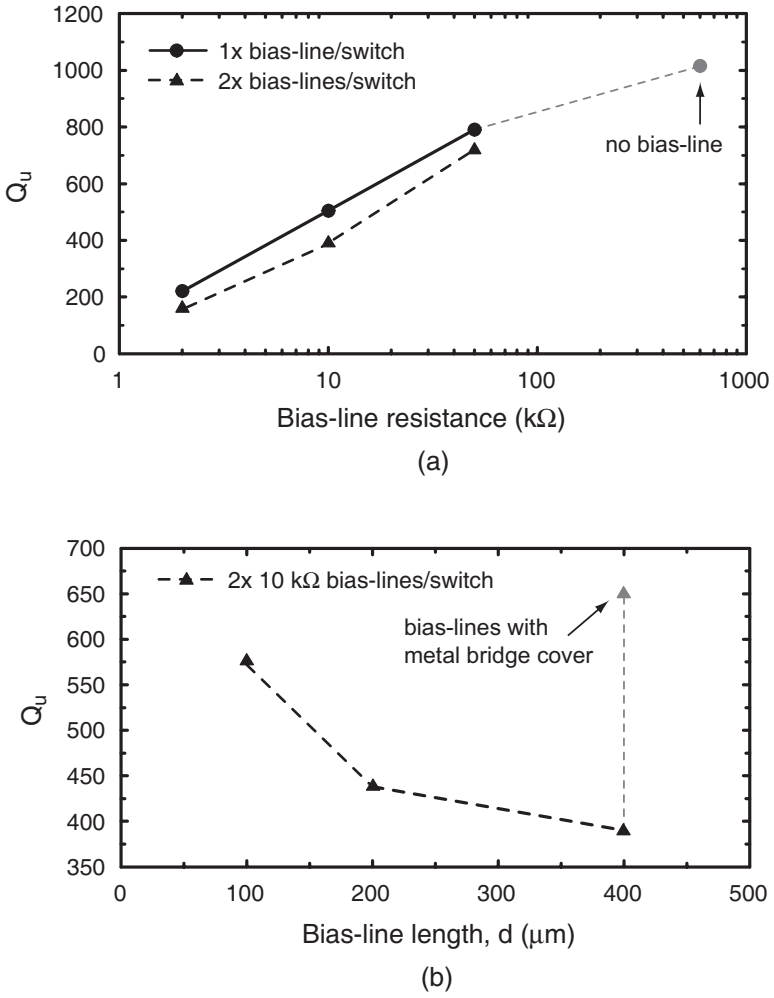

Figure 7.11: The unloaded Q of the evanescent-mode cavity resonator with the bias-line resistance (a) and the bias-line length (b). The calculations are done at 5 GHz with the cavity in Fig. 7.6.

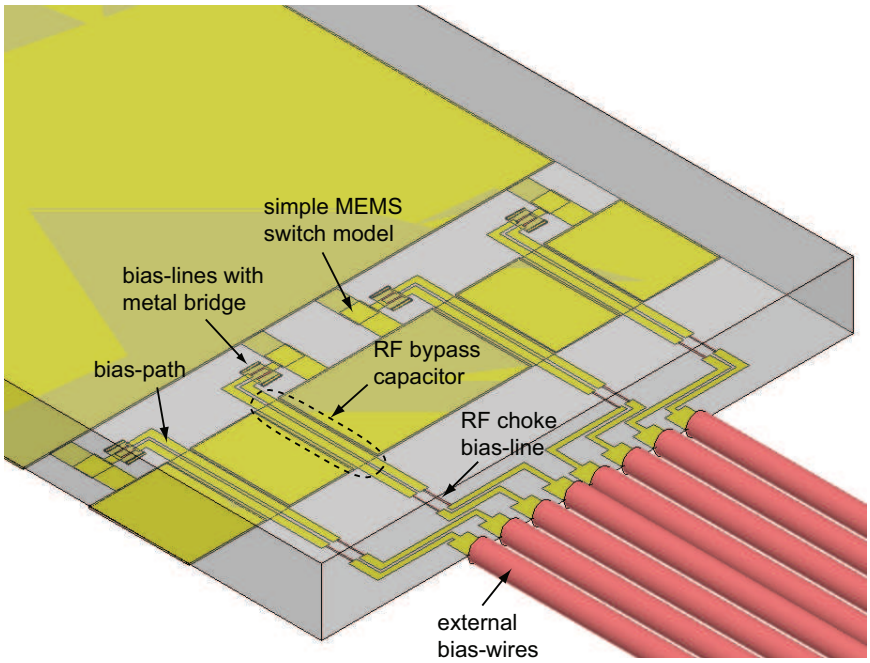

Figure 7.12: The high-Q capacitance network on a quartz substrate with RF bypass capacitors and RF block resistors.

the bias-wires are accomplished with conductive bias-paths. The bias-wires connected at end of the bias-paths go through a small channel on the cavity wall, and create a link to the external voltage source. Even though the cavity resonance frequency is far below the cutoff of the biasing channel dimension, RF energy can couple to the wires and radiate through this channel. An RC circuit is implemented in the bias-path to prevent the RF energy leakage to the bias wires. The metal bridge over the bias-path creates a shunt capacitance (C=500 fF), and the bias-line section just before the bias-wire connection pad produces a series resistance (R=200 kΩ), thus minimizing the possible RF-signal leakage through the bias wires.

The realization of the high-Q RF-MEMS cantilever-switch network and its filter implementation

For a narrow-band tunable filter, it is very important to match the resonance frequency of each resonator. Simulations with different loading capacitance values in the evanescent-mode cavity filter were performed, and their frequency responses are plotted in Fig. 7.13.

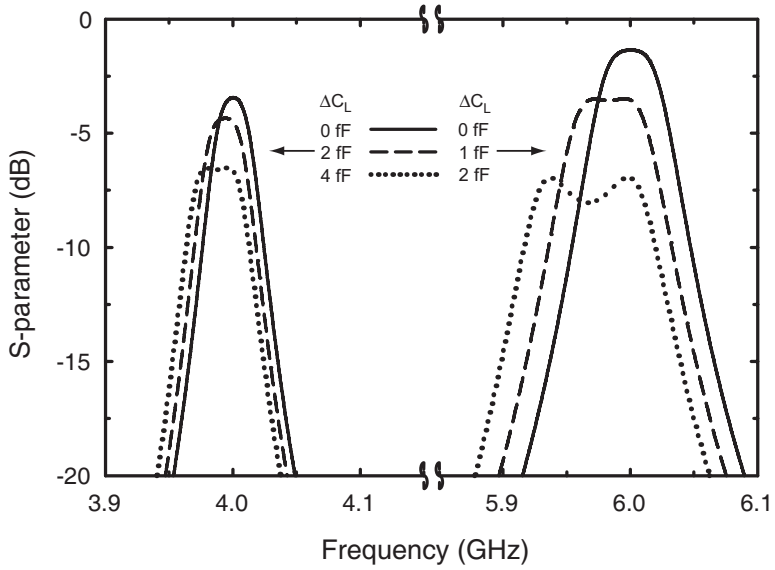

Figure 7.13: Sensitivity of the frequency responses with the different loading capacitance values in the filter. The calculations are done with the cavity in Fig. 7.6.

The simulated filter has C_L values of 322-91 fF and a 0.83-0.94 % 3-dB fractional bandwidth at 4.0-6.0 GHz. The simulation results show that at 6.0 GHz, the two loading capacitance values need to be controlled to within 1 fF, and at 4.0 GHz, 2 fF variation is the maximum allowed. This, as well as the high-Q requirement, seriously limits the design of the RF-MEMS capacitance network.

An RF-MEMS cantilever switch with an analog tuning capability (Fig. 7.14) is utilized to fulfill those requirements. The thick plated (3.5-4.0 μm) cantilever and the zipping effect with a hold-down bias voltage, V_h make this switch a good candidate for both high-Q and analog tuning capability. The measured cantilever switch has up-state and down-state capacitance of 40 fF (V_p=0 V) and 250 fF (V_p=0 V, V_h=0 V), respectively, and its analog capacitance coverage is 250-320 fF (V_p=30 V, V_h=0-12 V). The measured analog capacitance variation with different V_h is shown in Fig. 7.15 (a), and the calculated C_L value for the 4-bit capacitance network using this result is plotted in Fig. 7.15 (b). With the analog tuning capability, the 4-bit C_L network covers the capacitance range of 160-630 fF.

The chip layout of the 4-bit high-Q RF-MEMS cantilever-switch network is shown in Fig. 7.16. Each switch has a metal-air-metal scaling capacitor connected in series, and two bias-lines covered with metal bridges: one for the pull-down bias voltage, V_p, and the other

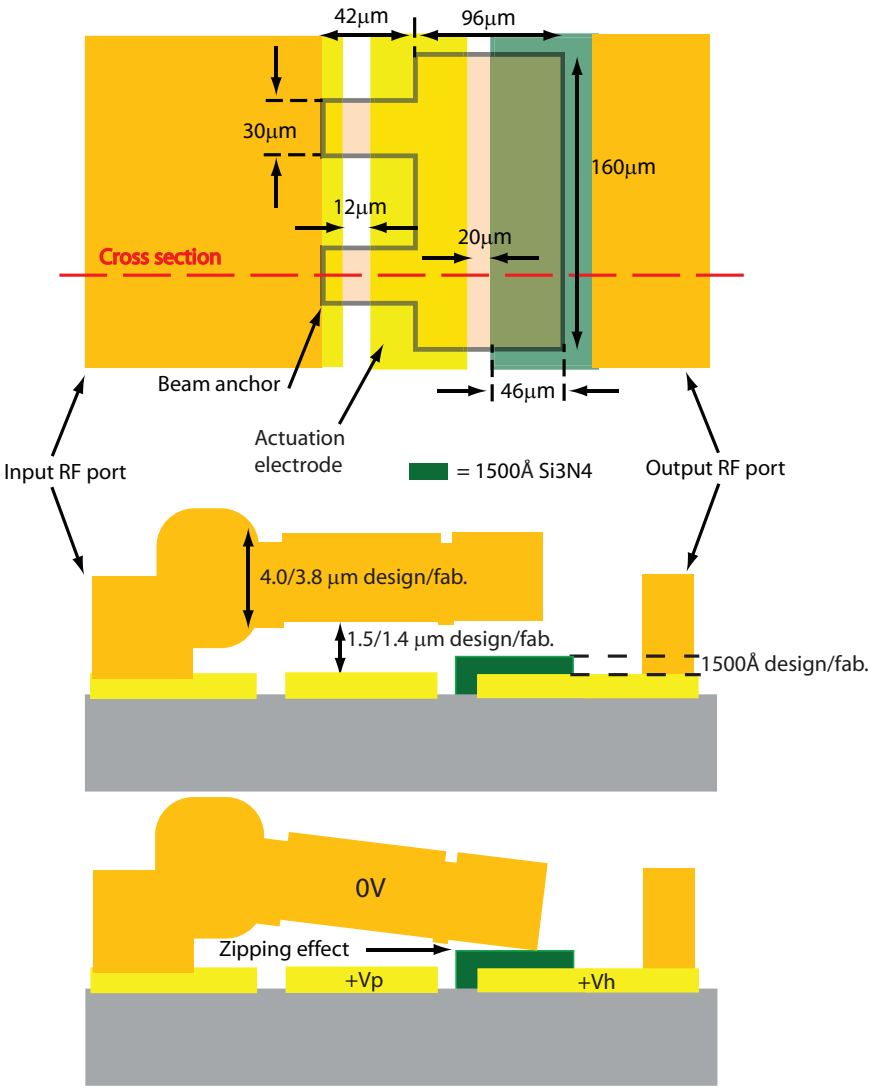

Figure 7.14: The RF-MEMS cantilever switch with analog tuning capability [5].

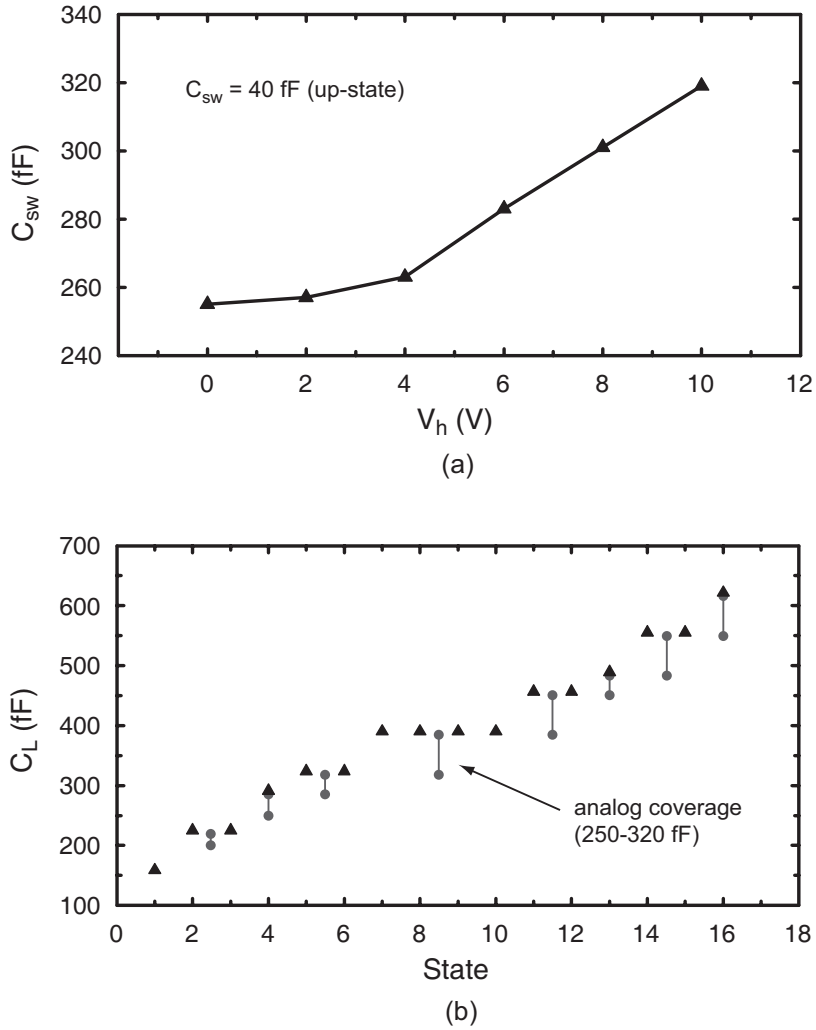

Figure 7.15: The analog coverage of the cantilever switch (a), and realized C_L values of the 4-bit capacitance network with the cantilever switch (b).

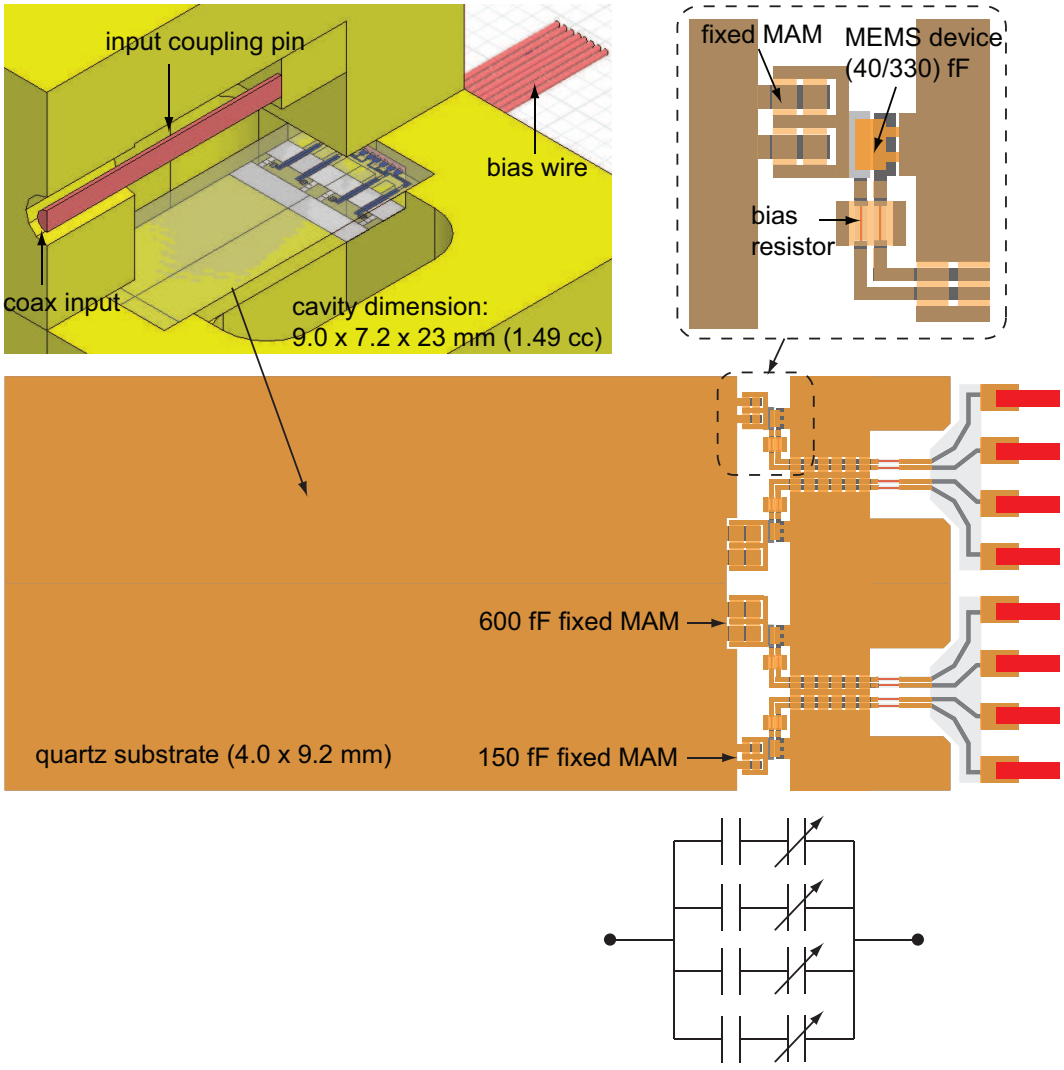

Figure 7.16: The high-Q RF-MEMS cantilever-switch capacitance network and its installation in the evanescent-mode waveguide cavity.

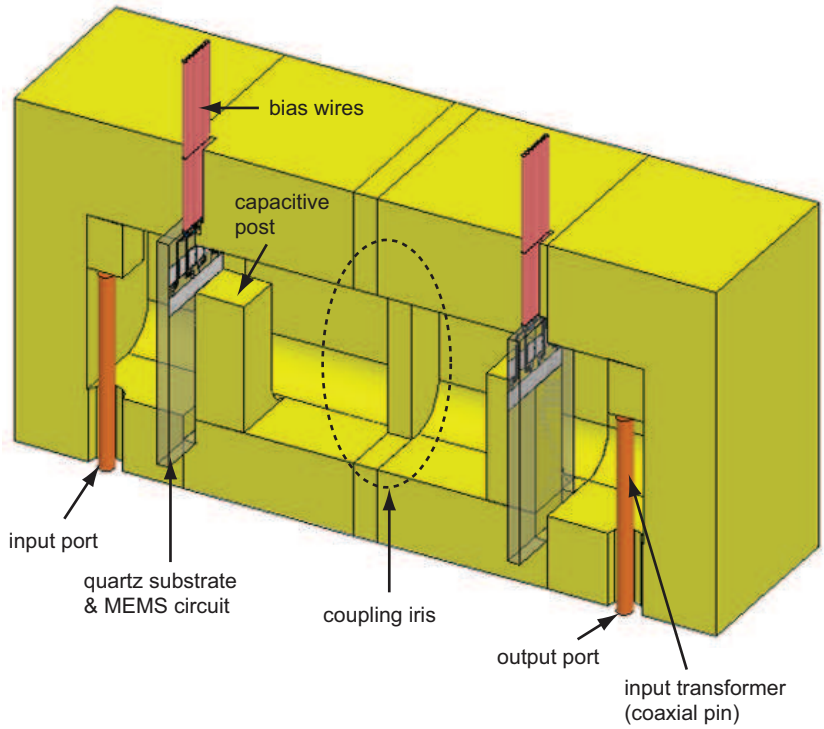

Figure 7.17: The complete model of the evanescent-mode cavity filter with the RF-MEMS chips (half view).

for the hold-down voltage, V_h.

The complete filter model with the high-Q tunable RF-MEMS chips is shown in Fig. 7.17. The chips are installed on each posts and create capacitive loadings in the resonator sections. The bias-wires attached to the RF-MEMS chip pass through the small channels in the cavity and are connected to the outside voltage source. The input couplings are realized using center pins of the coaxial connectors, and the inter-resonator coupling is controlled by the coupling iris located at the center.

7.3 Fabrication and Measurements

7.3.1 Filters With Fixed Capacitors

A 2-pole evanescent-mode waveguide filter was fabricated and its frequency response was measured. The filter is designed to have a 0.45-0.50 % bandwidth butterworth response over the 3.5-7.0 GHz range. The internal cavity volume of this filter is 3.2 cc (10.4 x 3.82 x 36.0

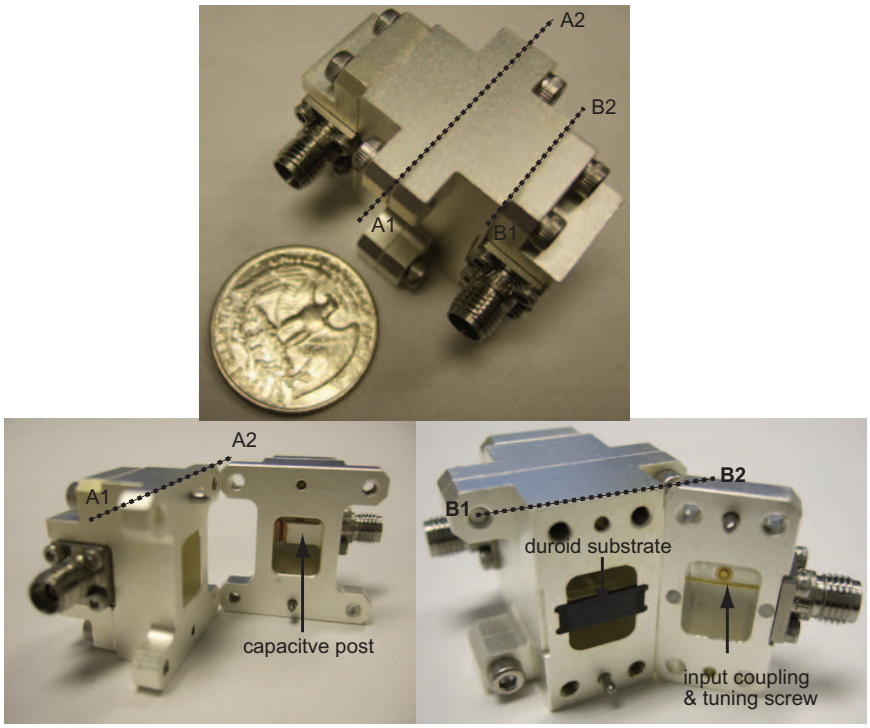

Figure 7.18: The fabricated 3cc evanescent mode cavity filter with modular assemblies.

mm^3), and the simulated Q_u is around 1,500-2,200 at 3.5-7.0 GHz. The fabricated filter and its modular assemblies are shown in Fig. 7.18. The filter is designed to have 4 sections: the input coupling section, the evanescent-mode section, and the exact mirrored copies of those two (coupling iris was not used in this design). The main reason for this modular design is for easy installation of the RF-MEMS chip, and the cut-planes are chosen so as not to disturb the current flow inside the cavity. The A1-A2 cut-plane separates the filter with two symmetrical sections. A shorting block can be mounted on this cut-plane, and this makes each symmetrical section an odd-mode resonator, and Q_u, and Q_e can be obtained directly from a measurement on this resonator section. A coupling iris block can also be inserted in this cut-plane to realize a different inter-resonator coupling. The B1-B2 cut-plane divides the resonator section into the external coupling and the evanescent-mode section, and the RF-MEMS chip is mounted on the post with this opening. The change in Q_e is also possible by using different external coupling block.

The measured frequency response of the fixed 3.2 cc evanescent-mode waveguide filter is shown in Fig. 7.19. The measured center is 6.89 GHz, and the insertion loss and 3-dB

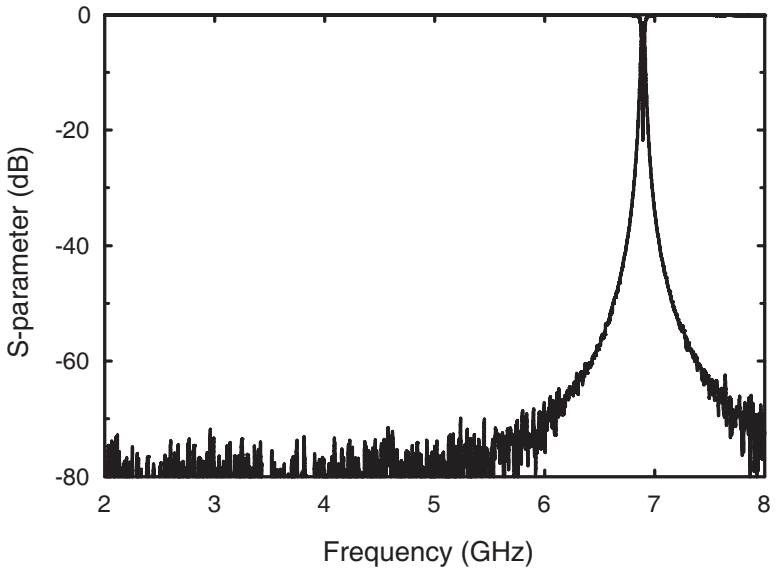

Figure 7.19: Measured 3cc evanescent mode cavity filter.

Table 7.1: The measured tuned states for the 3 cc evanescent-mode tunable filter.

f_0 (GHz)	3.45	4.37	5.36	6.13	6.99
I.L. (dB)	3.4	3.1	2.5	2.2	2.4
3-dB BW (%)	0.35	0.39	0.41	0.41	0.41
3-dB BW (MHz)	12	17	22	25	29
Q_u	1040	1020	1200	1380	1240

bandwidth are 1.35 dB and 30 MHz (0.44 %), respectively. The measured Q_u is 2050. For this measurement, no substrate was used and the loading capacitance was achieved using a small tuning screw above the post.

To examine the response versus frequency, larger tuning screws were inserted at the wall above the cavity post, and measurement was performed by Rockwell Collins International [56]. The measured frequency response is shown in Fig. 7.20, and their results are summarized in Table 7.1. The measured results show a tuning over an octave bandwidth in 3.5-7.0 GHz frequency range. The measured insertion loss and 3-dB bandwidth are 3.4-3.3 dB and 12-29 MHz, respectively. The matching of the filter is $>$ 11 dB over the tuning range, and the estimated Q_u is 1040-1380.

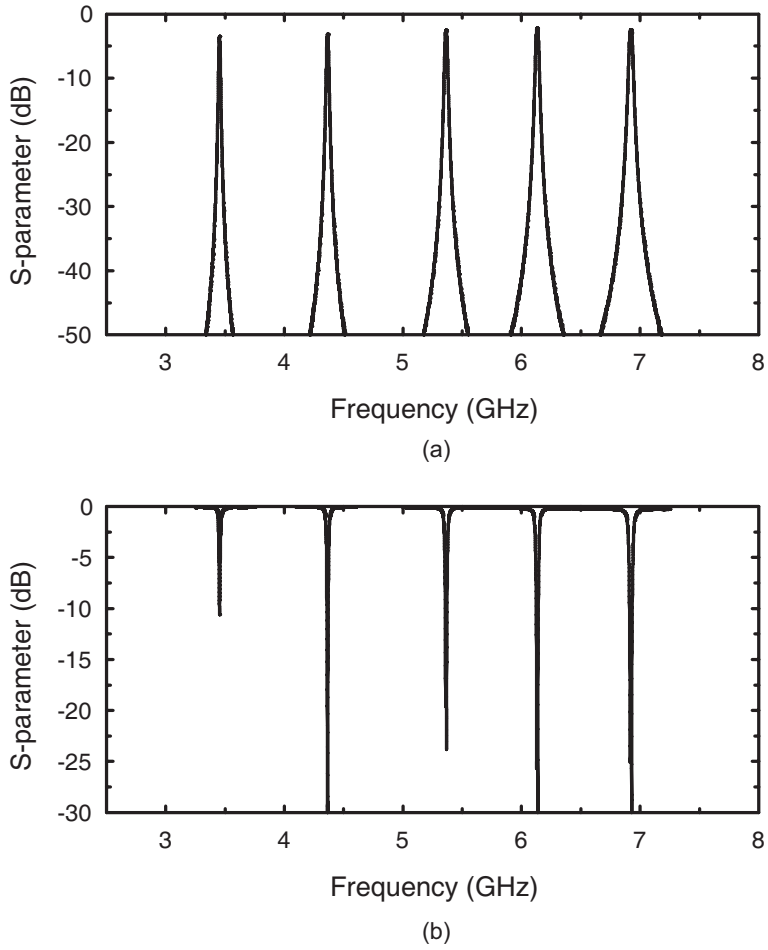

Figure 7.20: The measured S-parameters of the 3 cc evanescent-mode tunable filter (mechanical tuning).

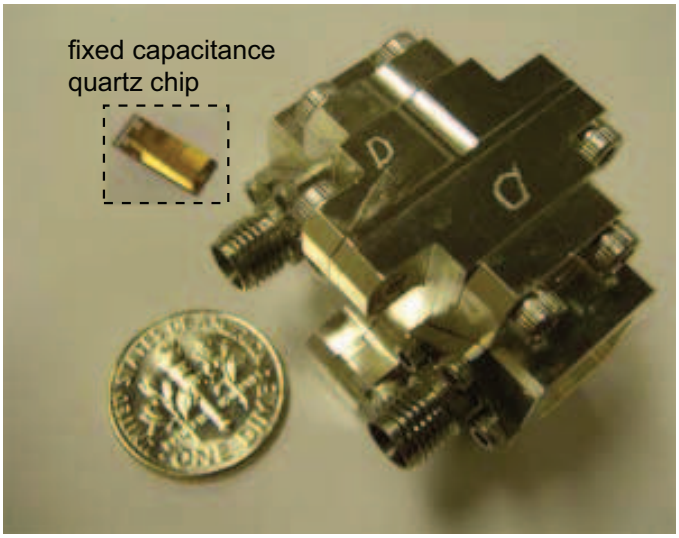

Figure 7.21: The fabricated 1.5 cc evanescent mode filter with the interdigital capacitor on quartz substrate.

7.3.2 Filters With Very High-Q Tunable RF-MEMS Cantilever-Switch Capacitor Network

An evanescent-mode cavity filter with a 1.5 cc (9.0 x 7.2 x 23.0 mm) volume and interdigital-capacitor quartz chips with different fixed capacitance values was fabricated (Fig. 7.22. The interdigital-capacitor quartz chip has the same bottom layer configuration as the RF-MEMS chip except that the cantilever switches are replaced with an interdigital capacitor. Three different quartz chips were installed in the evanescent-mode cavity, and the frequency responses were measured (Fig. 7.22, Table. 7.2. The measured filter frequencies done on several prototypes are 4.19 GHz, 5.36 GHz, and 6.59 GHz, and the corresponding capacitance values of the interdigital-capacitor chips are 570 fF, 280 fF, and 80 fF, respectively.

The high-Q tunable RF-MEMS cantilever-switch network chips are being fabricated, and the tunable filter responses with these chips will be measured soon.

7.4 Conclusion

Evanescent-mode cavity filters with very high-Q were designed, fabricated and measured. The design of the evanescent-mode cavity resonator as a filter network and its design pa-

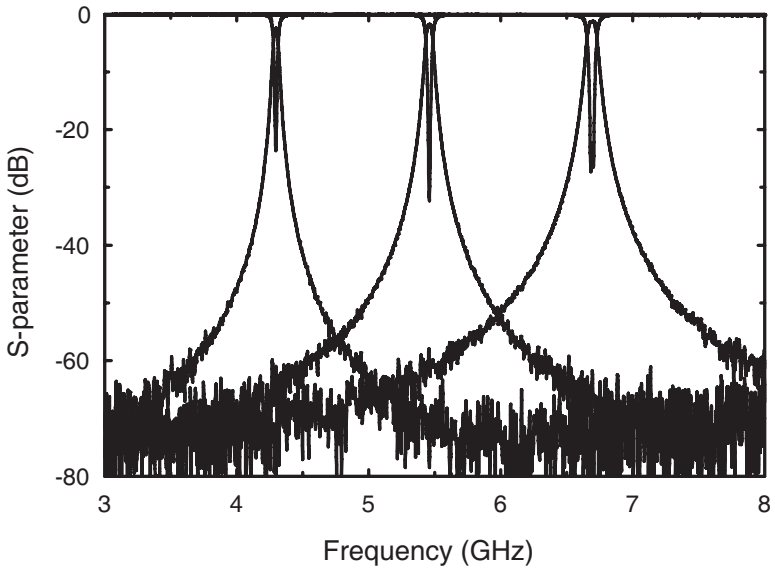

Figure 7.22: Measured 1.5 cc evanescent mode filter with three different interdigital-capacitor chips.

Table 7.2: Measured states of the 1.5 cc evanescent-mode filter with different capacitance chips.

f_0 (GHz)	4.19	5.36	6.59
I.L. (dB)	2.46	1.81	1.28
3-dB BW (%)	0.93	1.01	1.14
3-dB BW (MHz)	39	54	75
Q_u	535	675	845

rameter extractions were discussed. The loss mechanisms in the tunable filter realization were investigated, and a very high-Q RF-MEMS cantilever switch network is proposed.

The 3.2 cc evanescent-mode filter with mechanical tuner has an octave of tuning range(3.5-7.0 GHz) with a Q_u of 1040-1380. The reduced-volume 1.5 cc evanescent-mode cavity filter with different interdigital-capacitor chips was measured, and its measured filter frequency and Q_u are 4.19-6.59 GHz and 535-845, respectively. The tunable very high-Q RF-MEMS capacitance network chips are being fabricated and will be measured soon.

Chapter 8

Conclusion and Future Work

8.1 Summary of Work

This thesis presented a new admittance matrix distributed filter design method and novel high-Q RF-MEMS tunable filters. A 2.1 GHz miniature filter with independent electric and magnetic coupling was designed using this admittance matrix method. The conventional filter design method has difficulties in analyzing a complex shape hybrid coupling filter, and the admittance matrix design method takes all the intricate geometry into account making the filter design quite straightforward. A significant size reduction (6.6×4.6 mm^2) is accomplished on ϵ_r=10.2 Duroid substrate, and the measured filter shows the loss and unloaded Q of 1.4 dB and 150, respectively.

With the unique independent electric and magnetic coupling schemes in this miniature filter design, three tunable (Schottky varactor diodes) filters with constant fractional-bandwidth, decreasing fractional-bandwidth (absolute constant-bandwidth), and increasing fractional-bandwidth were built with a tuning range of ∼850 MHz to ∼1400 MHz. The constant fraction-bandwidth filter has a 1-dB bandwidth of 5.4 ± 0.3 % and an insertion loss of 2.88-1.04 dB. The decreasing fractional-bandwidth filter shows a 1-dB bandwidth decrease from 5.2 % to 2.9 % with an insertion loss of 2.89-1.93 dB (this is effectively an 40-45 MHz constant absolute-bandwidth filter). The increasing fractional-bandwidth filter shows a 1-dB bandwidth increase from 4.3 % to 6.5 % with an insertion loss of 3.47-1.18 dB. The measured Q of the filters are between 53 and 152 from ∼850 MHz to ∼ 1400 MHz. The measured IIP3 ranges from 11.3 dBm to 20.1 dBm depending on the bias voltage. To our knowledge, these planar tunable filters represent state-of-the art insertion loss performance at this frequency range.

In the 4-6 GHz 3-bit RF-MEMS tunable filter work, a detailed distributed admittance matrix design method for the capacitively-loaded coupled $\lambda/2$ resonators is presented. Source-load impedances are first included in the design equation, and a filter design including arbitrary loss becomes possible with this impedance loading design method. The lossy electric-field to bias-line coupling mechanisms were first addressed and the orthogonal high-Q capacitance network was introduced to minimize the coupling. Measurements show an unloaded-Q of 85-170, an insertion loss of 1.5-2.8 dB, and a 1-dB bandwidth of 4.35 $\pm$ 0.35% at 4-6 GHz. The measured IIP3 and 1-dB power compression point at 5.91 GHz are $>$ 40 dBm and 27.5 dBm, respectively. The unloaded Q can be improved to 125-210 with the use of a thicker bottom electrode. To our knowledge, this is the highest Q tunable planar filter to-date at this frequency range.

Finally, a very high-Q RF-MEMS tunable filter design using a cavity resonator is discussed. The evanescent-mode cavity resonator is introduced to realize a resonator $Q \sim$ 1000, and the filter design and its full-wave implementation are presented. A high-Q RF-MEMS cantilever-switch capacitance network is designed as a chip to realize a frequency tuning circuit in the cavity. The lossy interaction between the high resonant electric field and the bias-lines in the cavity is further investigated, and the bridge $bias-linecover$ is introduced. The energy loss throughout the bias-channel is also minimized using RC networks in the bias-path, and a novel modular assembly of the cavity is introduced to ease the installation of the chip and coupling coefficient alteration. With all these novel techniques, a dramatic reduction in the loss of the tunable RF-MEMS capacitance network is accomplished. The measured results of the evanescent-mode cavity filter with several fixed interdigital-capacitance chips show a center frequency of 4.19-6.59 GHz, an insertion loss of 2.46-1.28 dB, and a Q of 538-845, respectively. No tunable data was obtained at the time of this thesis.

8.2 Future Work

For the 4-6 GHz RF-MEMS tunable filter in chapter 4, the realized unloaded Q was 85-170. The resonator Q can be increased to 150-250 with the use of a thicker bottom electrode

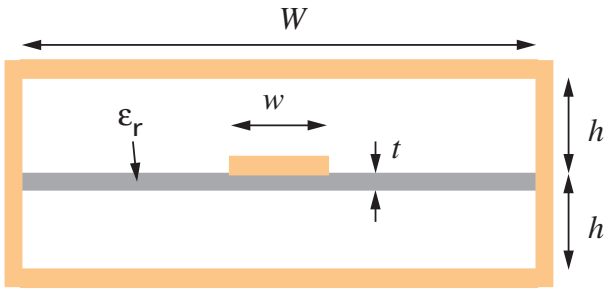

Figure 8.1: The cross sectional view of the suspended strip transmission line.

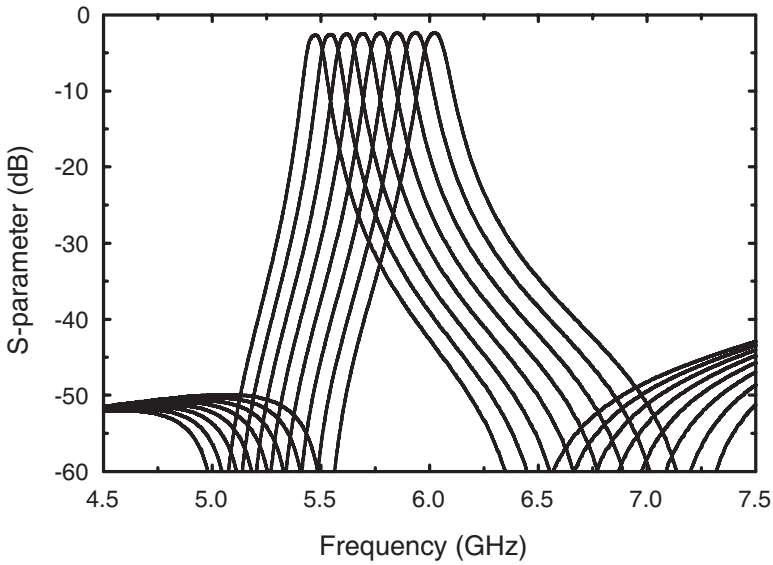

Figure 8.2: Simulated responses of the 5.4-6.0 GHz suspended strip-line tunable filter. The simulated 3-dB bandwidth, insertion loss, and Q_u at 5.4-6.0 GHz are 82-97 MHz, 2.7-2.3 dB, and 320-510, respectively

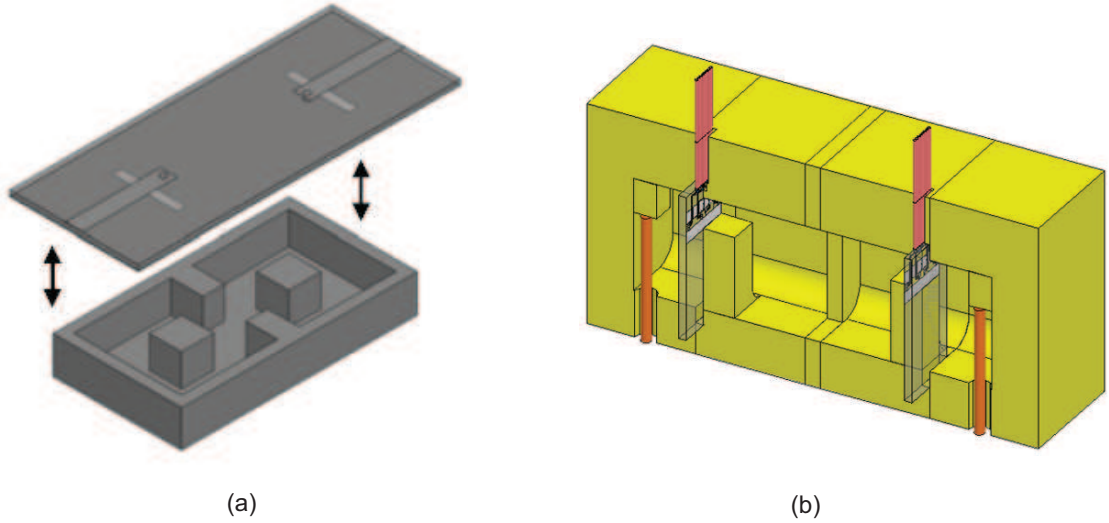

Figure 8.3: The very high-Q loaded-cavity [6] (a) and evanescent-mode cavity (b) tunable filters.

in the capacitance network, and this is nearly the limit of the achievable tunable Q using planar technologies at 3-6 GHz. A suspended strip-line resonator (Fig. 8.1) can be used to further enhance the resonator Q up to 600, however, the Q of the MEMS capacitance tuning network can be a limiting factor unless the Q of the tuning network is compatible with the Q of the suspended strip-line resonator. A tunable filter with the suspended strip-line resonator is designed and the simulation results are shown in Fig. 8.2 (the MEMS capacitance Q is 400 including bias-line loss). The bias-lines must also be designed in an orthogonal fashion and have a resistivity > 10 kΩ/sq so as not to contribute any additional loss and maintain a very high device Q.

Realizing a tunable $Q > 500$ is not possible even with the suspended strip implementation, and this is only feasible with a very high-Q resonator such as a cavity resonator. The cavity resonator usually has a Q of 5,000-20,000, and for the size reduction, evanescent-mode resonator ($Q \sim$ 2,000-4,000) can also be used. The research areas in 3-dimensional realizations of the tunable filters (Fig. 8.3) are still wide-open, and active investigations are required along with the enhancement of the tunable network Q inside the cavity.

Bibliography

[1] G. M. Rebeiz, *RF MEMS Theory, Design, and Technology.* New York, USA: Wiley, 2003.

[2] Sirific Wireless Incorporation, Richardson, TX USA.

[3] S. Duffy, C. Bozler, S. Rabe, J. Knecht, L. Travis, P. Wyatt, C. Keast, and M. Gouker, "MEMS microswitches for reconfigurable microwave circuitry," *IEEE Microw. Wireless Compon. Lett.*, vol. 11, no. 3, pp. 106–108, Mar. 2001.

[4] P. M. Zavracky, N. E. McGruer, R. H. Morrison, and D. Potter, "Microswitches and microrelays with a view toward microwave applications," *Int. J. RF Microwave CAE*, vol. 9, no. 4, pp. 338–347, July 1999.

[5] A. Grichener, B. Lakshminarayanan, and G. M. Rebeiz, "High-Q RF MEMS capacitor with digital/analog tuning capabilities," *IEEE MTT-S Int. Microwave Symp. Dig.*, June 2008.

[6] H. Joshi, H. H. Sigmarsson, D. Peroulis, and W. J. Chappell, "Highly loaded evanescent cavities for widely tunable high-Q filters," in *IEEE MTT-S Int. Microwave Symp. Dig.*, Honolulu, Hawaii USA, June 2007, pp. 2133–2136.

[7] G. L. Matthaei, L. Young, and E. Jones, *Microwave Filters Impedance-Matching Networks, and Coupling Structures.* Norwood, MA: Artech House, 1980.

[8] P. S. Carter, "Equivalent circuit of orthogonal-loop-coupled magnetic resonance filters and bandwidth narrowing due to coupling resonance," *IEEE Trans. Microwave Theory Tech*, vol. 18, pp. 100–105, Feb. 1970.

[9] R. F. Fjerstad, "Some design considerations and realizations of iris-coupled YIG-tuned filters in the 12-40 ghz region," *IEEE Trans. Microwave Theory Tech*, vol. 18, pp. 205–212, Apr. 1970.

[10] W. J. Keane, "YIG filters aid wide open receivers," *Microwave J.*, vol. 17, no. 8, Sept. 1980.

[11] A. Tombak, J.-P. Maria, F. T. Ayguavives, Z. Jin, G. T. Stauf, A. I. Kingon, and A. Mortazawi, "Voltage-controlled RF filters employing thin-film barium-strontium-titanate tunable capacitors," *IEEE Trans. Microwave Theory & Tech.*, vol. 51, no. 2, pp. 462–467, Feb. 2003.

[12] I. C. Hunter and J. D. Rhodes, "Electronically tunable microwave bandpass filters," *IEEE Trans. Microwave Theory & Tech.*, vol. 30, no. 9, pp. 1354–1360, Sept. 1982.

[13] B. H. Moekley and Y. Zhang, "Struntium titanate thin films for tunable $YBa_2Cu_3O_7$ microwave filters," *IEEE Trans. Appl. Superconduct.*, vol. 11, pp. 450–453, Mar. 2001.

[14] A. R. Brown and G. M. Rebeiz, "A varactor-tuned RF filter," *IEEE Trans. Microwave Theory & Tech.*, vol. 48, no. 7, pp. 1157–1160, July 2000.

[15] M. Sanchez-Renedo, R. Gomez-Garcia, J. I. Alonso, and C. Briso-Rodriguez, "Tunable combline filter with continuous control of center frequency and bandwidth," *IEEE Trans. Microwave Theory & Tech.*, vol. 53, no. 1, pp. 191–199, Jan. 2005.

[16] L. Dussopt and G. M. Rebeiz, "Intermodulation distortion and power handling in RF MEMS switches, varators, and tunable filters," *IEEE Trans. Microwave Theory & Tech.*, vol. 51, no. 4, pp. 1247–1256, Apr. 2003.

[17] J. Brank, J. Yao, M. Eberly, A. Malczewski, K. Varian, and C. L. Goldsmith, "RF MEMS-based tunable filters," *Int. J. RF Microwave CAE*, vol. 11, pp. 276–284, Sept. 2001.

[18] B. Lakshminarayanan and T. Weller, "Tunable bandpass filter using distributed MEMS transmission lines," in *IEEE MTT-S Int. Microwave Symp. Dig.*, Philadelphia, PA USA, June 2003, pp. 1789–1792.

[19] R. M. Young, J. D. Adam, C. R. Vale, T. T. Braggins, S. V. Krishnaswamy, C. E. Milton, D. W. Bever, L. G. Chorosinski, L.-S. Chen, D. E. Crockett, C. B. Freidhoff, S. H. Talisa, E. Capelle, R. Tranchini, J. R. Fende, J. M. Lorthioir, and A. R. Tories, "Low-loss bandpass RF filter using MEMS capacitance switches to achieve a one-octave tuning range and independently variable bandwidth," in *IEEE MTT-S International Microwave Symposium Digest*, Philadelphia, PA, June 2003, pp. 1781–1784.

[20] A. Abbaspour-Tamijani, L. Dussopt, and G. M. Rebeiz, "Miniature and tunable filters using MEMS capacitors," *IEEE Trans. Microwave Theory & Tech.*, vol. 51, no. 7, pp. 1878–1885, July 2003.

[21] C. D. Nordquist, A. Muyshondt, M. V. Pack, P. S. Finnegan, C. W. Dyck, I. C. Reines, G. M. Kraus, T. A. Plut, G. R. Sloan, C. L. Goldsmith, and C. T. Sullivan, "An x-band to Ku-band RF MEMS switched coplanar strip filter," *IEEE Microw. Wireless Compon. Lett.*, vol. 14, no. 9, pp. 425–427, Sept. 2004.

[22] A. Pothier, J.-C. Orlianges, G. Zheng, C. Champeaux, A. Catherinot, P. B. D. Cros, and J. Papapolymerou, "Low-loss 2-bit tunable bandpass filters using MEMS DC contact switches," *IEEE Trans. Microwave Theory & Tech.*, vol. 53, no. 1, pp. 354–360, Jan. 2005.

[23] K. Entesari and G. M. Rebeiz, "A differential 4-bit 6.5-10 GHz RF MEMS tunable filter," *IEEE Trans. Microwave Theory & Tech.*, vol. 53, no. 3, pp. 1103–1110, Mar. 2005.

[24] ——, "A 12-18 GHz three-pole RF MEMS tunable filter," *IEEE Trans. Microwave Theory & Tech.*, vol. 53, no. 8, pp. 2566–2571, Aug. 2005.

[25] B. Pillans, A. Malczewski, R. Allison, and J. Brank, "6-15 GHz RF MEMS tunable filters," in *IEEE MTT-S Int. Microwave Symp. Dig.*, Long Beach, CA USA, June 2005, pp. 919–922.

[26] J.-M. Kim, S. Lee, J.-H. Park, J.-M. Kim, C.-W. Baek, Y. Kwon, and Y.-K. Kim, "Digitally frequency-controllable dual-band WLAN filters using micromachined frequency-tuning elements," in *19th IEEE MEMS 2006 Conf.*, Istanbul, Turkey, Jan. 2006, pp. 158–161.

[27] C. L. Goldsmith, Z. Yao, S. Eshelman, and D. Denniston, "Performance of low-loss RF MEMS capacitive switches," *IEEE Microw. Guided Wave. Lett.*, vol. 11, no. 3, pp. 106–108, Mar. 2001.

[28] L. Dussopt and G. M. Rebeiz, "High-Q millimeter-wave MEMS varactors," *IEEE MTT-S Int. Microwave Symp. Dig.*, pp. 1205–1208, June 2000.

[29] M. Sagawa, M. Makimoto, and S. Yamashita, "Geometrical structures and fundamental characteristics of microwave stepped-impedance resonators," *IEEE Trans. Microwave Theory Tech.*, vol. 45, no. 7, pp. 1078–1085, Jul. 1997.

[30] T. Ishizaki, M. Fujita, H. Kagata, T. Uwano, and H. Miyaki, "Very small dielectric planar filter for portable telephones," *IEEE Trans. Microwawe Theory Tech.*, vol. 42, pp. 2017–2022, nov 1994.

[31] H. Yatsuda, T. Horishima, T. Eimura, and T. Ooiwa, "Miniaturized saw filters using a flip-chip technique," *IEEE Trans. Ultrasonics, Ferroelectrics and Frequency Control*, vol. 43, pp. 125–130, jan 1996.

[32] R. C. Ruby, P. Bradley, Y. Oshmyansky, A. Chien, and J. D. Larson, "Thin film bulk wave acoustic resonators (FBAR) for wireless applications," in *IEEE Ultrasonics Symposium*, vol. 1, Oct. 2001, pp. 813–821.

[33] *HFSS 10.1*, Ansoft, Corporation., Pittsburgh, PA USA, 2006.

[34] *MATLAB 7.1*, The Mathworks, Inc., Natick, MA USA, 2005.

[35] *Roger RT/Duroid Data Sheet*, Rogers Corporation, Chandler, AZ USA.

[36] *ATC 600S data sheet*, American Techincal Ceramics, Hungtington Station, New York USA.

[37] *Advanced Design System 2005A*, Agilent Technologies, Inc., Palo Alto, CA USA, 2005.

[38] C. J. Lugo and J. Papapolymerou, "Electronic switchable bandpass filter using PIN diodes for wireless low cost sytem-on-a-package applications," *IEE Proc.-Microw. Antennas Propag.*, vol. 151, no. 6, pp. 497–502, Dec. 2004.

[39] S.-J. Park, K.-Y. Lee, and G. M. Rebeiz, "Low-loss 5.15-5.70-GHz RF MEMS switchable filter for wireless LAN applications," *IEEE Trans. Microwave Theory & Tech.*, vol. 54, no. 11, pp. 3931–3939, Nov. 2006.

[40] S.-J. Park, K. V. Caekenberghe, and G. M. Rebeiz, "A miniature 2.1-GHz low loss microstrip filter with independent electric and magnetic coupling," *IEEE Microw. Wireless Compon. Lett.*, vol. 14, no. 10, pp. 496–498, Oct. 2004.

[41] V. K. Tripathi, "Asymmetric coupled transmission lines in an inhomogeneous medium," *IEEE Trans. Microwave Theory & Tech.*, vol. 23, no. 9, pp. 734–739, Nov. 1975.

[42] *Sonnet 10.52*, Sonnet Software, Inc., North Syracuse, NY USA, 2005.

[43] *M\A COM MA46H202 Data Sheet*, Rogers Corporation, Lowell, MA USA.

[44] *AVX Accu-P data sheet*, AVX Corporation, Myrtle Beach, SC USA.

[45] J. Nath, D. Ghosh, J.-P. Maria, A. I. Kingon, W. Fathelbab, P. D. Franzon, and M. B. Steer, "An electronically tunable microstrip bandpass filter using thin-film barium-strontium-titanate (BST) varactors," *IEEE Trans. Microwave Theory & Tech.*, vol. 53, no. 9, pp. 2707–2717, Sept. 2005.

[46] J.-S. Hong and M. J. Lancaster, "Couplings of microstrip square open-loop resonators for cross-coupled planar filter," *IEEE Trans. Microwave Theory & Tech.*, vol. 44, no. 12, pp. 2099–2109, Dec. 1996.

[47] M. Makimoto and M. Sagawa, "Varactor tuned band pass filters using microstrip-line ring resonators," in *IEEE MTT-S Int. Microwave Symp. Dig.*, Baltimore, MD USA, June 1986, pp. 411–414.

[48] I. Hunter, *Theory and Design of Microwave Filters.* London U.K.: The Institution of Electrical Engineers, 2001.

[49] J. S. Hayden and G. M. Rebeiz, "Very low loss distributed X-band and Ka-band mems phase shifters using metal-air-metal capacitors," *IEEE Trans. Microwave Theory & Tech.*, vol. 51, no. 1, pp. 309–314, Jan. 2003.

[50] E.-Y. Sun and S.-H. Chao, "Unloaded Q measurement-the critical-points method," *IEEE Trans. Microwave Theory & Tech.*, vol. 43, no. 8, pp. 1983–1986, Aug. 1995.

[51] D. Mercier, K. V. Caekenberghe, and G. M. Rebeiz, "Miniature RF MEMS switched capacitors," *IEEE MTT-S Int. Microwave Symp. Dig.*, pp. 745–748, June 2005.

[52] G. F. Craven and C. K. Mok, "The design of evanescent mode waveguide bandpass filters for a prescribed insertion loss characteristic," *IEEE Trans. Microwave Theory & Tech.*, vol. 19, no. 3, pp. 295–308, Mar. 1971.

[53] C. K. Mok, "Design of evanescent-mode waveguide diplexers," *IEEE Trans. Microwave Theory & Tech.*, vol. 21, no. 1, pp. 43–48, Jan. 1973.

[54] R. V. Snyder, "New application of evanescent mode waveguide to filter design," *IEEE Trans. Microwave Theory & Tech.*, vol. 25, no. 12, pp. 1013–1021, Dec. 1977.

[55] D. Kajfez and E. J. Hwan, "Q-factor measurement with network analyzer," *IEEE Trans. Microwave Theory & Tech.*, vol. 32, no. 7, pp. 666–1984, Jul. 1984.

[56] Rockwell Collins International, Cedar Rapids, IA USA.